NORTHWESTERN UNIVERSITY

Opening the Proteome to Analysis By Magnetic Resonance Imaging

SUBMITTED TO THE GRADUATE SCHOOL

IN PARTIAL FULLFILLMENT OF THE REQUIREMENTS

for the degree of

DOCTOR OF PHILOSOPHY

Field of Biochemistry

By

Luke Vistain

EVANSTON, ILLINOIS

MARCH 2017

Abstract

Opening the Proteome to Analysis By Magnetic Resonance Imaging

The development of metal-based probes has provided major benefits to understanding basic biological process and clinical outcomes. Metals offer access to geometries that carbon alone cannot attain, along with valuable magnetic, optical, and binding properties. Metals have proven to be particularly useful in advancing molecular imaging, a field that seeks to identify the location of events of biochemical interest in intact specimens. Such imaging is commonly achieved with a clinical modality such as positron emission tomography, single-photon emission computed tomography, or X-Ray computed tomography. However, the modality with the best combination of spatial resolution and imaging depth is magnetic resonance imaging (MRI). Metals with interesting magnetic properties have played a major role in expanding MRI from a strictly anatomical imaging technique to a modality that can be used for molecular imaging. Three different probes were designed with the goal of expanding the functionality of MRI in three unique ways.

First, a nanoparticle based probe was developed to create an MRI reporter gene that could integrate into the existing HaloTag platform. An analysis was performed that sought to couple well-understood properties of relaxation theory to quantification of protein expression levels. This analysis was then applied to the design of an MRI probe consisting of a gold nanoparticle core functionalized with Gd(III)-bearing DNA strands. Finally, those strands were coupled to a HaloTag targeting group. This nanoparticle displayed the ability to bind to HaloTag expressed on the cell surface, cause differential uptake in HaloTag-expressing cells, and HaloTag-dependent contrast in cell pellet images.

Second, a series of probes were created with the goal of imaging amyloid plaques in the brain. These plaques are indicative of Alzheimer’s disease, however there are no suitable MR probes to detect them in live samples. These Stilbene-based probes were tested for their ability to bind to amyloid fibrils and bypass the blood-brain barrier. In addition, they were evaluated for the capacity to serve as cell labeling agents by measuring their toxicity, ability to accumulate in cells, serve as bimodal agents through

stilbene fluorescence, and imaging them in cell pellets. These data conclude that, contrary to published reports, Stilbene-chelates do not cross the blood-brain barrier.

Third, iron oxide nanoparticles were applied to the development of a method for quantifying experimental metastases in the brain. Using a high-relaxivity probe developed in the Meade lab, breast cancer cells were labeled and injected in the heart of live mice. These mice were then imaged over seven days and showed clear hypointense voxels indicative of the presence of labeled micrometastases. This work outlines a procedure count metastases via MRI, identify successful injections through the use of bioluminescence, validated these results histologically fluorescence.

Finally, the basic lessons learned in probe design from HaloTag-targeting were expanded to endogenously expressed surface receptors. A second generation of targeted nanoparticles with improved particle stability and Gd(III) payload. Folate receptor and PSMA were selected using the parameters outlined in the HaloTag study. Probes targeted to each, along with HaloTag, were synthesized and characterized. Preliminary *in vitro* data showed that the second generation nanoparticles are capable of outperforming the first generation in regard to particle stability, loading, synthetic ease, and protein binding in the case of Folate Receptor-targeted nanoparticles. These agents show promise for successful translation into *in vivo* experiments.

Acknowledgements

This thesis is only possible with through the contribution of many people. Most importantly is my mentor Thomas J. Meade. The environment he created in his lab fostered the kind of collaboration and freedom that is essential to this kind of work. I would also like to thank my outstanding committee (Josh Leonard, Curt Horvath, Andrew Larson, and Khashayarasha Khazaie) for helping me give this work a shape. In particular I want to thank, Josh Leonard who went well beyond his role as my committee chair, acting as a second mentor to me.

There are also a number of people I need to thank for helping me work toward becoming a well-rounded scientist. Renee Strauch and Victoria Harrison took the time to train me in organic synthesis, despite having no experience in it. Andy Hung and Laura Lilley taught me everything I understand about the physics behind MRI. Without Matt Rotz's guidance on nanoparticle design, none of this work would have happened. I want to thank Natsuho Yamamoto for teaching me most of what I know about science writing. Zhidong Ma initially created the Stilbene project and taught me how to carry it on. And a special thanks to Adam Preslar for adding what I imagine is a year to graduate school. Each of you has been a pleasure to work with.

I have also been fortunate to mentor three amazing undergraduates. Richa Rathore, DongHee Nam, and Heeyoun Wong, your work was essential to this thesis.

To my wife, who insisted she be included in these acknowledgements, I want to thank you for your love and support. To my parents Kirk and Cindy Vistain, I want to thank you instilling in me the values that led me to a path in science, and for supporting me throughout this process.

Table of Contents

List of Figures

List of Abbreviations

ACN	Acetonitrile
AMA	Ammonium Hydroxide Methylamine
B_0	External Magnetic Field
BBB	Blood-Brain-Barrier
BME	Basement Membrane Extract
BSA	Bovine Serum Albumin
C	Celsius
CA	Contrast Agent
CNR	Contrast-to-Noise Ratio
CPG	Controlled Pore Glass
CT	X-Ray Computed Tomography
DAPI	4',6-Diamidino-2-Phenylindole
DCC	N,N'-Dicyclohexylcarbodiimide
DCM	Dichloromethane
DLS	Dynamic Light Scattering
DMEM	Dulbecco's Modified Eagle's Media
DMF	Dimethylformamide
DMSO	Dimethylsulfoxide

DNA	Deoxyribonucleic Acid
DPBS	Dulbecco's Phosphate Buffered Saline
DPBST	Dulbecco's Phosphate Buffered Saline with Tween
dT	polydeoxythymidine
DTT	Dithiothreitol
E	Energy
EDH	1-Ethyl-3-(3-dimethylaminopropyl)carbodiimide
EGF	Epidermal Growth Factor
EMT	Epithelial-to-Mesenchymal Transition
ESI-MS	Electrospray Ionization Mass Spectrometry
FBS	Fetal Bovine Serum
FDG	18F-fluoro-deoxy glucose
FLINT	Intrinsic Fluorescence
g	gram
GAPDH	glyceraldehyde 3-phosphate dehydrogenase
h	Hour
HA	Haloalkane
HPLC	High Pressure Liquid Chromatography
HRG	heregulin-β1
HT	HaloTag

HT-	U-2 OS
HT+	U-2 OS HT
ICP-MS	Inductively-Coupled Plasma Mass Spectrometry
IVIS	In Vivo Imaging System
K_d	Binding Constant
L	Liter
logP	Octanol-Water Partition Coefficient
M	Net Magnetic Moment
M	Molar
m	Meter
MALDI-MS	Matrix-Assisted Laser Desorption Ionization Mass Spectrometry
MEM	Modified Eagle's Media
MeOH	Methanol
MESF	Molecular Equivalence of Soluble Chromophore
min	Minute
MMP-9	Matrix Metalloproteinase 9
mol	mole
MPIO	Micron-Sized Superparamagnetic Iron Oxide Nanoparticles
MRI	Magnetic Resonance Imaging
MTS	MTT soluble

NHS	N-hydroxysuccinimide
NIR	Near Infrared
NMR	Nuclear Magnetic Resonance
NMRD	Nuclear Magnetic Resonance Dispersion
OD	Optical Density
PBS	Phosphate Buffered Saline
PCA	Personal Cell Analyzer
PET	Positron Emission Tomography
pH	Acidity
PK/PD	Pharmacokinetic and pharmacodynamics
PSMA	Prostate-Specific Membrane Antigen
q	Water Coordination Number
r_1	T_1 Relaxation Rate
r_2	T_2 Relaxation Rate
RF	Radiofrequency
ROI	Region of Interest
RPMI	Roswell Park Memorial Institute medium
RT	Room Temperature
s	Second
SB	Stilbene

sb	Schiff's Base
SBM	Solomon-Bloembergen-Morgan
SDS-PAGE	Sodium Dodecyl Sulfate Polyacrylamide Gel Electrophoresis
SNA	Spherical Nucleic Acid
SNR	Signal-to-Noise Ratio
SPECT	Single Photon Emission Computed Tomography
SPION	Superparamagnetic Iron Oxide Nanoparticles
T	Tesla
T_1	Spin-Lattice Relaxation Time
T_{1e}	Electron Relaxation Time
T_2	Spin-Spin Relaxation Time
TEA	Triethylamine
TEAA	Triethylammmonium Acetate
TEM	Transmission Electron Microscopy
TF	Transcription Factor
THF	Tetrahydrofuran
THPTA	Tris(3-hydroxypropyltriazolylmethyl)amine
THT	Thioflavin T
UV	Ultraviolet
τ_c	Correlation Time

τ_m	Mean Residence Lifetime
τ_R	Rotational Correlation Time
$\hbar$	Reduced Plank's Constant
γ	Gyromagnetic Ratio
ω_o	Angular Frequency

Chapter One

An Introduction to Molecular Imaging

1.1 Molecular Imaging

The advent of molecular biology has been successful in elucidating the specific mechanisms of hundreds of diseases. However, linking the tremendous progress in understanding the molecular mechanisms of biology to human health remains an outstanding problem. In part, this difficulty arises from the need to be translate these discoveries into *in vivo* model systems that reflect the entire physiology of the specimen. The capacity to monitor a molecular event in an intact organism is fundamentally a problem of detection. Molecular imaging is a field that creates a link between the molecular interactions that drive biology and the living systems in which the interactions occur. Its purpose is to serve as a bridge technology that expands the scope of fundamental discoveries in biology and couples them to clinical outcomes.

Non-invasive imaging provides several distinct advantages over invasive techniques such as histology and biopsy. First, molecular imaging minimizes perturbation of the sample, adding confidence that the measured effect is a not a consequence of the measurement process. Second, it enables dynamic measurements because, unlike histology, samples do not need to be sacrificed for measurements to be taken. Third, both histology and biopsy introduces sampling bias that molecular imaging can overcome by imaging the entire specimen. Finally, molecular imaging is particularly well suited to events that have clear importance but occur in an unknown location.

The central feature of a molecular imagining is non-invasive detection of a specific molecule or molecular interaction. Although molecular imaging includes a wide variety of different techniques, each experiment has in common several general features. First, there must be a chemical tracer that is both easy to measure and able to interact with the molecular event of interest. Second, there must be an imaging modality to indicate the specific location of the tracer, and thus the molecular event. Additionally, a second imaging modality may be used if the first is unable to provide sufficient anatomical context. Each imaging modality has a set of intrinsic strengths and weaknesses. Generally, the choice of modality must be made to reflect the specific experiment or diagnostic goal. Clinical modalities are most common, including, Positron Emission Tomography (PET), Single-Photon Emission Computed Tomography (SPECT), Magnetic Resonance Imaging (MRI), and optical techniques.

The benefits of molecular imaging interface directly with human health. The dominant clinical agent is ^{18}F-fluoro-deoxy glucose (FDG). This PET probe is used to identify tissues with usually high glycolytic activity. It is routinely used to stage a cancer diagnosis and identify the location and abundance of metastases (1, 2). In addition to FDG, there are a battery of clinically approved agents to image specific biomarkers such as tumor cell metabolism, inflammation, amyloid plaques, and surface receptors (3-5). Clinical MR images are routinely enhanced with untargeted contrast agents that improve the quality of anatomical images (6). Optical imaging has limited penetrance into the clinic. However, it is frequently used to guide surgeries (7).

1.2 Molecular Imaging Modalities

1.2.1 Positron Emission Tomography

PET is one of the nuclear techniques that define the gold standard for molecular imaging. It forms an image by measuring the radiation generated from a positron-emitting nuclide. As PET tracers degrade, the released positron travels though the sample until it encounters an electron. Upon doing so, both particles annihilate and emit a pair of gamma photons oriented 180˚ to one another (8). These photons constitute the signal that is measured by a detector and used to form an image. The high energy of the emitted photons, along with the paired emission of those photons, results in PET having the best sensitivity of any molecular imaging technique (approaching the picomolar range) (8). The most commonly used nuclei are ^{18}F ($t_{1/2}$ = 109.8 min), ^{64}Cu ($t_{1/2}$ = 12.7 h), ^{76}Br ($t_{1/2}$ = 16.2 h), ^{11}C ($t_{1/2}$ = 20.3 min), ^{13}N ($t_{1/2}$ = 10 min), and ^{15}O ($t_{1/2}$ = 2.04 min) (8). The choice of radionuclide is determined by the chemistry that is available for radionuclide incorporation, the half-life of the radionuclide, and the proximity to a cyclotron that can produce the desired radionuclide.

Positron-emitting radiation and gamma ray detection are well-understood, and as a result there is a strong theoretical foundation for understanding PET detection limits. The camera used in a PET experiment is comprised of an immobile ring surrounding the specimen. The ring contains scintillator crystals, which luminesce upon encountering a gamma ray, and cameras to detect the luminescence (9). The major technical limit to PET resolution is defined by the width of the detector element (9). The smaller these elements, the better the resolution. Other technical limitations include the distance that the photon travels through the detector before it interacts with the scintillator crystal, the optical decoding of scintillation events (generally there are more crystals than cameras), and sampling errors (not all locations in the field-of-view have the same number of assigned detectors). In addition, there are two physical limits to the spatial resolution imposed by the physics of positron detection. First, positrons travel some distance (up to several millimeters) before they encounter an electron and annihilate to produce gamma rays. Second, while the photons emitted from annihilation are at 180˚ in the rest frame of the positron, due the particle's high speed there is a small acolinearity error in the laboratory frame. Clinical PET image resolution is in the mm range and research PET can achieve resolutions as low as 0.5mm (10, 11).

PET imaging has undergone very successful translation into the clinic. FDG has proven to be a highly versatile probe that can indicate a high metabolic rate for a variety of cells in addition to cancer (12). FDG serves as a fluorinated glucose mimic that can enter cells through the GLUT1 transport, be phosphorylated by hexokinase and trapped in the cell, but is unable to continue through glycolysis (8). As a result, FDG accumulates in cells that have high glucose requirements and is particularly useful for locating the presence of a tumor that is using aerobic glycolysis (the Warburg effect) as its primary energy source (13). Beyond FDG, radionuclides can be incorporated into an existing drug to provide a tracer that is chemically identical to the drug. These can be used to create highly accurate pharmacokinetic and pharmacodynamics (PK/PD) data, both in mice and humans (4). Novel PET probes are a very active area of research, with major progress in clinical translation for many targets, including imaging amino acid metabolism, hypoxia, apoptosis, angiogenesis, and amyloid-beta plaques (5, 14-17).

1.2.2 Single-Photon Emission Computed Tomography

SPECT probes operate on similar principle to PET probes, in that both involve the detection of nuclear decay. SPECT probes consist of gamma-emitting radionuclides rather than positron-emitting. The most prevalent are ^{99m}Tc ($t_{1/2}$ = 6 h), ^{123}I ($t_{1/2}$ = 13.3 h), ^{111}In ($t_{1/2}$ = 2.8 days), and ^{67}Ga ($t_{1/2}$ = 3.3 days) (18). When these nuclei degrade they release a single gamma ray photon that can be measured by a SPECT device and used to generate an image (8). Because SPECT agents release only one photon upon degradation it can be difficult to ensure that a measured photon came from the probe. This problem is addressed by counting photons that strike the detector at a right angle and discarding all others. As a result, SPECT agents have a lower sensitivity (approaching the nanomolar range) than PET (8). In order to produce tomographic images with SPECT, the gamma counter needs to be rotated around the subject. The spatial resolution is therefore limited by the accuracy of the mechanical component rotating around the subject, and the tradeoff between rejecting off-angle incident photons and the loss of sensitivity that comes from counting fewer photons. Clinical SPECT devices typically have a spatial resolution in the 1-2mm range, whereas research SPECT can achieve resolutions as low as 0.25mm (8, 19).

The clinical success of SPECT imaging is comparable to that of PET imaging. SPECT agents typically have longer half-lives than PET agents, and many of the radionuclides are metals. These traits combine to expand the number of available chemistries that can be used for SPECT. There is a strong foundation in chelate chemistry that facilitates attachment chemistry of SPECT-active metals to targeting groups (18). There is significant overlap between the applications of SPECT and PET, including PK/PD, apoptosis, and amyloid-beta plaques (20-22). In addition, SPECT is well suited to antibody conjugation (23).

1.2.3 In Vivo Optical Imaging

Optical imaging is among the most commonly used molecular imaging technique for research purposes. Light can be detected *in vivo* from either a fluorophore of a source of luminescence. Despite some shortcomings, optical imaging is still popular in research in part because the detection equipment is inexpensive and compatible with the fluorophores and luciferases that are common in molecular biology. The key limitation for optical imaging is that many biomolecules absorb light in the UV and visible wavelengths. Ideally the light passing through the sample will be in the near infrared (NIR) range (650-900nm) because this wavelength range minimizes light absorption by biomolecules (24). Regardless of the selected wavelength, scattering of light as it passes through the sample makes it difficult to precisely locate the source of light. This limits the spatial resolution. Typically, scattering and absorption make it difficult to detect an optical signal more than a centimeter from the surface of the specimen (25). Finally, because both absorption and scattering are dependent on the distance that the light travels through the sample, optical imaging is always surface-weighted and both the sensitivity and spatial resolution will depend heavily on how deep in the sample the light source is (25).

Under ideal circumstances, optical imaging has the highest spatial resolution, with the diffraction-limited resolution limit of 250nm, determined by the wavelength of light. However, this resolution only applies to intravital and surface imaging. For the majority of *in vivo* optical imaging, the spatial resolution will be will be significantly reduced by light scattering as it passes through the specimen. For light passing through an array of scatterers, the likelihood of scattering will depend on the distance that the light travels and its wavelength relative to the size of the scatterers (26). As a result, the precise spatial resolution will depend heavily on the wavelength of the light and the tissue depth that light-emitting molecule resides at. Due to the capacity of biological tissues to strongly absorb the shorter wavelengths of visible light, red or NIR are strongly preferred for optical imaging *in vivo*. A fluorophore that emits in the NIR window can achieve spatial resolutions as high as 30μm at a shallow depth (3mm), with lower spatial resolutions for deeper tissue (27).

1.2.4 X-Ray Computed Tomography

X-ray computed tomography (CT) is primarily an anatomical technique with some molecular imaging applications. It is the three-dimensional extension of traditional two-dimensional x-ray images. In order to produce tomographic images, an x-ray source and detector are rotated around the specimen as a pair. Image contrast is determined by the x-ray attenuation of the sample, with areas of high electron density (such as bone) producing positive contrast and areas of low electron density (such as the air in the lungs) producing negative contrast (8). The importance of electron density results in an image with excellent hard-tissue contrast but fairly modest soft tissue contrast. CT resolution is not limited by the depth of penetration in the sample.

CT is primarily considered to be an anatomical technique, but there is growing interest in developing contrast agents that can identify locations of biological interest. In principle, any electron-dense material can serve as a CT contrast agent. Iodinated contrast agents have long been used to generate additional contrast for soft tissues (28). Recently, gold nanoparticles have begun to draw attention as CT contrast agents due to their high atomic number and capacity for targeting (29).

1.3 Magnetic Resonance Imaging

MRI has several features that make it unique among the imaging modalities. First, MRI can be used in the absence of contrast agents because it produces anatomical images. This stems from the fact that MRI is typically measuring the signal generated by water protons in the sample, rather than directly from a contrast agent. Second, it can achieve a spatial resolution below 100µm, lower than any other technique that has unlimited penetration depth (30). Third, unlike the PET, SPECT, and CT, MRI does not require the use of ionizing radiation. This is a major advantage clinically, since the same patient can be imaged multiple times without concern for radiation exposure. Finally, MRI has the best soft tissue contrast of any modality that can be used for anatomical imaging. This property has driven widespread clinical use, as the excellent soft-tissue contrast it provides enables easy discrimination between tissues. The status of MRI as a molecular imaging technique is a matter of debate, as it is often thought of as a very effective anatomical technique that can’t achieve the sensitivity to image molecular events.

MRI generates an image by taking advantage of the magnetic properties of various nuclei, most commonly ^{1}H. The technique uses of well-understood properties that govern how nuclei respond to an external magnetic field. These magnetic properties can be perturbed such that they provide information about the sample that can be used to form an image. There are two core physical properties that enable an MRI experiment to occur: magnetic alignment and precession.

Any nucleus with spin angular momentum has a nuclear magnetic moment. The key dynamic in an MRI experiment is the relationship between the nuclear magnetic moment of ^{1}H and the external magnetic field. In the absence of an external magnetic field (B_0), there is no preferred orientation for the nuclear magnetic moment of each nucleus. The external magnetic field induces a preferred orientation for the nuclear magnetic moment, resulting in nuclei adopting either a spin-up orientation in preference over a spin-down orientation, with the lowest energy state pointing along the B_0 vector. Thus more spins align with the vector of the external field and a macroscopic net magnetic moment forms for the sample. The energy difference between the spin-up and spin-down states is due to Zeeman splitting, and the energy difference can be calculated from the Zeeman equation, where $\Delta\mathrm{E}$ is the energy difference between orientations, γ is the gyromagnetic ration unique to each nucleus, and $\hbar$ is the reduced Plank's constant (Equation 1.1). The energy difference is directly

Equation 1.1 $$\Delta\mathrm{E} = \gamma\hbar\mathrm{B}_0$$

proportional to the external field strength. This equation also motivates the need for stronger MR magnets, as the energy difference between these states is related to the signal-to-noise ratio for imaging. Clinical magnetics are typically 1.5-3.0 T and research magnetics can achieve field strengths as high as 11.4 T.

In addition to aligning with the external magnetic field, each ^{1}H also precesses around it. This precession has a characteristic angular frequency (ω_o) described by the Larmor equation (Equation 1.2).

Equation 1.2 $$\omega_0 = \gamma\mathrm{B}_0$$

Nuclear spins process with a frequency that is proportional to the strength of the external magnetic. Due precession at the Larmor frequency, the sample can undergo resonance with electromagnetic radiation at a matching frequency in the radiofrequency (RF) range, thus enabling perturbation of the magnetic moment with an appropriate RF pulse. Once the magnetic moment is perturbed, it will relax back to the lowest energy state. The response of the magnetic moment to perturbation is the physical property used to create the MR image.

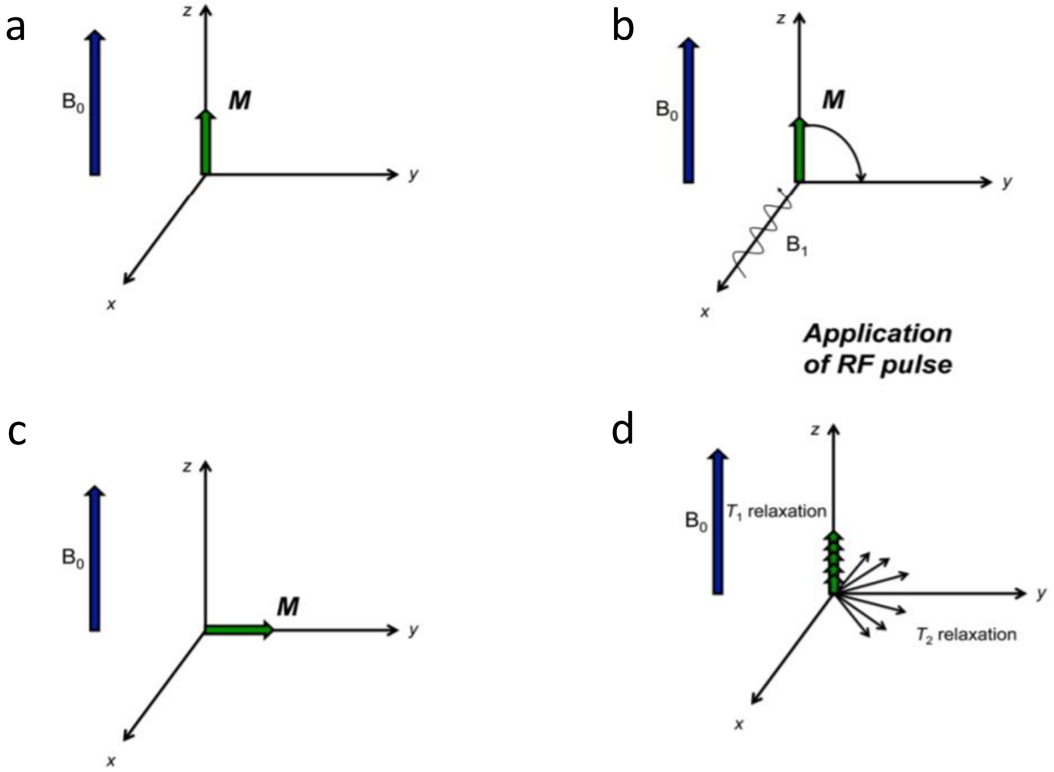

Figure 1.1 Description of the net magnetic moment formed by nuclei in an external magnetic field

a) Because aligning with the magnetic field is the lowest energy state, nuclei form a net magnetic moment (**M**) that points parallel to the external magnetic field (B_o). b) An RF pulse can interact with **M** causing it to rotate. c) **M** can exist in the XY-plane after RF stimulation. d) Two types or relaxation occur after RF perturbation. The spins that contribute to **M** in the XY-plane lose coherency, causing loss of magnetization in the plane. This is represented by the T_2 relaxation rate. In addition, **M** returns to its original orientation pointing parallel to B_0. This is represent by the T_1 relaxation rate. Image modified and reproduced with permission from Heffern *et al*. Chemical Reviews, 2013.

There are two primary time constants that describe how a magnetic spin relaxes upon perturbation. Prior to perturbation, the net magnetic moment points along the direction of the external magnetic field. By convention, this is defined as the Z axis (Figure 1.1). In addition, individual nuclei precess around the Z axis with different phases, resulting in a net magnetic moment of zero in the XY plane. Consider an instance in which a 90˚ RF pulse is applied to the sample. This will cause the magnetic moment to rotate into the XY plane, and cause the nuclei to precess in phase with one another (Figure 1.1). The magnetization vector will now relax in two ways, by returning magnetization to the Z axis and by losing magnetization in the XY plane. Realignment with B_0 is called T_1 relaxation and occurs as the excited spins release the absorbed RF energy into the surrounding lattice. When T_1 relaxation is complete the magnetic moment again points along the Z axis. (Figure 1.1). The second form of relaxation that concerns the dephasing of the magnetic vector in the XY plane (Figure 1.1). The amount of time it takes to dephase is defined by T_2. MRI scans are designed to generate image contrast that depends on these values. The excellent soft tissue contrast seen in MR images stems from the fact that various tissues tend to display a wide range of T_1 and T_2 values. In addition, exogenous contrast can be produced from any chemical agent that modulates these relaxation rates.

MRI is capable of achieving the highest spatial resolution of any *in vivo* imaging modality. However, the precise spatial resolution dependent on several factors. The field strength is a key variable, since the signal-to-noise ratio (SNR) improves with increasing field. Resolution is also limited by the amount of time that can be devoted to scanning the subject. There are two key physical limitations to the MRI spatial resolution. The ultimate limit is the degree of molecular diffusion that can occur on the scale of the MR scan (31). However, the more significant limit is imposed by the distance between the scanner coil which detects the MR signal and the subject. Under ideal circumstances, MR images can achieve in-plane spatial resolutions in the hundreds of micrometers, whereas research MRI can achieve spatial resolutions as low as 25 µm (32).

1.3.1 MRI Contrast agents

MRI is a uniquely advantageous imaging modality. However, despite its many advantages it is not yet considered the gold standard molecular imaging modality. In large part, the effectiveness of MR contrast agents has prevented MR from dominating the molecular imaging field.

There are several classes of contrast media that can be applied to MR imaging. Because MRI is typically detecting the magnetic properties of water ^{1}H, contrast agents can be chemicals that are composed of other magnetic nuclei (such as ^{19}F), ^{1}H with unique chemical shifts, or chemicals that change the relaxation rates of water ^{1}H (33). All clinically approved MR contrast agents fall into the last category, which is in turn divided into agents that preferentially shorten the T_1 relaxation rate, or the T_2 relaxation rate. Despite this division, all such agents shorten both relaxation rates, and their categorization is only a convention that reflects what the agents are best suited for.

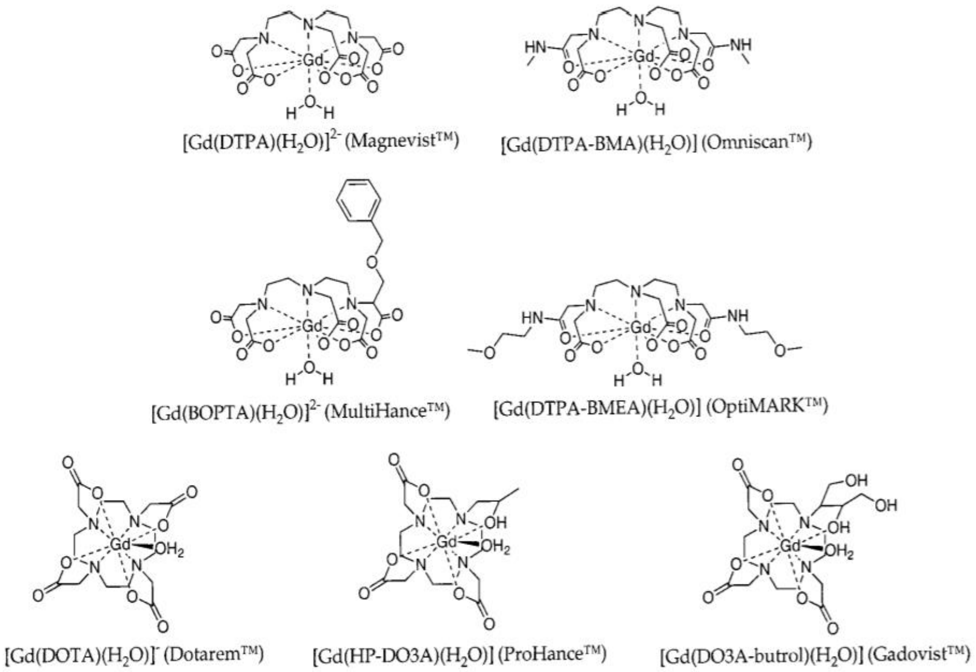

$[Gd(DTPA)(H_2O)]^{2-}$ (Magnevist™)

$[Gd(DTPA\text{-}BMA)(H_2O)]$ (Omniscan™)

$[Gd(BOPTA)(H_2O)]^{2-}$ (MultiHance™)

$[Gd(DTPA\text{-}BMEA)(H_2O)]$ (OptiMARK™)

$[Gd(DOTA)(H_2O)]^-$ (Dotarem™)

$[Gd(HP\text{-}DO3A)(H_2O)]$ (ProHance™)

$[Gd(DO3A\text{-}butrol)(H_2O)]$ (Gadovist™)

Figure 1.2 Structures of all clinically approved Gd(III) contrast agents.

Each agent is composed of a single Gd(III) atom chelated by an 8-coordinate ligand. The remaining coordination site is occupied by water. Reproduced with permission from Caravan *et al*. Chemical Reviews, 1999.

Gadolinium is the most commonly used MR contrast agent, with up to 30% of clinical MR images enhanced with Gd(III) (6). It is classified as a T_1 agent. There are several clinically approved Gd(III) contrast agents that are routinely used (Figure 1.2). All clinical Gd(III) contrast agents are administered as chelates to prevent toxicity associated with Gd(III). These agents have proven to be particularly useful in decreasing MR scan times, staging brain cancer, and angiography (34, 35). Beyond the clinic, Gd(III) chelates have been extensively studied as molecular imaging tools. This includes designing probes to respond to biochemical activity (36-38), target biomarkers of interest (39-42), label cells (43-45), and track implants (46). The versatility of Gd(III) stems in part from a thorough understanding of the relationship between the chemical properties of Gd(III) chelates and relaxation rates.

Gd(III) is useful as a contrast agent because it is paramagnetic, has seven unpaired electrons, and an electron relaxation time comparable to the Larmor frequency of ^{1}H (47). The large magnetic moment of Gd(III) causes it to efficiently increase the relaxation rate of water molecules that are bound to it. Gd(III) is nine-coordinate and chelates typically occupy seven or eight of those coordination sites, with water occupying the remainder (Figure 1.2). The relationship between a Gd(III) chelate and the observed T_1 relaxation rate can be described by the Solomon-Bloembergen-Morgan (SBM) equations (48). These equations define a term, relaxivity (r_1), as the change in T_1 caused by a given concentration of contrast agent (Equation 1.3). Furthermore, the relaxivity can be related to several molecular characteristics of the contrast agent.

Equation 1.3 $$\frac{1}{\mathrm{T_{1obs}}} = \frac{1}{\mathrm{T_{1d}}} + \mathrm{r_1}[\mathrm{Gd}]$$

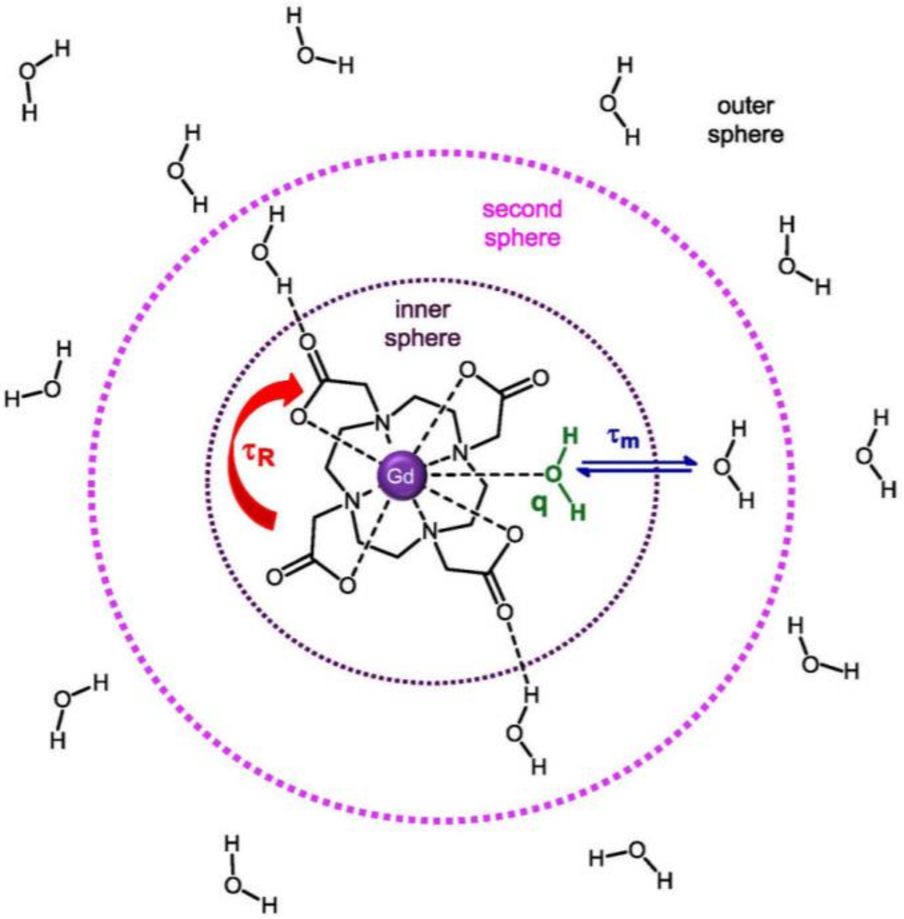

Figure 1.3 A description of the chemical properties that govern chelate relaxivity.

The inner sphere is limited to water molecules that directly interact with Gd(III). The relaxivity of the inner sphere is dependent on the number of bound water molecules (q), the amount of time they remain bound to Gd(III) (τ_m), and the chelates rotational correlation time (τ_R). In addition, relaxivity is effected by the second sphere and outer sphere. Second sphere is defined as any water in the hydrogen bonding network with the chelate, whereas outer sphere concerns only bulk water. Image modified and reproduced with permission from Manus *et al*. Analytical Chemistry, 2012.

There are three key variable parameters that contribute to r_1 (Figure 1.3). First, is the hydration number (*q)*, which is the number of water molecules bound to the inner-sphere of the chelate at one time. Second, is the mean residence lifetime of bound water (τ_m). Third, is the rotational correlation time (τ_r). The *q* value scales linearly with r_1, and typically chelates will be q = 1 or 2 (6). τ_m and τ_r have a more complex relationship with r_1. Relaxivity is maximized when the total correlation time, τ_c, matches the Larmor frequency. τ_c can be calculated from equation 1.4, where T_{1e} is the electronic relaxation time and is intrinsic to Gd(III).

Equation 1.4 $$\frac{1}{\tau_c} = \frac{1}{\mathrm{T}_{1e}} + \frac{1}{\tau_r} + \frac{1}{\tau_m}$$

Gd(III) chelates can be activated for molecular imaging purposes by causing a molecular event to change any of the above parameters, including [Gd(III)]. Modification of a chelate's τ_r value is often the most feasible option for producing additional relaxivity. The value of τ_r correlates with the molecular weight of the chelate, and thus can be dramatically changed by binding to a macromolecule. This strategy has been explored at length both in the clinic and in research (49-51). In 2000 the Meade Lab showed that q-modulation can be used to detect the presence of beta-galactosidase through changing the number of coordinating groups on the Gd(III) chelate (52). Unlike q and τ_r, τ_m is more difficult to associate with a measurable physical parameter. As a result, there few instances in the literature of adjusting τ_m to activate a chelate (46, 53). Rather, it is primarily used as a tool for increasing overall chelate effectiveness. Finally, analogous to the nuclear techniques, Gd(III) can produce additional contrast simply by targeting a biochemical event that is enriched over the background, such that [Gd(III)] exceeds non-specific binding (40, 54).

The second class of MR contrast agents, T_2-weighted agents, have also been extensively studied. Such agents generate negative contrast in a MR image, producing voxels of lower signal intensity. These agents can also be described with a relaxivity term, r_2. The most common of these agents is iron oxide.

1.3.2 The detection limit of Gd(III) contrast agents

Compared to the thorough exploration of Gd(III) chemistry in the literature, there is comparatively little inquiry into the fundamental limits of molecular imaging with MRI. However, given the low concentrations of typical biological analytes, a complete understand of the detection limit of Gd(III) is absolutely essential to guiding design principles for molecular imaging probes. Particularly in the case of targeted probes, it is feasible to link the theory of relaxation to target abundance such that a basic estimation of the detection limit can be used to guide probe design.

The SBM equations can be used to create a mathematical model for the detection limit of Gd(III). Such a model was formalized by Eric Ahrens in 1998 (Equation 1.5) (55).

Equation 1.5 $$[\mathrm{M}]_\mathrm{a} = \frac{1-\Gamma}{\Gamma \mathrm{T}_{01}\mathrm{R}} + \frac{[\mathrm{M}]_\mathrm{b}}{\Gamma}$$

The model determines the degree of T_1 shortening required for detection by considering the intrinsic T_1 of the tissue (T_{01}) surrounding the target, the amount of non-specifically bound Gd(III) probe ($[M]_b$), and the signal-to-noise capacity of the specific MR device (Γ). The required amount of Gd(III) to reach this T_1 value ($[M]_a$) can be determined from the relaxivity equation. The key conclusion of Ahren's analysis was that the detection limit was unacceptably high (≈100μM) for molecular imaging devices and chelates commonly used in the clinic. Typically analytes targeted for molecular imaging range from 1-1000nM.

The strength of MR devices has improved significantly over the last two decades. The detection limit model includes a term (Γ) that can be used to reflect these improvements in MR technology. Whereas clinical MRI magnets were typically 1.5 T in 1998, modern research magnets can run in the 7-11.4 T range. Stronger external magnets increase the Zeeman splitting, which results in higher SNR. This improvement dramatically lowers the detection limit of Gd(III). Estimates for the detection limit at 9.4T are close to 10 µM Gd(III) (56). While this is still far above the desired range of detection for molecular imaging, it is possible to close the remaining gap using chemical techniques. The use of chemical techniques is essential in this case, because there is a sharp diminishing of returns for additional increases in field strength. As shown in a typical Nuclear Magnetic Relaxation Dispersion for a high-molecular weight Gd(III) probe (Figure 1.4), relaxivity plummets at high field. In total, 7-11.4 T represents an imaging window which maximizes the tradeoff between gain of sensitivity and loss of relaxivity.

The ability to quantify the expression level of biologically interesting analytes has rapidly improved in recent years. Quantitative knowledge of protein expression levels can be easily incorporated into Ahrens' detection limit model, if one includes an estimate of cell size. In 2011 a global quantification of protein expression levels for mouse fibroblasts was reported (57). This analysis provided crucial insight into what the average protein expression level is, the shape of the expression distribution curve, and allows the average expression level to be further subdivided by major protein classes, such as surface receptors. Unsurprisingly, the 10 µM detection limit of Gd(III) would allow only the most highly expressed proteins in the cell to be measured (assuming a cell volume ≈1 pL), few of which are regulated in a way that would make them interesting molecular imaging targets.

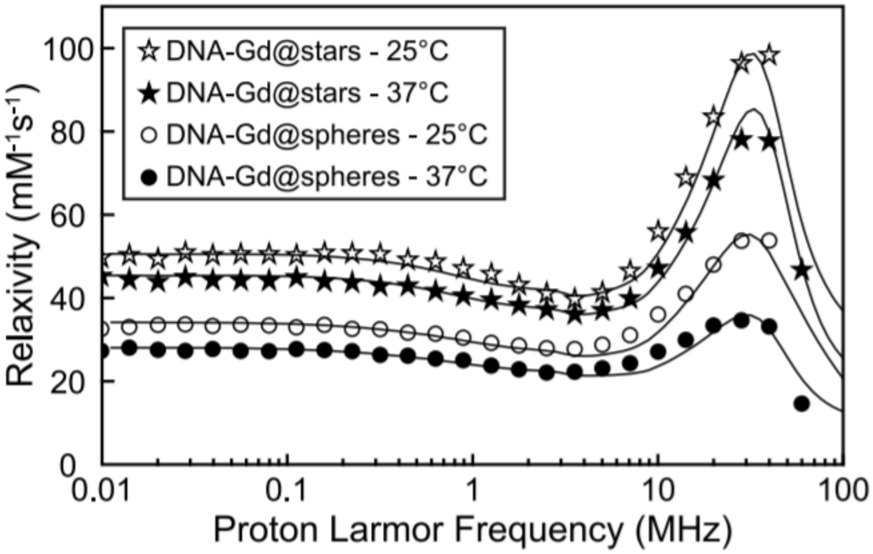

Figure 1.4 A measurement of the effect of field strength on relaxivity for a pair of nanoconstructs. The relaxivity of Gd(III) functionalized gold nanostars or nanospheres are measured at multiple field strengths and temperatures. After peaking at 20 MHz (0.47 T), relaxivity drops dramatically. Relaxivity at 60 MHz (1.4 T) is typically less than half its value at 20 MHz. Reproduced with permission from Rotz *et al*. ACS Nano, 2015.

With a firm grasp on both the detection limit of Gd(III) and the expression level of typical protein targets, it is possible to outline a set of design parameters and limitations for hypothetical Gd(III) molecular imaging probe. The most important feature is large-scale multiplexing. The SBM equations limit the effectiveness of Gd(III) chelates at high field, resulting in concentration being the only tunable parameter to drive better sensitivity. Nanotechnology is well suited to achieving the payloads required. Multiplexing Gd(III) 100-fold would open the top 25% of the proteome to MR analysis (57). However, such an agent would have a molecular weight too high for membrane permeability, thus limiting the targetable proteome to proteins expressed on the cell surface. Larger particles enable additional multiplexing, however, particle size introduces significant limitations compared to small-molecule targeted Gd(III) chelates. Large particles have limited tissue penetrance and are rapidly cleared from the bloodstream through the reticuloendothelial system (58). While tissue penetrance is limited for all nanoconstructs, it has been shown smaller nanoparticles achieve higher tumor penetration than larger ones (58). Taken together, these facts suggest a window to enable molecular imaging using modern high-field MR devices and targeted nanoconstructs.

1.4 Scope of Thesis

This thesis focuses on the development of a series of chemical tools designed to use MR imaging to improve the quality of biological research. Each tool attempts to expand the MR toolkit in a unique way. Three of the tools focus on Gd(III)-based contrast agents for the detection of proteins and a fourth focuses on iron oxide nanoparticles for cell tracking. Specifically, Chapter One gives an overview of every imaging modality used in for molecular imaging, while highlighting their respective strengths and weaknesses. In addition this chapter discusses the basic physical properties that give rise to MRI, how contrast agents can be used to track events *in vivo*, and the major hurdles that can be addressed by chemical means. Chapter Two describes the development of a nanoparticle-based contrast agent targeted to the HaloTag protein, with the overall goal of creating a broadly applicable reporter gene for MRI. Chapter Three discusses the design and testing of a series of Gd(III) probes targeted to amyloid plaques for the purpose of non-invasively detecting the presence of Alzheimer’s plaques. Chapter Four outlines a procedure for labeling, tracking, and validating experimental metastases in the brain of mice. Chapter Five explores the capacity of second-generation nanoparticle probes to detect the presence of endogenous surface receptors, Folate Receptor and Prostate Specific Membrane Antigen (PSMA).

In addition to the discussion of MR probes, this thesis contains an appendix evaluating a Co(II)-based transcription factor inhibitor. This inhibitor was shown to impair the capacity of Snail to induce an epithelial-to-mesenchymal transition in multiple breast cancer cells, potentially reducing their capacity to metastasize.

Chapter Two

Targeted Delivery of gold nanoparticle contrast agents for reporting gene detection by magnetic resonance imaging

Reproduced from Vistain *et al*. Chemical Communications, 2016 with permission from The Royal Society of Chemistry

2.1 Introduction

The field of molecular imaging is motivated by the need for techniques that enable *in vivo* visualization of biochemical processes, biomarkers, and gene expression (8, 59, 60). Magnetic resonance imaging (MRI) is an appealing modality for molecular imaging because it provides excellent spatial resolution (<100 μm), detailed anatomical information, and does not require exposing the subject to potentially harmful ionizing radiation (31). Where native MR contrast is insufficient, contrast agents (CAs), such as those based on paramagnetic gadolinium, are used to shorten water proton relaxation times, increasing image contrast. However, the low sensitivity of Gd(III) CAs has limited their utility in molecular imaging due to the high concentrations required to produce contrast (10-100 μM) (55). Crucially, many biomolecules are present at concentrations (0.1-1 μM) that are below the detection limit of Gd(III) CAs (56). To date, molecular imaging using Gd(III) has been limited to a small number of biomarkers present at high concentrations *in vivo* (21, 39, 40, 42, 61-63).

The low sensitivity of Gd(III) CAs has made it challenging to develop MR reporter genes. Many of these genes are from endogenous proteins, produce negative contrast (bright-to-dark), and generate only modest contrast overall (36, 52, 64-67). Furthermore, none of the genes in these systems have been integrated into existing reporter gene platforms. As such, their utility is limited because they require a unique genetic element dedicated solely to MR detection.

An ideal reporter platform for MR monitoring of gene expression presents extracellularly**,** integrates into an existing reporter gene platform, provides irreversible binding of molecular probes, and contains the necessary signal amplification to overcome the low sensitivity of Gd(III) probes. The HaloTag reporter gene system addresses these challenges (68). HaloTag is an engineered haloalkane delahogenase that can be expressed on the outer surface of the plasma membrane (69). The enzyme active site has been modified to catalyze covalent bond formation with terminal haloalkanes, promoting superior probe retention (68). Because haloalkanes are virtually absent from eukaryotic systems, HaloTag and its targeting group create an orthogonal binding pair. Furthermore, HaloTag can readily form functional fusions with a variety of proteins (70). The specificity and versatility of the HaloTag system make it attractive as an MR reporter gene. In addition, it operates as a variable-output reporter gene, whereby the researcher can select the nature of the output by choosing the appropriate HaloTag-targeted agent. For this reason, a variety of imaging agents, including fluorophores, PET agents, MR agents, and quantum dots have been successfully targeted to HaloTag (50, 69, 71, 72). However, coupling HaloTag expression to the production of T_1 contrast demands significant signal amplification.

Spherical nucleic acids (SNAs) have the potential to address this design requirement (73). Extensive work on over 100 cell types showed that SNAs exhibit high biocompatibility and low toxicity *in vitro* and *in vivo* (74, 75). Furthermore, previous work with SNAs developed a multiplexing strategy to deliver a high payload of Gd(III) chelates (76). In this case, the SNAs were not targeted and their cellular uptake was a result of SNAs binding to scavenger receptors on the cell surface (77). Although SNAs can be targeted using antibodies or aptamers, there is no precedent for SNA targeting using small molecule ligands (78, 79).

2.2 Results and Discussion

HaloTag-targeted AuDNA-Gd(III) nanoparticles were synthesized according to Figure 2.1. A 24-mer polydeoxythymidine (dT) oligonucleotide bearing a protected 3’ thiol and a 5’ terminal haloalkane (HA) moiety for HaloTag binding was synthesized (Figure 2.2). The oligonucleotide included modified dT bases bearing terminal alkyne functionality at five positions internal to each strand. Using a Gd(III) chelate bearing an azide functionality, a Cu(I)-catalyzed 1,3 dipolar cycloaddition was conducted to produce the complete HaloTag-targeted Gd(III) DNA (Figure 2.2). The purified oligonucleotide was deprotected to expose the 3’ thiol and conjugated to gold nanoparticles using a salt aging procedure. (80)

The density of oligonucleotide loading on the particle surface was determined by calculation of the Gd/Au ratio using Inductively Coupled Plasma Mass Spectrometry (ICP-MS) (76). Results indicate that the average loading of DNA was 100 ± 10 strands per particle, yielding a Gd(III)-chelate payload of 500 ± 60 per particle. The T_1 relaxivity (r_1) was measured to be 16 ± 3 $mM^{-1}s^{-1}$ per Gd(III) at 37 °C and 1.41 T, and the T_2 relaxivity (r_2) was measured to be 28 ± 3 $mM^{-1}s^{-1}$ per Gd(III). We hypothesized that this degree of signal amplification would enable visualization of surface receptors that would be below the detection limit of individual Gd(III) chelates.

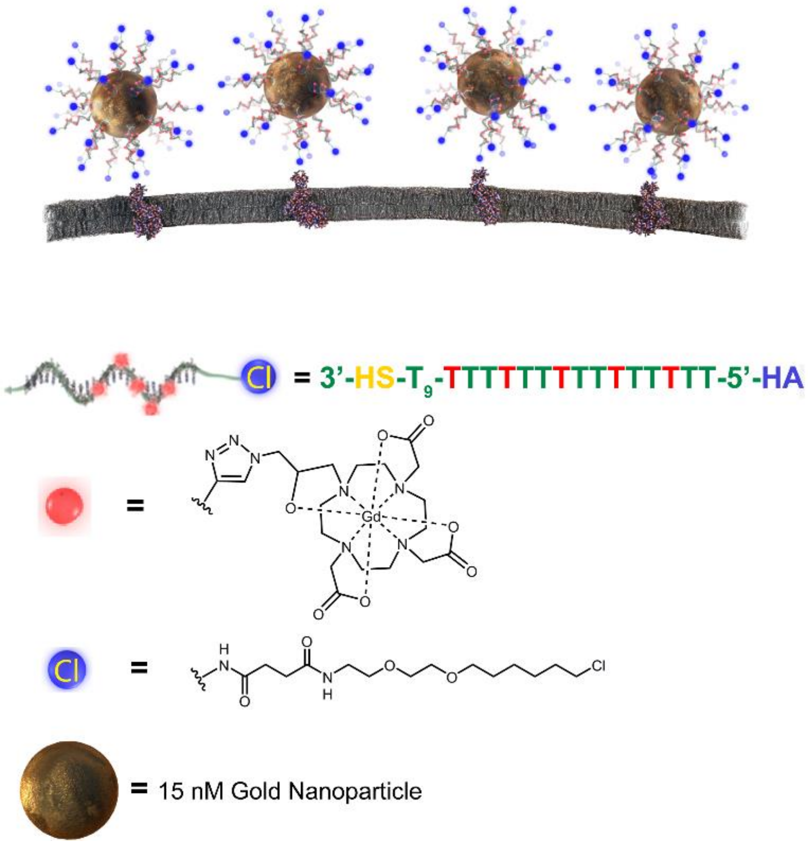

Figure 2.1. Schematic of AuDNA-Gd(III)-HA binding to HaloTag on the cell surface.

Each particle delivers a high payload of Gd(III) to a single protein. The nanoparticle consists of a 15 nm gold core that is bound to several copies of single stranded DNA. Each strand contains five covalently attached Gd(III) complexes. The 3’ end is functionalized with a thiol for gold binding and the 5’ end is modified to include a haloalkane (HA) moiety for HaloTag targeting. Azide functionalized Gd(III) chelates are used to label the DNA with Gd(III).

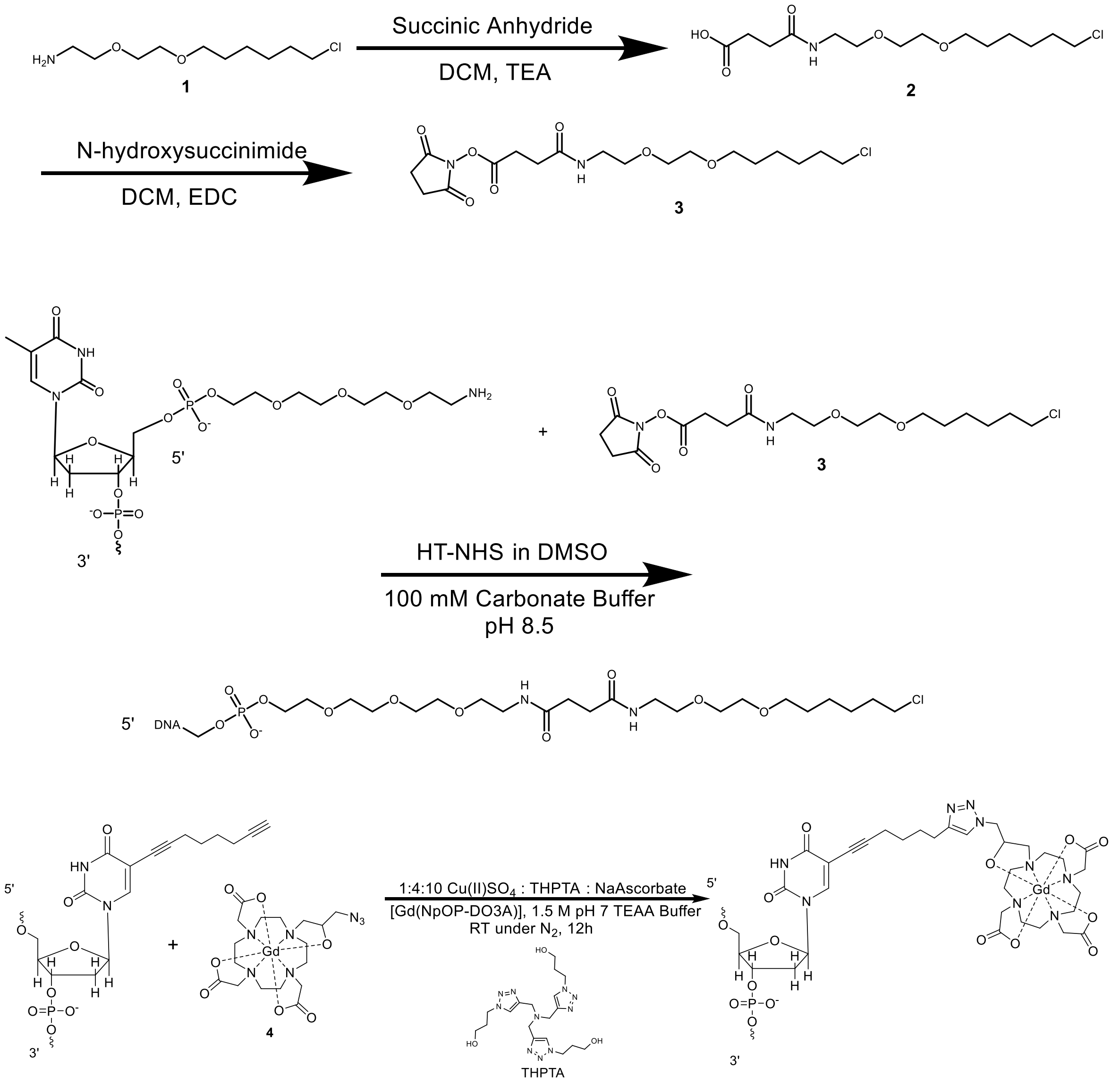

Figure 2.2. Synthetic schemes for nanoparticle synthesis.

Compound **1** and complex **4** were synthesized using previously reported procedures (81, 82). Briefly, a HaloTag-targeting moiety is functionalized with a carboxylate to enable the formation of an NHS ester. This allows for peptide coupling to the amino group on the 5’ end of the poly-T DNA strand. In a separate reaction, azide-functionalized Gd(III) chelates are attached to alkyne-functionalized bases through a Cu(I)-catalyzed 1,3 dipolar cycloaddition

The U-2 OS HT-ECS (HT+) cell line constitutively expresses extracellular HaloTag. Flow cytometry was used to quantify the number of HaloTag proteins expressed on the outer surface of the plasma membrane by using cell-impermeable HaloTag-targeted AlexaFluor488 dye. Unlike antibody-based cell surface stains, each HaloTag protein binds irreversibly to only one molecule of AlexaFluor488 *(68).* Therefore, the number of HaloTag proteins present on the surface of these cells could be quantified by fluorescence. The HT+ cell line was observed to express 1,800,000 ± 500,000 copies of HaloTag on its surface (Figure 2.3). Using the common volume approximation of 2 pL/cell, this yields a concentration of 1.6 ± 0.4 μM HaloTag that is accessible to the cell surface (83). Though this concentration of HaloTag corresponds to the top decile of protein expression in the mammalian cell, a Gd(III) agent bound to HaloTag in one-to-one stoichiometry would still fail to achieve a detectable concentration (57).

This theoretical prediction was tested explicitly. A HaloTag-targeted Gd(III) contrast agent (HTGd) had previously been reported (Figure 2.4) (50). This contrast agent was synthesized in order to show that complete binding of cell-surface accessible HaloTag would result in a Gd(III) concentration below the detection limit. Flow cytometry was used to measure binding of HTGd to HaloTag on the plasma membrane. HT+ cells were first incubated with 1 mM HTGd, followed by labeling with HaloTag-targeted AlexaFluor488. When HTGd binds to HaloTag on the cell surface, fewer sites remain for AlexaFluor488 binding. Therefore, HTGd binding to HaloTag was monitored by the loss of AlexaFluor488 fluorescence (Figure 2.4). Loss of fluorescence indicated that 93% of HaloTag sites were occupied by HTGd. Nonetheless, cell pellet images show no contrast enhancement over unlabeled cells (Figure 2.4)

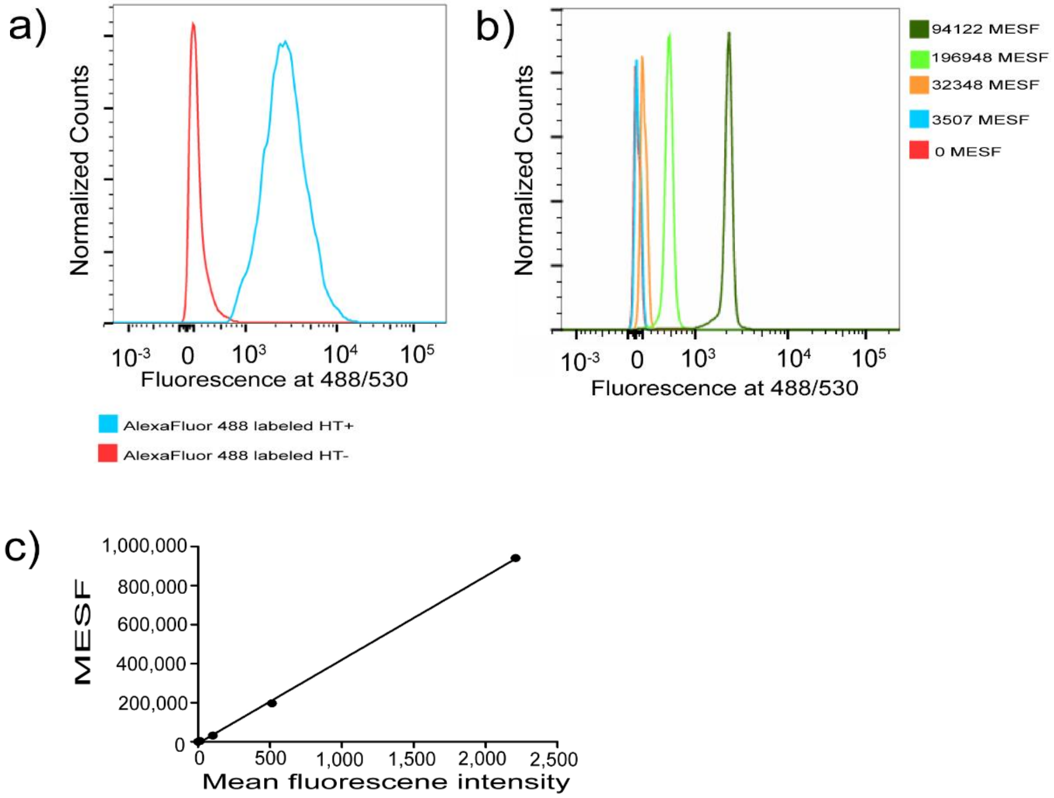

Figure 2.3 Procedure for quantifying the expression level of HaloTag on the surface of U-2 OS HT cells. a) Flow cytometry data showing the fluorescence shift from HT+ cells compared to the fluorescence from the non-specific binding of AlexaFluor488-HT to U-2 OS cells. b) The fluorescence intensity measured from beads with known molecular equivalents of soluble fluorochrome (MESF) for AlexaFlour488 (Bang's Lab) and c) the corresponding standard curve.

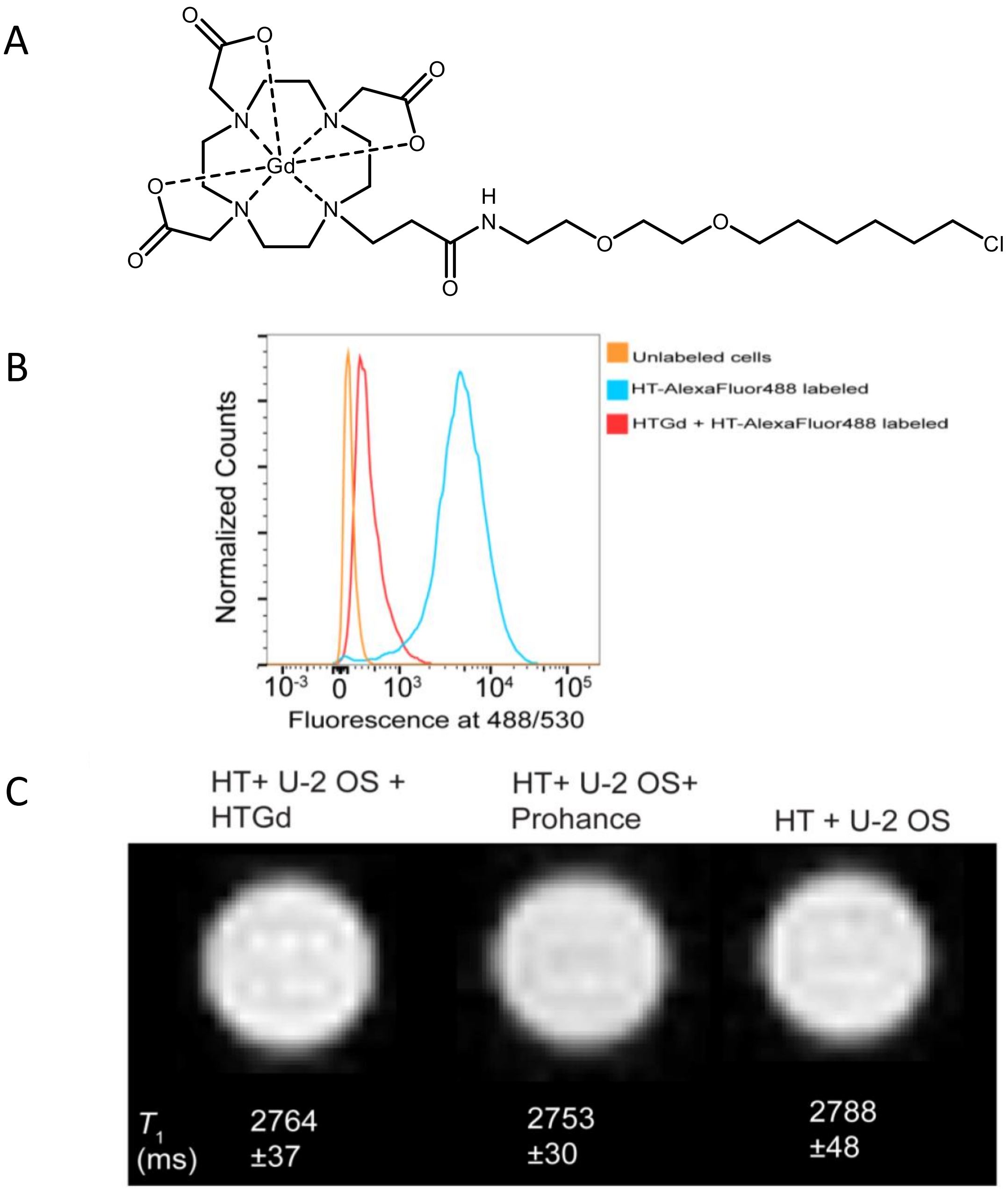

Figure 2.4 Experimental validation of the calculated detection limit for Gd(III).

a) Chemical structure of HTGd. b) Flow cytometry data showing that HTGd can effectively prevent HaloTag-targeted AlexaFluor488 from binding to HaloTag, indicating binding. c) Cell pellet images confirming that even when fulling occupied by Gd(III), there is insufficient expression of HaloTag to be detectable by MRI. HT+ cells were treated with either 1 mM HTGd, 1mM Prohance, or left untreated. In all three cases no difference in contrast is or T_1 times.

To directly observe AuDNA-Gd(III)-HA binding to HaloTag, transmission electron microscopy (TEM) was used to identify membrane binding. A change in the subcellular localization of AuDNA-Gd(III)-HA was observed when comparing HT+ cells to otherwise identical cells that do not express HaloTag (U-2 OS (HT-)) (Figure 2.5). Both cell lines showed intracellular clusters of nanoparticles, which are likely endosomes or lysosomes. This observation is consistent with the previously proposed mechanism of scavenger receptor uptake (77). However, only HT+ cells showed large numbers of particles adjacent to the plasma membrane.

Flow cytometry was used to measure binding of AuDNA-Gd(III)-HA to HaloTag on the plasma membrane. After a 24-hour incubation period, HaloTag binding was observed to plateau at an incubation concentration of 40 nM nanoparticles, with greater than 60% binding as low as 10 nM (Figure 2.5). In addition, HaloTag was saturated after 8 hours of incubation at 40 nM (Figure 2.5). The binding kinetics of AuDNA-Gd(III)-HA are slower than HaloTag-targeted small molecules (68). This is likely the result of a complex protein corona that forms around nanoparticles when exposed to serum proteins and reduces access to targeting groups (84, 85). Importantly, these data suggest that saturated cells will have an average of 1,730,000 nanoparticles associated with the cell as a result of HaloTag binding. If each particle contributes 500 Gd(III) chelates, we predict that HaloTag saturation will result in 1.5 fmol Gd(III)/cell. This concentration is an order of magnitude above the most conservative estimates for the detection limit (56).

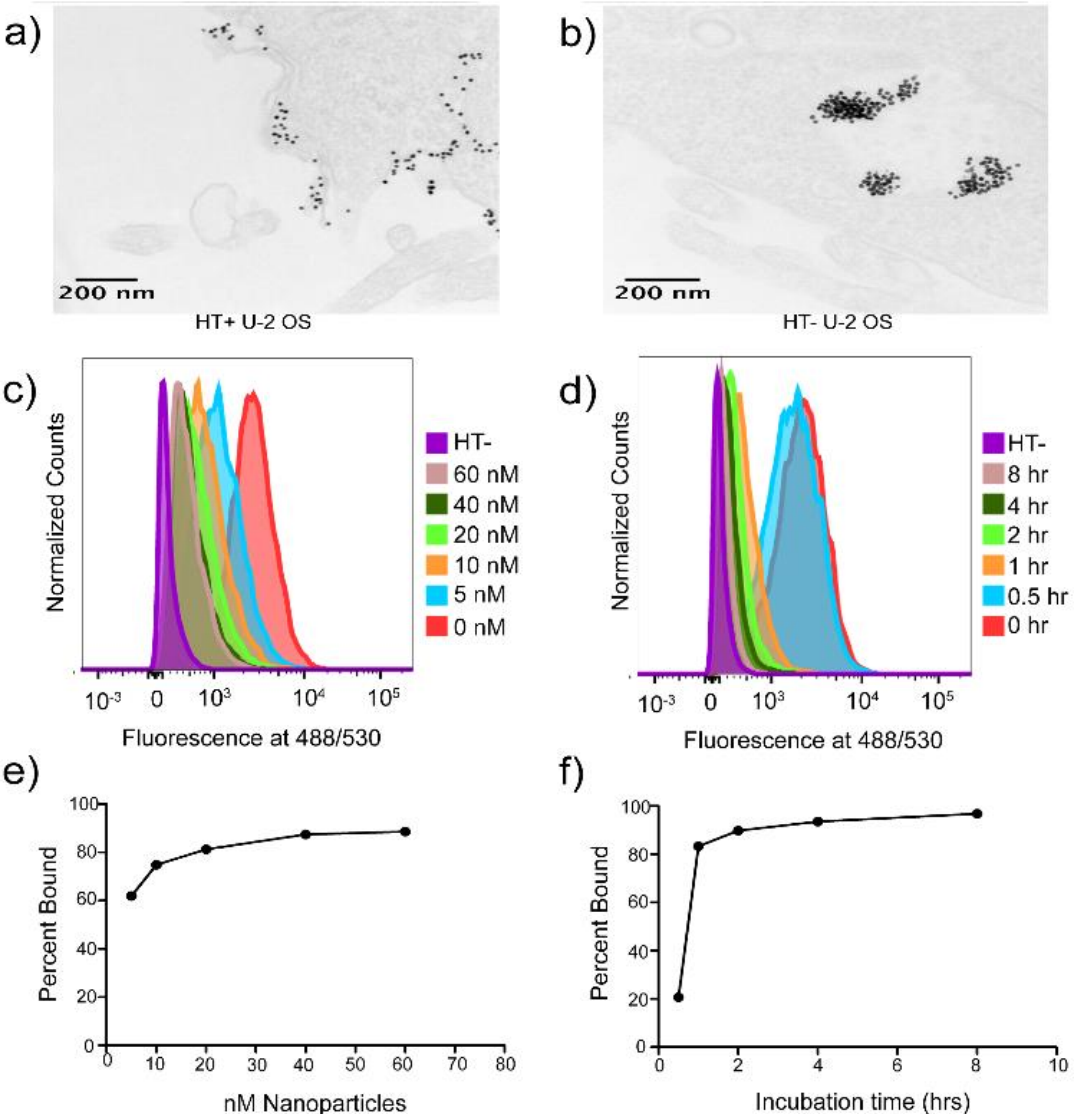

Figure 2.5 AuDNA- Gd(III)-HA nanoparticles bind the HaloTag protein on the cell surface.

a) and b) display the transmission electron microscopy images of HT+ cells and HT- cells, respectively, after incubation with 20 nM AuDNA-Gd(III)-HA. The expression of surface HaloTag changes the subcellular localization of AuDNA- Gd(III)-HA nanoparticles. AuDNA- Gd(III)-HA nanoparticle binding to HaloTag can be monitored by flow cytometry. HaloTag expressing cells labeled with HaloTag-targeted AlexaFluor488 after incubating with AuDNA-Gd(III)-HA at c) various concentrations for 24 hours or for d) various times at 40 nM. The percent of HaloTag proteins bound to nanoparticles can be extracted from this data. e) and f) show the binding curves corresponding to the concentration gradient and time course respectively

To determine the accuracy of these uptake approximations, HT- and HT+ cells were incubated with AuDNA-Gd(III)-HA and Gd(III) uptake was measured using ICP-MS. These data can be used to determine the signal contributions that depend on the expression of HaloTag and untargeted uptake of AuDNA-Gd(III)-HA. It is likely that untargeted uptake of AuDNA-Gd(III)-HA is due to AuDNA nanoparticles binding scavenger receptors, as previously reported (77). HT- cells display saturation for both incubation concentration and time, which is the expected trend as available scavenger receptors are depleted (Figure 2.6). The Gd(III) uptake values for HT+ cells continue to increase beyond the measured values for HT- cells at several time points and concentrations (Figure 2.6). After 8 hours of incubation with 40 nM AuDNA-Gd(III)-HA, HT+ cells accumulated threefold more Gd(III) than HT- cells (Figure 2.6). HaloTag expression resulted in an additional accumulation of 1.16±0.08 fmol Gd(III)/cell over HT- cells. This value is very close to the predicted value of 1.5 fmol Gd(III)/cell calculated from the expression level of HaloTag (Figure 2.5). A likely explanation for the reduced uptake is slow degradation of the nanoparticles over the course of the incubation. While AuDNA nanoparticles are resistant to the activity of DNase, the reaction still proceeds at a measurable rate (74).

Cell pellet MR images were taken to verify that the additional uptake conferred by HaloTag expression would effectively translate to contrast in an MR image acquired at 7 T. As expected, both cells lines showed an increase in signal intensity over unlabeled cells after incubation with AuDNA-Gd(III)-HA (Figure 2.6). Significantly, HaloTag-expressing cells are clearly distinguishable from cells that do not express HaloTag. From this image the contrast-to-noise ratio (CNR) between HT+ and HT- cells was calculated to be 9.4. Based on the clinical standard for MR imaging, CNR values above 5 are considered to be visually “obvious.”(55)

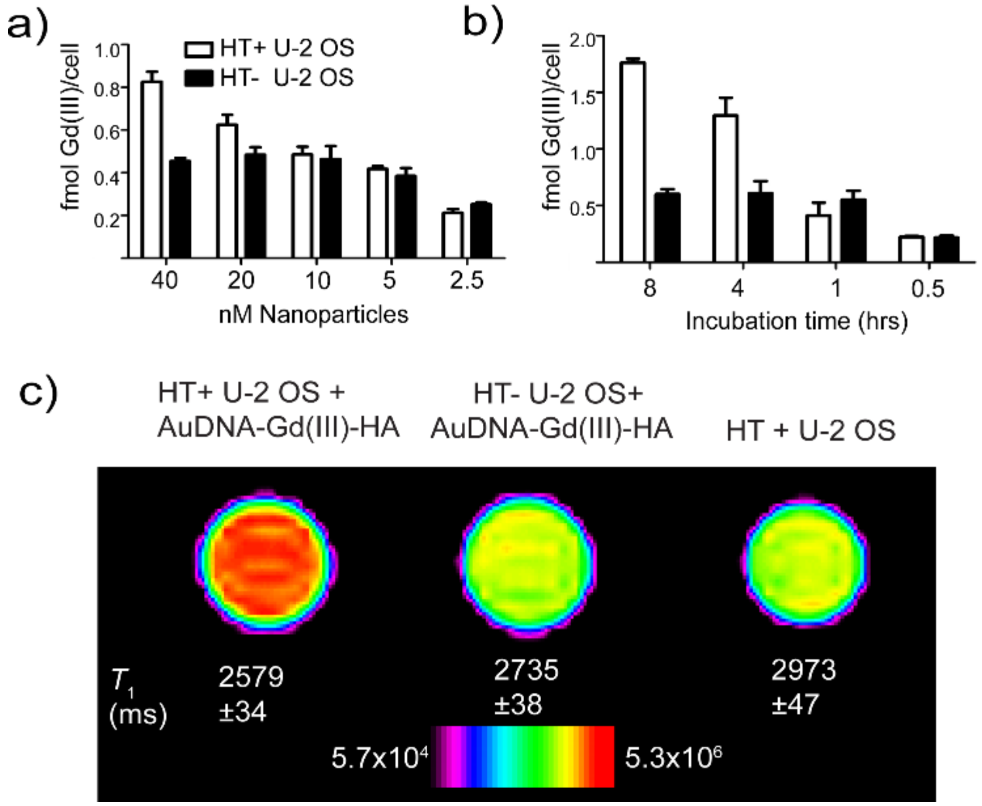

Figure 2.6 Cellular uptake of Gd(III) is measured for both HT- (black bars) and HT+ (white bars) cell lines using ICP-MS.

a) The concentration dependence of uptake was measured using a 24 hour incubation for each concentration. b) Cells were incubated with 40 nM nanoparticles for the indicated time. The expression of HaloTag results in measurably higher uptake of Gd(III). Error bars show standard error of the mean. c) HaloTag-dependent contrast enhancement is clearly visible after incubation with AuDNA-Gd(III)-HA at a concentration of 52 nM nanoparticles for 8 hours. Gradient bar denotes signal intensity. Error bars indicated standard error of the mean.

2.3 Conclusion and Future Directions

There have been several attempts to create a method to report on gene expression via MRI. This goal has proven to be difficult to obtain, and while there are many options for MR reporter genes, there is no clearly superior option. The probe described herein has identifiable strengths and weaknesses. It produces positive contrast (which is preferable over negative contrast) and is incorporated into an existing reporter gene platform. However, the amount of contrast generated is exceeded by other reporter genes and this approach suffers from non-specific uptake that will further limit its applicability (67). However, both of these weaknesses can be addressed through additional iterations of probe design.

This work is the first study to explicitly link theoretical calculation for the detection limit of Gd(III) to experimental results, in the context of protein targeting. Prior to 2011, it was difficult to obtain quantitative expression level data for many proteins in the proteome (57). As a result, even successful instances of protein-targeted contrast enhancement rarely quantified the component of contrast that was dependent on binding (54, 61, 63). This body of work has the potential to guide design decision for other protein-targeted probes and aid in selection of targets.

2.4 Materials and Methods

2.4.1 Probe synthesis

DNA Strand Synthesis

The first step in synthesizing the DNA strand required the use of a DNA synthesizer. In total, the DNA strand taken form the synthesizer would consist of a 24mer poly-T strand with a 3’ disulfide, 5’ amine for peptide coupling, and five thymidine bases modified with an alkyne for Cu(I)-catalyzed 1,3 dicycloadditions. Oligonucleotides were synthesized on solid phase controlled pore glass beads (CPGs) by standard techniques on a MerMade automated synthesizer. DNA purifications were performed on an Agilent dynamax 250 x 10 mm microsorb 300-10 C18 column using a linear gradient of 0% acetonitrile in 150 mM triethylammonium acetate buffer to 75% acetonitrile in 45 minutes on a Varian Prostar 500, with a flow rate of 3 mL/min. Synthesis of the alkyne modified oligonucleotide was performed on 3’ thiol modifier C3 disulfide controlled pore glass beads (Glen Research) using C8-alkyne dT phosphoramidite (Glen Research) for the five internal modifications, indicated as T*, and 5' amino modifier TEG phosphoramidite (Glen Research) indicated as NH_2. The synthesized oligonucleotide consisted of the sequence 3' – S-S-TTT-TTT-TTT-T*TT-T*TT-T*TT-T*TT-T*TT–NH_2 5'. Deprotection of the oligonucleotide from the resin was performed using standard 1:1 AMA conditions (ammonium hydroxide:methylamine) at 55 °C for one hour. Strands were filtered away from CPGs, purified by reverse phase HPLC, and characterized by MALDI-MS.

The resulting DNA strand was then functionalized with Gd(III) to confer relaxivity to the particle. The synthetic scheme for this reaction is shown in Figure 2.2. Complex **4** was synthesized using previously published methods (82). Covalent attachment of Gd(III) complex **4** to DNA begins with dissolution of 1 µmol of the 5x alkyne bearing HT-poly dT DNA from above, into 500 µL of 1.5 M triethylammonium acetate buffer pH 7. To the mixture (via stock solutions according to Hong, et. al.) (86) is added 100 nmol Cu(II) sulfate, 500 nmol tris-hydroxypropyl triazolyl amine, 10 µmol of **4**, and 1 µmol sodium ascorbate. The reaction vessel is capped and allowed to stir overnight. The reaction mixture was analyzed by MS-MALDI to verify that the reaction had reached completion with 5 Gd(III) chelates per DNA strand. The resulting 5x Gd(III)-HT DNA complex is then purified by reverse phase HPLC and characterized by MS-MALDI.

The DNA strand was completed by functionalizing it with a HaloTag-targeting moiety. The synthesis for HaloTag functionalization is shown in Figure 2.2 Briefly, a HaloTag targeting group with an amine functionality was synthesized according to previously published methods. The amine functionality was replaced with a carboxylic acid through a succinic anhydride ring opening. Finally, an n-hydroxysuccinimide (NHS) ester was generated for reaction with the free amine on the DNA.

*4-((2-(2-((6-chlorohexyl)oxy)ethoxy)ethyl)amino)-4-oxobutanoic acid (**2**)*

An amine terminated HaloTag-targeting group (**1**) was synthesized according to literature methods (81). To a flame dried flask was added **1** (0.220 g, 0.983 mmol) and succinic anhydride (0.590 g, 5.90 mmol). The flask was then placed under vacuum for 60 minutes. The contents of the flask were dissolved in 50 ml dichloromethane (DCM) followed by the addition of triethylamine (0.121 g, 12.0 mmol). The solution was allowed to stir for 48 hours under nitrogen. The resulting mixture was concentrated *in vacuo*, diluted in 1 M HCl, and extracted into ethyl acetate (3 x 30 ml). The organic layer was dried over sodium sulfate and concentrated *in vacuo*. The resulting mixture was purified by reverse phase semi-preparative HPLC with an XBridge prep C18 column. The desired product appears as a colorless oil and was characterized by NMR

*2,5-dioxopyrrolidin-1-yl 4-((2-(2-((6-chlorohexyl)oxy)ethoxy)ethyl)amino)-4-oxobutanoate (**3**)*

To a flame dried flask was added **2** (0.144 g, 0.445 mmol), NHS (0.153 g, 1.33 mmol), and 0.5 g sodium sulfate. The flask was then left under vacuum for 60 minutes and then placed under nitrogen. 30 ml of anhydrous DCM was added to the flask and allowed to stir for 30 minutes until the NHS was fully dissolved. 1-Ethyl-3-(3-dimethylaminopropyl)carbodiimide (EDC) (0.104 g, 0.670 mmol) was injected into the flask and the solution was allowed to stir at room temperature for 16 hours. The resulting mixture was concentrated *in vacuo* yielding a dark brown oil. This oil was dissolved in a 1:1 suspension of water and ethyl acetate, extracted into ethyl acetate (3x3 ml), and characterized by ESI-MS. The resulting NHS-ester was concentrated *in vacuo* and used immediately.

HaloTag-Targeted DNA

Addition of the HaloTag targeting functionality was performed off CPG and began with 1 μmol of 5x alkyne modifier-NH_2 poly dT DNA in 500 μL of 100mM pH 8.5 carbonate buffer (Scheme S2). To the mixture is added to 5 mg of freshly extracted HT NHS ester (**3**) in 100 μL of DMSO. The reaction is allowed to stir overnight and is observed to be complete by full reaction of starting DNA by MALDI-MS. Intermediate HT-DNA is purified by reverse phase HPLC and characterized by MALDI-MS.

Nanoparticle Construction

AuDNA-Gd(III)-HA was completed by binding the DNA strand to the nanoparticle using a salt aging procedure. Specifically, 29 OD (260 nm) of DNA (corresponding to ~200 strands of DNA per nanoparticle) was dried into a 1.5 mL microcentrifuge tube, to which is added 300 μL of 100 mM dithiothreitol in 180 mM (pH 8.0) phosphate buffer. The solution is left to stir at room temperature for 1 hour. After such time, the DNA is run through a pre-packed G25 sephadex column (NAP-5, GE life sciences) using 180 mM phosphate buffer as the mobile phase, monitoring elution by UV/Vis at 260 nm.

To 50 mL of 10 nM citrate stabilized gold nanoparticles in water is added 54 µL of tween 20 (for a total concentration of 0.01% v/v) and deprotected and purified DNA in 4 mL 180 mM phosphate buffer. The solution is then sonicated for 30 seconds and left to stir for 30 minutes. Over the subsequent five hours, a solution of NaCl (4.753 M), phosphate buffer (10 mM) and 0.01% tween 20 is added in increments of 1.25, 1.29, 1.32, 1.35 and 1.38 mL per hour, with each addition followed by 30 seconds of sonication. During the intervening time, the solution is left to stir at room temperature. The final concentration of NaCl is 600 mM. The solution is left to stir for a further 48 hours.

Purification of AuDNA-Gd(III)-HA is conducted by three rounds of centrifugation at 4 °C (30 minutes at 21.1 x g), followed by resuspension in fresh DPBST (0.01% Tween20). This procedure yielded up to 4 nmol AuDNA-Gd(III)-HA from 5 nmol citrate stabilized gold nanoparticles.

2.4.2 Probe Characterization

*T*he finished AuDNA-Gd(III)-HA nanoparticle was characterized for size and ligand density. The size of the nanoparticles prior to DNA functionalization was measured for two separate batches using transmission electron microscopy (Figure 2.7). After functionalization, DNA ligand density was measured by ICP-MS. This technique yielded a quantitative measure of both Au and Gd(III) concentration. From this data, ligand density can be determined by calculating the volume of the nanoparticle assuming a perfect sphere and the atomic density of bulk gold (59.1 atoms/nm^3). Gd(III) was related to DNA concentration because it is known that each DNA strand contains 5 Gd(III) atoms. Stability was monitored by UV-Vis (Figure 2.7).

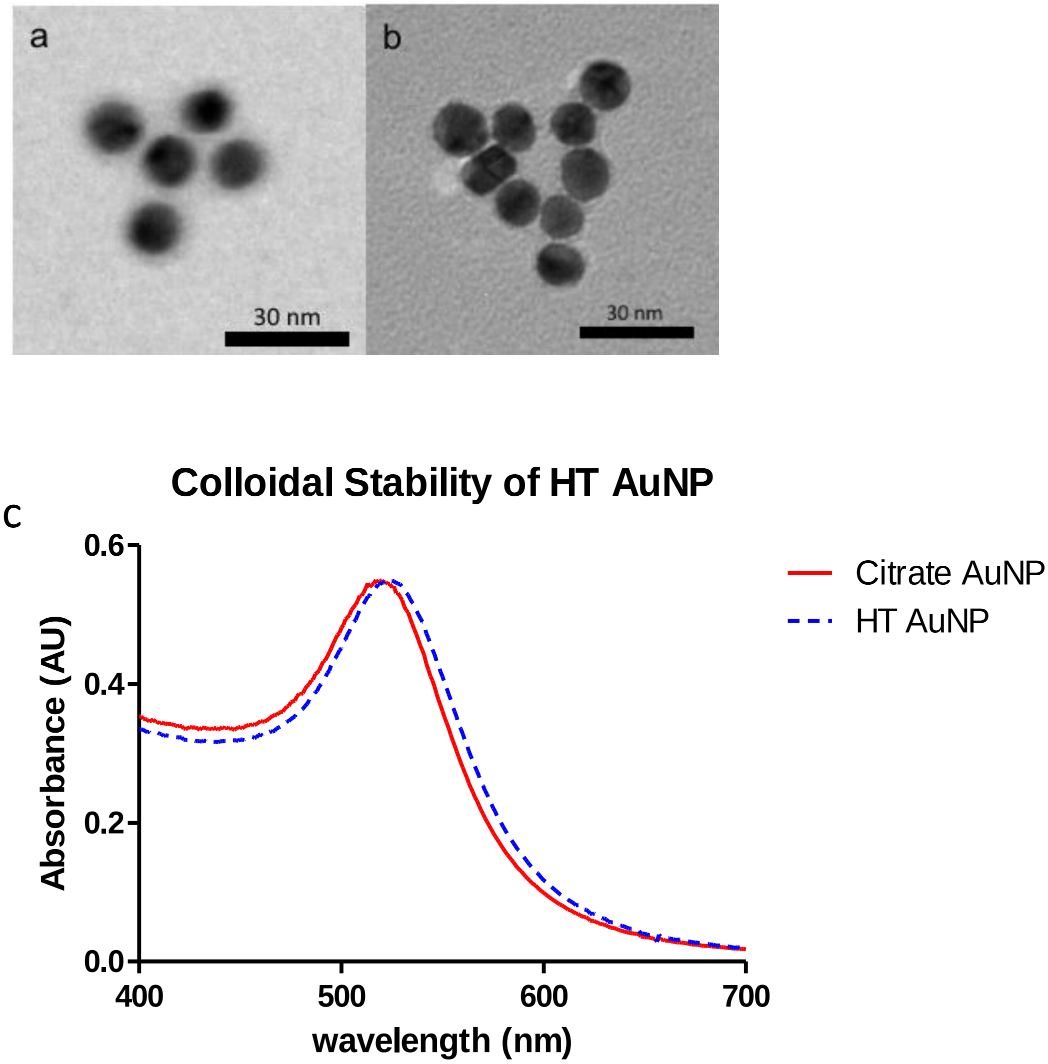

Figure 2.7 Characterization of nanoparticles.

a) and b) display TEM data from two different batches of nanoparticles. c) shows UV-Vis data for nanoparticles before and after functionalization with DNA.

Relaxivity

Both the T_1 and T_2 relaxivities were measured. A stock solution of AuDNA-Gd(III)-HA conjugates was made (700 µL). Serial dilution was performed four times for a total of five solutions. Solutions were heated to 37 °C and 200 µL of each dilution was measured for T_1 relaxation time. Data were collected using an inversion recovery pulse sequence using 4 averages, a 15 s repetition time and 10 data points. The remaining volumes of each solution were utilized for ICP analysis of [Gd(III)]. The inverse of the longitudinal relaxation time ($1/T_1$, s^{-1}) was plotted versus the Gd(III) concentration (mM). By applying a linear fit to this data, the slope that is generated is defined as the relaxivity of the agent (mM^{-1} s^{-1}).

2.4.3 Cell culture techniques

U-2 OS (ATCC) and U-2 OS HT-ECS (Promega) were cultured in McCoy's 5A media supplemented with 10% fetal bovine serum (VWR) (FBS) at 37°C and 5% CO_2. U-2 OS HT-ECS is stably transfected with a HaloTag expression vector that includes a neomycin resistance gene. Therefore, U-2 OS HT-ECS media included 800 µg/ml G418 (Life Technologies).

HaloTag-Targeted Fluorescence Labeling

Cells were labeled by first treating them with trypsin, follow by inhibition with media, and collected into microcentrifuge tubes. The cells were then pelleted at 1000g for 5 minutes at 4°C. Media labeled with 1:1000 HaloTag-targeted AlexaFluor488 (Promega) was used to resuspend the cells. After a 15 minute incubation at 37°C, cells were pelleted at 1000g for 5 minutes at 4°C, resuspended in 400µL DPBS, spun down again, and finally resuspended in DPBS with 2% bovine serum albumin for flow cytometry. Analysis was performed on a LSR II (BD) flow cytometer and data were analyzed using FlowJo software (Treestar).

TEM

For transmission electron microscopy (TEM) imaging of cells, cell fixation was conducted in a Pelco Biowave microwave systems with cold spot and vacuum chamber. Cell pellets were fixed twice using

Karnovsky's fixative. The cells were then washed three times with sodium phosphate buffered saline. The sample was then enrobed in a gel of 2% agarose to promote pellet integrity through the embedding process. 2% OsO4 in water was applied as an additional fixative and to promote image contrast. The enrobed pellet was then washed with water and dehydrated with acetone washes. EMBed 812 resin (Electron Microscopy Sciences) was used for embedding. The resin was polymerized at 60 degrees C. Sectioning was conducted using a Leica Ultracut S. The resin was sliced to 90 nm thickness and collected on copper mesh grids. TEM was conducted using a 1230 JOEL transmission electron microscope. All imaging was carried out at 100 keV accelerating voltage.

Uptake and Viability

Cells were incubated with the indicated concentration of AuDNA-Gd(III)-HA for the indicated amount of time. They were then rinsed in the plate once with Dulbecco's phosphate buffered saline (DPBS), trypsinized, treated with trypsin inhibitor, and collected into microcentrifuge tubes. The cells were then pelleted at 1000g for 5 minutes at 4°C. Cell pellets were washed twice by resuspending in 400μL DPBS and pelleting.

Cells were counted and viability was measured as part of cell uptake experiments using a Guava EasyCyte Mini Personal Cell Analyzer. After cell resuspension, an aliquot (50 μL) of the suspension was diluted in Guava ViaCount reagent (150 μL). Stained samples were vortexed for 10 s and then cells were counted using a Guava EasyCyte Mini Personal Cell Analyzer (PCA) using the ViaCount software module***.*** Viability was measured using the EasyFit software module (Figure 2.8).

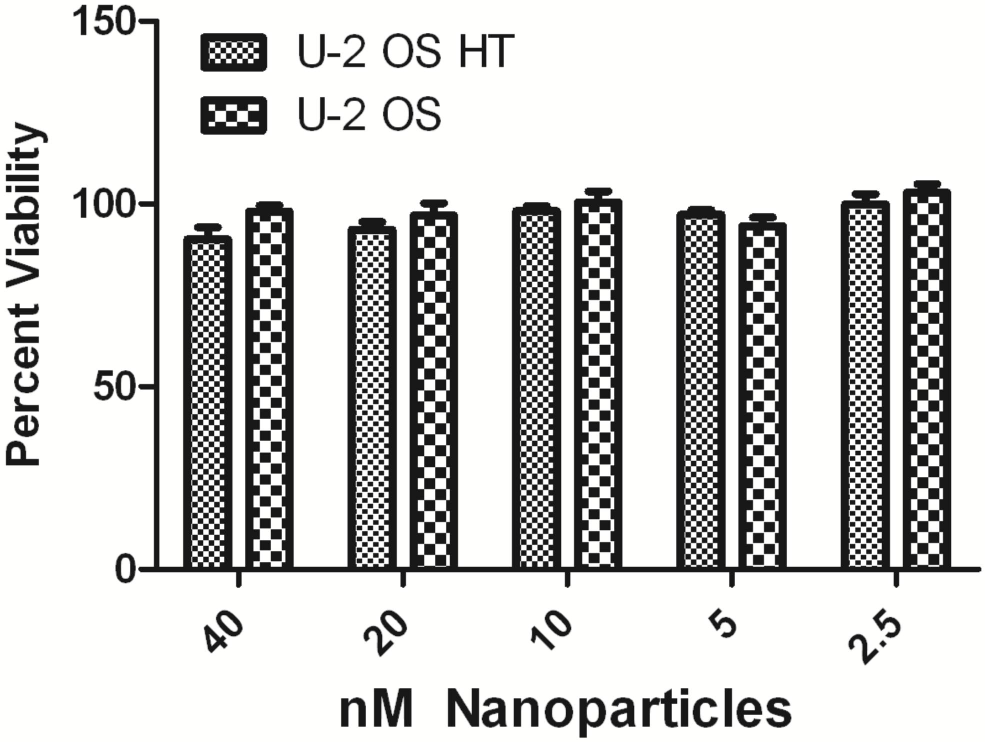

Figure 2.8 Percent viability of both U-2 OS HT and U-2 OS is measured after incubation with AuDNA-Gd(III)-HA.

After a 24 hour incubation no significant loss of viability is measured at concentrations as high as 40 nM AuDNA-Gd(III)-HA.

Quantification of gadolinium for cell uptake experiments was accomplished using ICP-MS of acid digested samples. Specifically, aqueous samples were digested in concentrated nitric acid (> 69%) and hydrochloric acid (37% BDH) and heated to 75 °C for overnight. Samples were then diluted with ultra-pure H_2O (18.2 MΩ·cm) and multi-element internal standard (CLISS-1, Spex Certiprep) to 3.0% nitric acid (v/v) and 5.0 ng/mL internal standard in a total sample volume of 3 mL. Individual Gd elemental standards were prepared at 0.78125, 1.5625, 3.125, 6.25, 12.5, 25.0, 50.0, 100, and 200 ng/mL concentrations with 3.0% nitric acid (v/v) and 5.0 ng/mL internal standards up to a total sample volume of 10 mL.

ICP-MS was performed on a computer-controlled (Plasmalab software) Thermo X series II ICP-MS (Thermo Fisher Scientific) operating in standard mode equipped with a CETAC 260 autosampler. A survey run and 3 main runs were acquired for each sample. For data interpolation and machine stability ^{157,158}Gd, and ^{115}In and ^{165}Ho were analyzed.

Cell pellet images

Adherent cells were incubated with 52 nM nanoparticles for 8 hours in T25 flasks, or with 100 µM Prohance or HTGd for 30 minutes in T25 flasks. After incubation the labeled media was removed and cells were washed once with DPBS. Cells were then trypsinized and collected into 1.5 ml microcentrifuge tubes. Cells were pelleted at 1000 g for 5 m, resuspended in 1 ml DPBS, and spun down again. This was repeated one more time. Cells were finally resuspended in 1 ml DPBS, placed into flame-sealed pipettes, pelleted at 100 g for 5 minutes, and imaged.

In order to determine Spin-lattice relaxation times (T_1), a rapid-acquisition rapid-echo (RARE-VTC) T_1-map plus sequence with static TE (11 ms) and variable TR (150, 250, 500, 750, 1000, 2000, 4000, 6000, 8000, and 10000 ms) values was used. The imaging parameters were: field of view (FOV) = 25 × 25 mm^2, matrix size (MTX) = 256 × 256, number of axial slices = 4, slice thickness (SI) = 1.0 mm, and averages (NEX) = 3 (total scan time = 2 h 36 min). T_1 analysis was carried out using the image sequence analysis tool in Paravision 5.0 pl3 software (Bruker) with monoexponential curve-fitting of image intensities of regions of interest (ROIs) for each axial slice.

Chapter Three

Stilbene-Conjugated Gd(III) Chelates for the Detection of Amyloid Plaques by Magnetic Resonance Imaging

3.1 Introduction

Amyloidoses are a broad class of protein misfolding diseases characterized by proteins transitioning from a functionally folded to state to a dysfunctional amyloid state. The most prominent amyloidosis is Alzheimer's disease, which is believed to affect 26 million people worldwide, with an estimated annual cost of 32 billion (87, 88). In addition to Alzheimer's disease, there are more than three dozen distinct amyloid diseases that affect human health including Parkinson's disease, type II diabetes, and Huntington's disease. Each one of these diseases features characteristic amyloid plaques that can either be localized to specific organs or distributed systemically. It is not known what role the plaques play in the pathophysiology of some amyloidosis, but they are characteristic of disease burden, making them a valuable diagnostic indicator.

Despite their impact on human health, diagnosing amyloids presents major challenges. For the majority of amyloidosis, the only method to conclusively diagnose them is through a biopsy (89). However, biopsies possess several shortcomings in regard to diagnosis. First, biopsy is unavailable for surgically inaccessible areas, such as the brain. Second, biopsies only reflect a sample of tissue and therefore are unable to reflect the overall disease burden throughout the tissue. Third, by virtue of being invasive, biopsies are ill-suited for longitudinal studies. In contrast, an appropriate non-invasive imaging technique that could detect amyloids would alleviate these concerns.

Although amyloid proteins have broadly dissimilar sequences, their structures are remarkably similar. Amyloids have certain structural features in common that drive the formation of large fibrils. These structures can exist even when they represent only a portion of the overall protein. β-sheets represent the majority of the amyloid secondary structure (Figure 3.1). Beta sheet monomers stack atop one another to form the axis of the fibril**,** with turns between β-sheets making up the remainder of the protein structure. Stacks of β-sheets then pack against one another to form larger protofibrils, and eventually mature fibrils. A key feature of amyloid structure is a "hydrophobic zipper" in which side chains between adjacent beta sheets interlock and exclude water. On the hydrated exterior of the fibril, the beta sheet structure produces long grooves that are bounded on either side by repeats of the same amino acid (Figure 3.1).

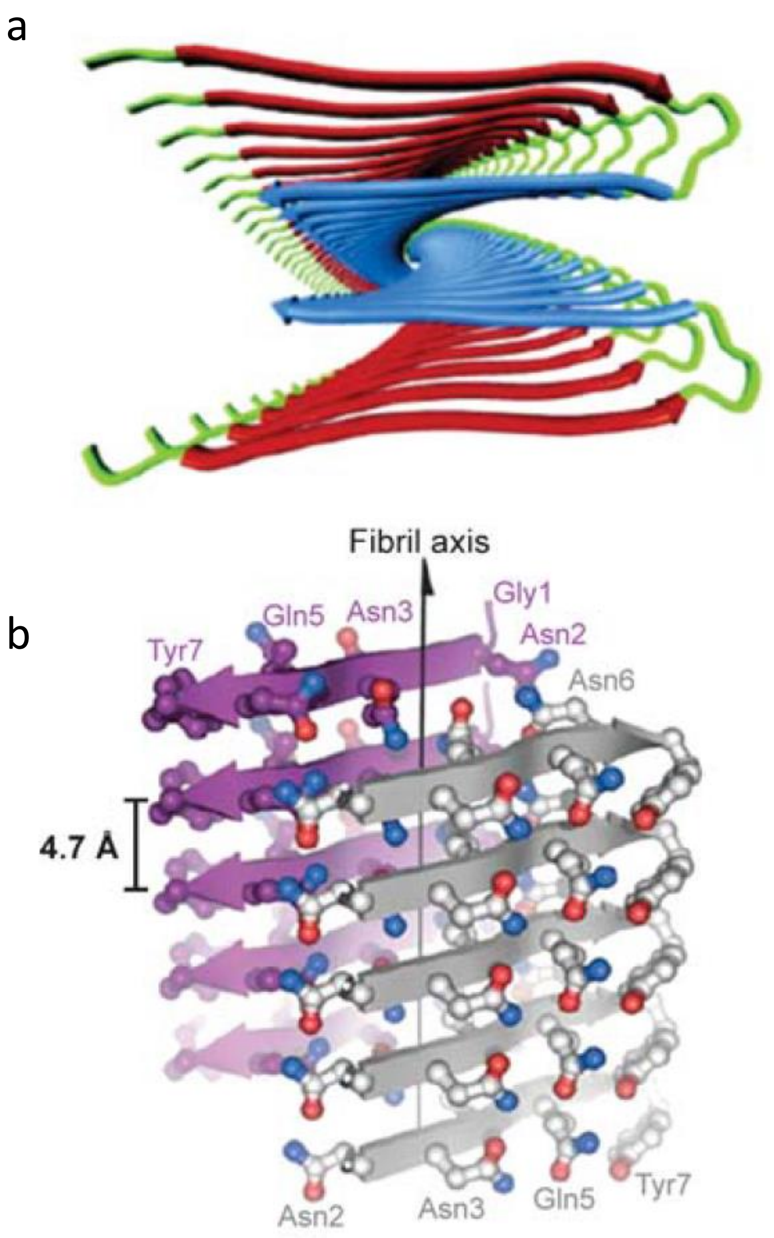

Figure 3.1 Structural models of two example amyloid fibrils.

a) A view down the long axis of the Aβ protofibril. The blue and red subunits join together with a steric zipper, which excludes water and shields hydrophobic residues. b) The crystal structure of the amyloidogenic portion of amyloid forming peptide (GNNQQNY). The exterior amino acids produce channels along the long axis of the fibril. Reproduced with permission from Chiti, F. & Dobson, C.M. Annual Review of Biochemistry 2006.

The long channels formed on the outside of fibrils serve as a common structural element. Several classes of molecules have the capacity to bind to amyloids in general, with little regard for the amyloid's primary structure. All of these molecules have in common a planar geometry and a large conjugated domain (Figure 3.2). Molecules in the Congo Red, Thioflavin T, Styryl, and amino-napthyl groups can typically bind to amyloids. Such agents are fluorescent, and their optical properties have been instrumental in detecting the presence of amyloid plaques in histological sections and *in vitro* assays. In addition, several attempts have been made to image amyloids *in vivo*. Radiological imaging agents for Alzheimer's disease have bene a particularly active area of research, with one probe clinically approved (5). While radiotracers can take advantage of the high sensitivity offered by PET and SPECT, they suffer from a lower spatial resolution than MRI. In order to generate exogenous contrast in an MR image, contrast agents such as Gd(III) must be used. Despite the significant advantages of MRI over PET and SPECT, there are few instances in the literature of amyloid-targeted Gd(III) agents.

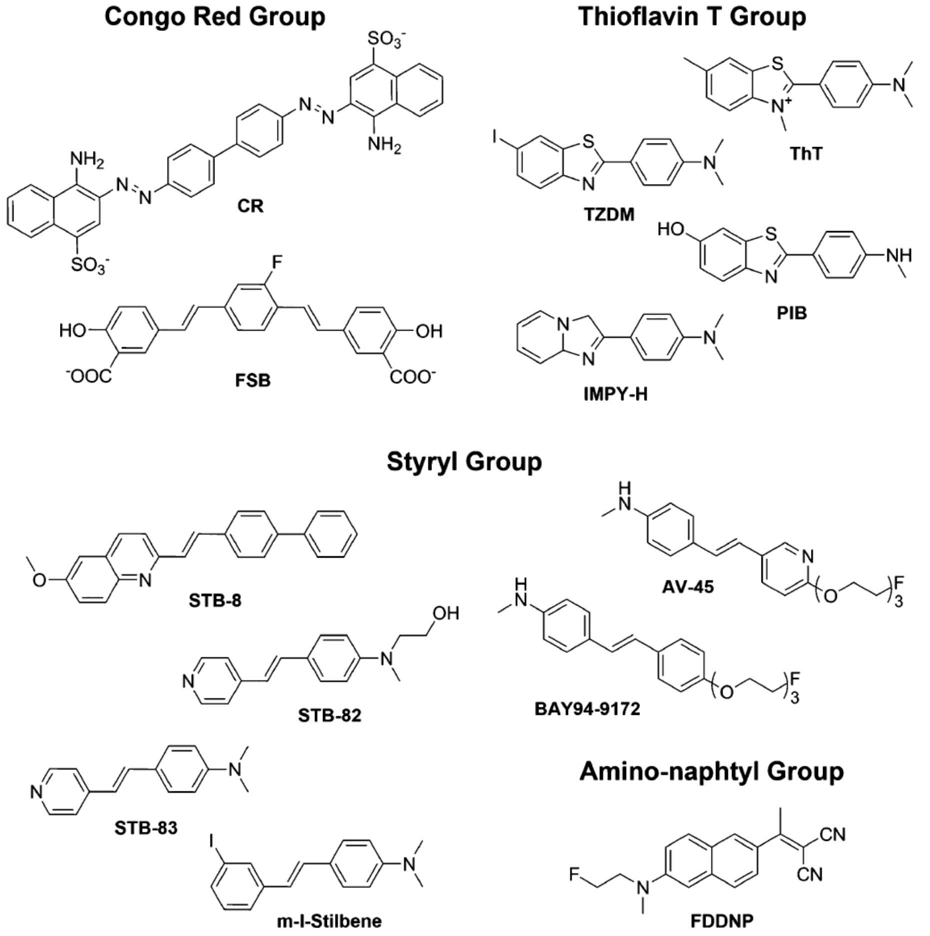

Figure 3.2 An overview of major structural groups of amyloid binding molecules.

Reproduced with permission from Kirkeby K. *et al*., JACS, 2013.

Designing a Gd(III)-based amyloid imaging agent presents several considerations unique from designing radiological probes. The key difference between is the significantly lower detection limit of Gd(III). As a result, any probe must be able to deliver high concentrations of agent to its target. This represent a major challenge for amyloid targeting, because amyloid-binding groups are typically very hydrophobic. Hydrophobicity in turn imparts higher toxicity and thus limits the maximum tolerable dose of the agent. Is therefore prudent to consider a variety of hydrophobicity profiles when creating amyloid-targeted MR probes. In addition, binding to amyloids may result in a longer τ_R, which can boost relaxivity at low field strength. This could help improve the sensitivity of the agent, as it would be brighter upon binding to its target.

3.2 Results and Discussion

The most important consideration for designing amyloid-targeting probes is balancing the need for a lipophilic amyloid binding group and the need for sufficient solubility to ensure favorable biodistribution. However, it is difficult to predict the solubility and biodistribution of a probe in the design phase. Therefore, two different contrast agent designs were explored for amyloid imaging (Figure 3.3). These designs were chosen for their synthetic accessibility and for their expected differences in solubility. Both rely on a stilbene moiety to provide lipophilicity and amyloid binding, and a macrocyclic Gd(III) chelate to provide MR contrast and high thermodynamic stability. The linkers offer differing lipophilicity, with the triazole group being much more hydrophilic than the alkyl group. In addition, these molecules should have very different molecular packing parameters, which will change the micellar properties in aqueous solution (90).

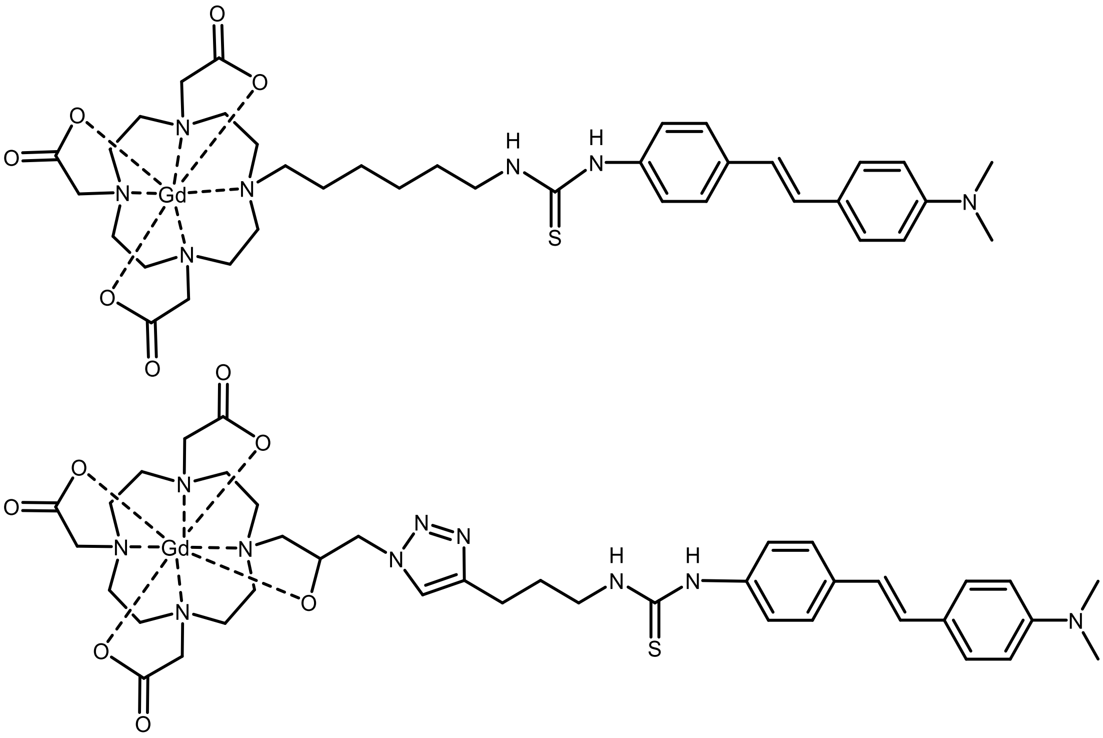

Figure 3.3 The structures of the proposed amyloid-targeted contrast agents.

Gd-Alkyl-SB (top) features a long alkyl chain linker whereas Gd-Triazole-SB incorporates a triazole moiety for increased hydrophilicity.

The simple synthetic scheme for the proposed molecules facilitates linker variation. Both synthetic schemes begin with a commercially available stilbene functionalized with an isothiocyante (Figure 3.4). This functional group creates a stable thiourea upon reaction with terminal amines. This property was used to couple stilbene to either **2** (synthesized using previous published techniques) or to incorporate an alkyne group (91). Coupling to **2** generates the complete Gd-Alkyl-SB, which was purified by extraction and characterized by analytical HPLC and electrospray-ionization mass spectrometry (ESI-MS). The alkyne-functionalized stilbene was purified by flash chromatography on silica and characterized by NMR and ESI-MS. This was further reacted with **1** to yield the finished Gd-Triazole-SB (Figure 3.4). HPLC was used to purify the complex.

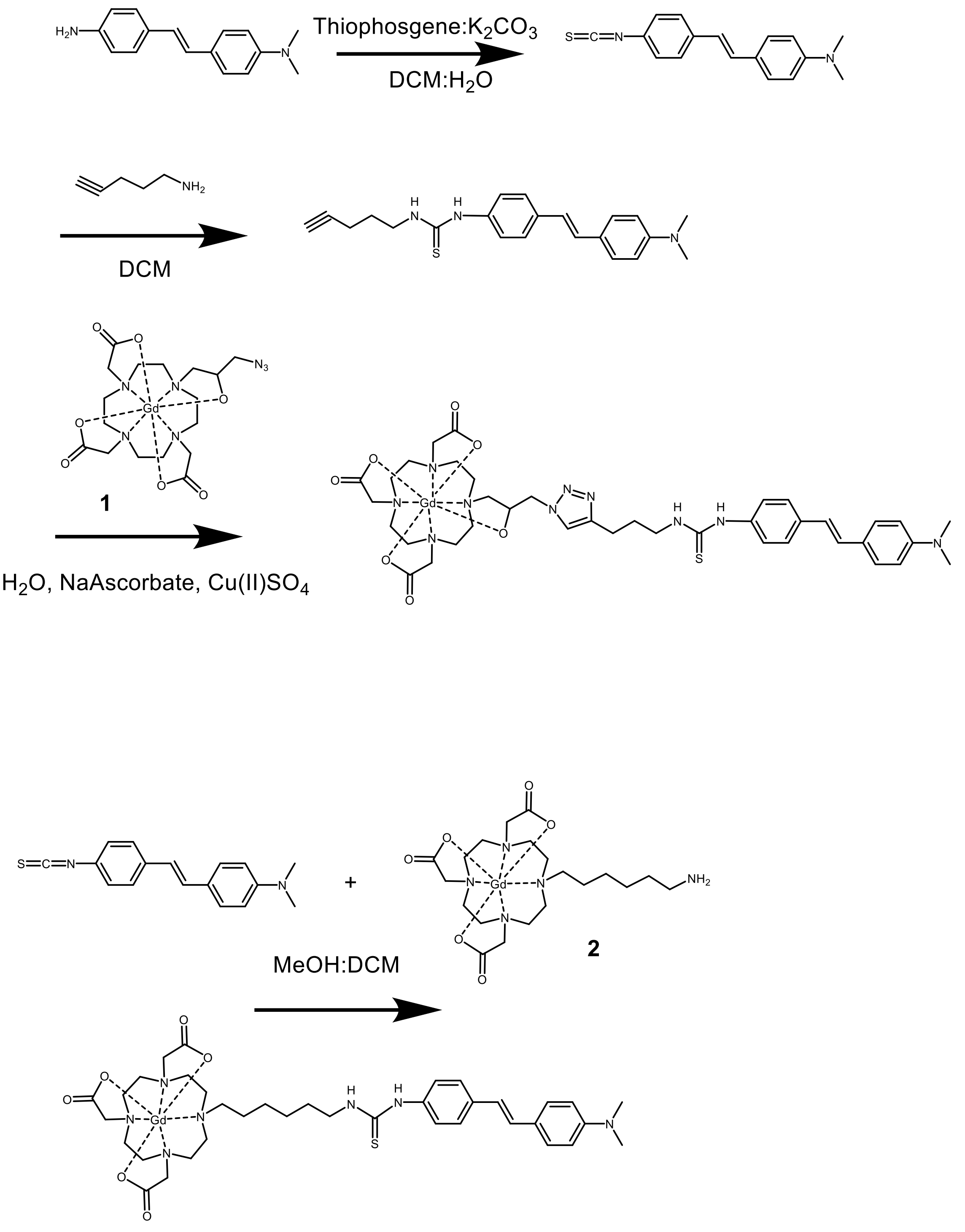

Figure 3.4 The synthetic both stilbene-targeted probes.

Briefly, stilbene-isocyothianate was coupled either directly to a Gd(III) chelate or functionalized with an alkyne that was used to couple to a Gd(III) chelate

Several chemical properties of the complexes were measured to ensure that they possessed the desired properties to detect amyloids. Relaxivity, hydrophilicity (in the form of octonal-water partition coefficient), and micelle size were all measured. Gd-Triazole-SB and Gd-Alkyl-SB displayed relaxivities of 16.3 $mm^{-1}s^{-1}$ and 15.2 $mm^{-1}s^{-1}$ respectively. Both of these values are far above what would be expected for a small molecule chelate. DOTA displays a relaxivity of 3.1 $mm^{-1}s^{-1}$ (6). This relaxivity boost is common for complexes that form macromolecules through aggregation or micelle formation. The longer rotational correlation time (τ_R) results in better magnetic coupling field strengths below 3 T. This interpretation is bolster by dynamic light scattering (DLS) data that indicates the formation of larger aggregates. Both agents displayed aggregate sizes in the hundreds of nanometers, however the precise value appeared to depend on the concentration of agent. Both agents were determined to be hydrophilic based on the octanol-water partition coefficient. As expected, Gd-Triazole-SB was more hydrophilic than Gd-Alkyl-SB, however both were water soluble. These data suggest that the aggregates measured by DLS are likely to be micelles. Finally, both agents were analyzed by nuclear magnetic resonance dispersion (NMRD) to explore the effect of field strength on relaxivity (Figure 3.5). The results are consistent with macromolecules of the size indicated by DLS.

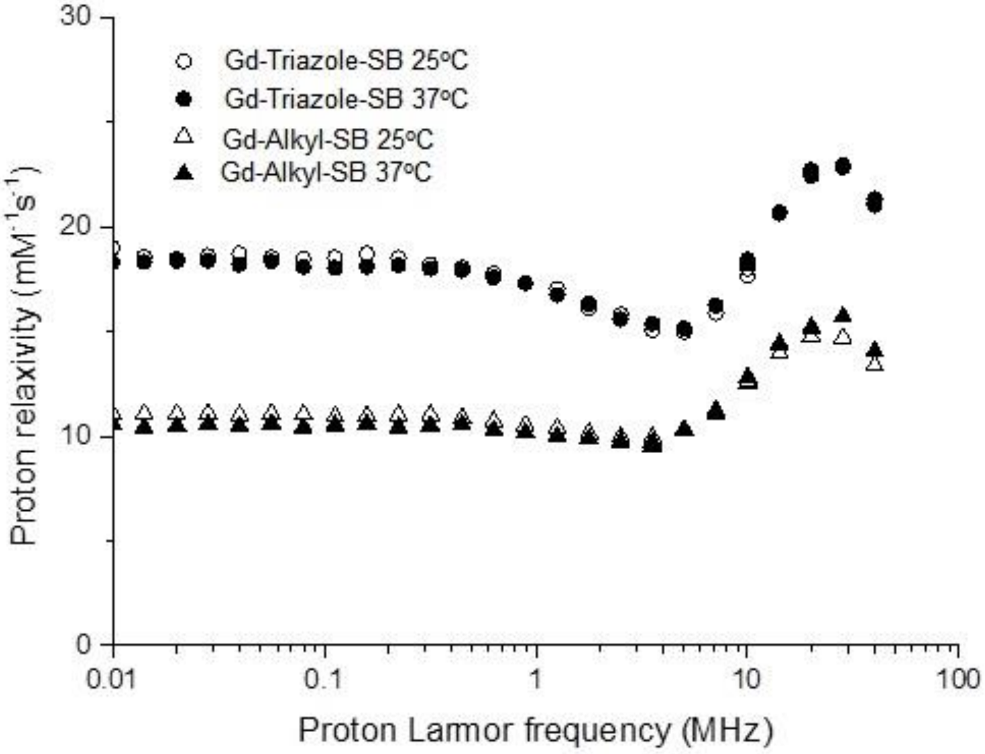

Figure 3.5 NRMD profile of both Gd-Triazole-SB and Gd-Alkyl-SB

Both agents were measured at 25˚C and 37 ˚C. The boost in relaxivity observed at 20 MHz is indicative of a slow tumbling rate, consistent with aggregation or micellar formation.

Functionalizing stilbene with a bulky-hydrophilic Gd(III) chelate could result in a loss of binding capacity to amyloids. This possibility was explored by directly measuring binding of Gd-Triazole-SB to insulin amyloids. Insulin is an intrinsically amyloidogenic protein that can be induced to aggregate with simple heating (92). Amyloid binding can be measured easily by taking advantage of the fluorescent properties of stilbene. When stilbene binds to amyloid it generates a large increase in the quantum yield, which led to the development of an Intrinsic Fluorescence Intensity (FLINT) assay (93). Importantly, there are two ways that a FLINT assay can be performed, either by adding increasing amounts of insulin fibril to a solution of stilbene (FLINT 1), or adding increasing amounts of stilbene to a solution of insulin fibrils (FLINT 2). These will yield different K_d values. This is because there is an unknown number of insulin monomers that are required to form a single stilbene binding site. Therefore, FLINT 1 should yield a higher K_d than FLINT 2, and the ratio of the two will indicate the number of insulin monomers that form a single stilbene binding site (93). Both FLINT 1 and FLINT 2 assays were performed for Gd-Triazole-SB (Figure 3.6). The measured binding constants were $K_{d1} = 11.4$ µM and $K_{d2} = 1.7$ µM. K_{d2} corresponds to the affinity of Gd-Triazole-SB for insulin fibrils, and is close to the affinity of other stilbene derivatives (94). These data indicate that Gd-Triazole-SB has maintained its amyloid binding ability and that there is one binding site for every 6.7 insulin monomers. It should be noted that the high background fluorescence in the FLINT 2 assay leads to a high error. This is an unavoidable consequence of using this assay. Unfortunately Gd-Alkyl-SB could not be used in these assays, as it required small amounts of dimethylsulfoxide (DMSO) to solubilize, and DMSO is known to disrupt amyloid aggregates (95).

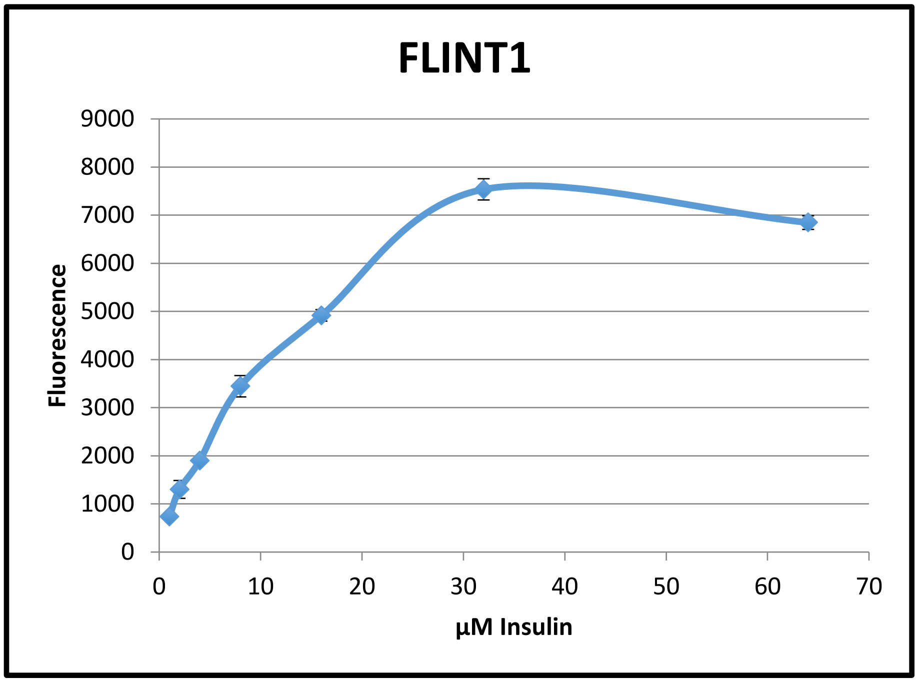

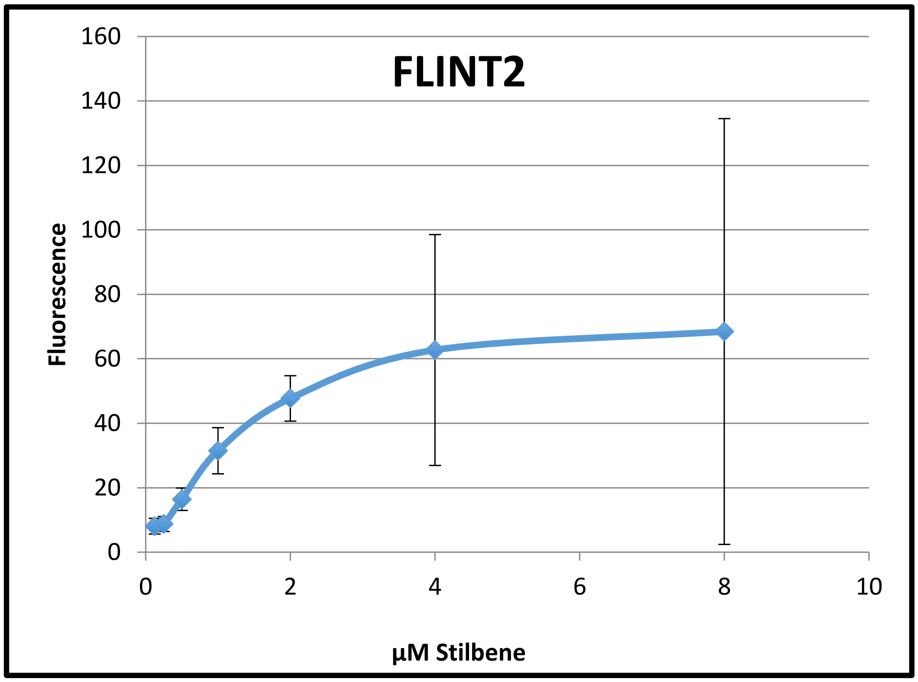

Figure 3.6 FLINT 1 and FLINT 2 assays indicating the binding of Gd-Triazole-SB to insulin amyloids. In FLINT1 insulin was added to a solution of Gd-Triazole-SB. In FLINT 2 Gd-Triazole-SB is added to a solution of insulin fibrils. These data were used to calculate the K_d in both cases. Error bars indicate standard deviation.

The primary motivation for synthesizing these agents was to act as amyloid imaging probes. However, they also possess many desirable properties sought in cell labeling agents. Many experiments suffer from an inability to track to the location of a specific set of cells in vivo. A variety of cell labeling agents exist to address this need. Iron oxide is particularly common, however as it produces negative contrast by MRI, there is a pressing need to create positive contrast cell labeling agents. A series of experiments was performed to evaluate the capacity of these agents to label cells. First, cell viability was measured for each agent in HT-22 mouse hippocampal cells (Figure 3.7). They both showed excellent cell viability up to 100 µM, with Gd-Triazole-SB showing no toxicity effects up to 1 mM. The cellular uptake of each agent was then measured against a panel of different cell lines (Figure 3.8). Gd-Triazole-SB showed superior uptake at all measured concentrations, in addition to having a higher range of viable concentrations. Interestingly, at all measured concentrations, B16 F0 cells showed higher uptake than other cell types. B16 cell are derived from mouse melanoma, and melanocytes are the only cells in this panel that contain amyloids (96). It was then verified that the measured cellular uptake could translate into contrast enhancement in cell pellet images (Figure 3.9). Additional contrast was observed at every incubation concentration. Bimodal detection is a particularly desirable property for a cell labeling agent. As stilbene is fluorescent, this bimodal capacity was verified using confocal microscopy (Figure 3.10). Indeed, intracellular aggregates of stilbene were clearly visible after incubation with the agent. Fluorescence can assist in validation of a cell labeling study.

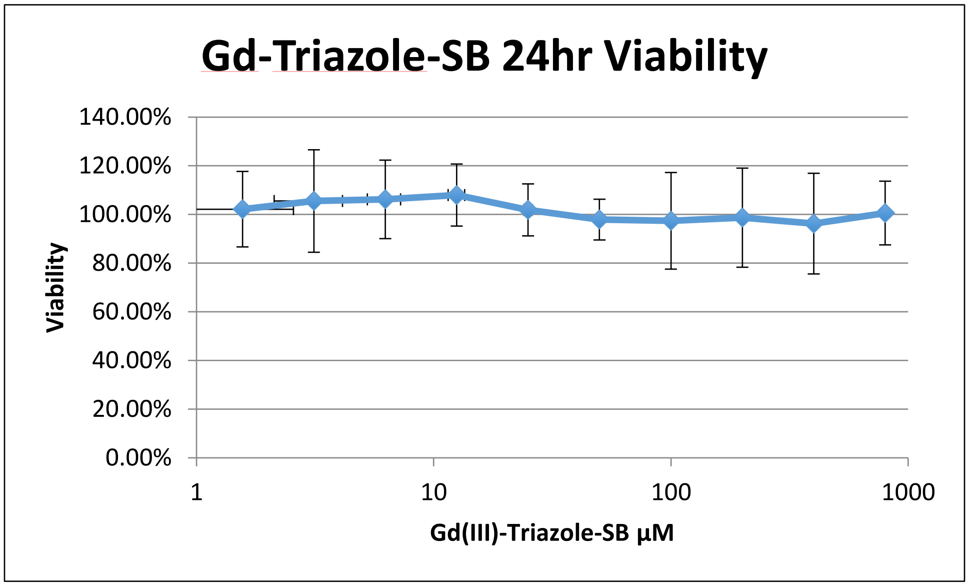

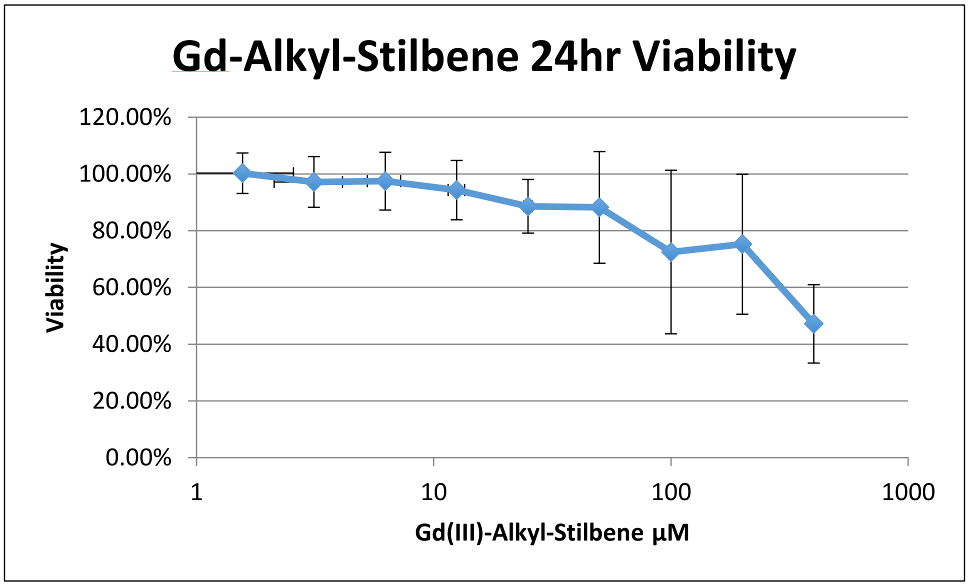

Figure 3.7 Viability of both agents in HT-22 cells

Viability was measured by MTS assay. Both agents display good biocompatibility up to several µM, with Gd-Triazole-SB being non-toxic. Error bars indicate standard deviation.

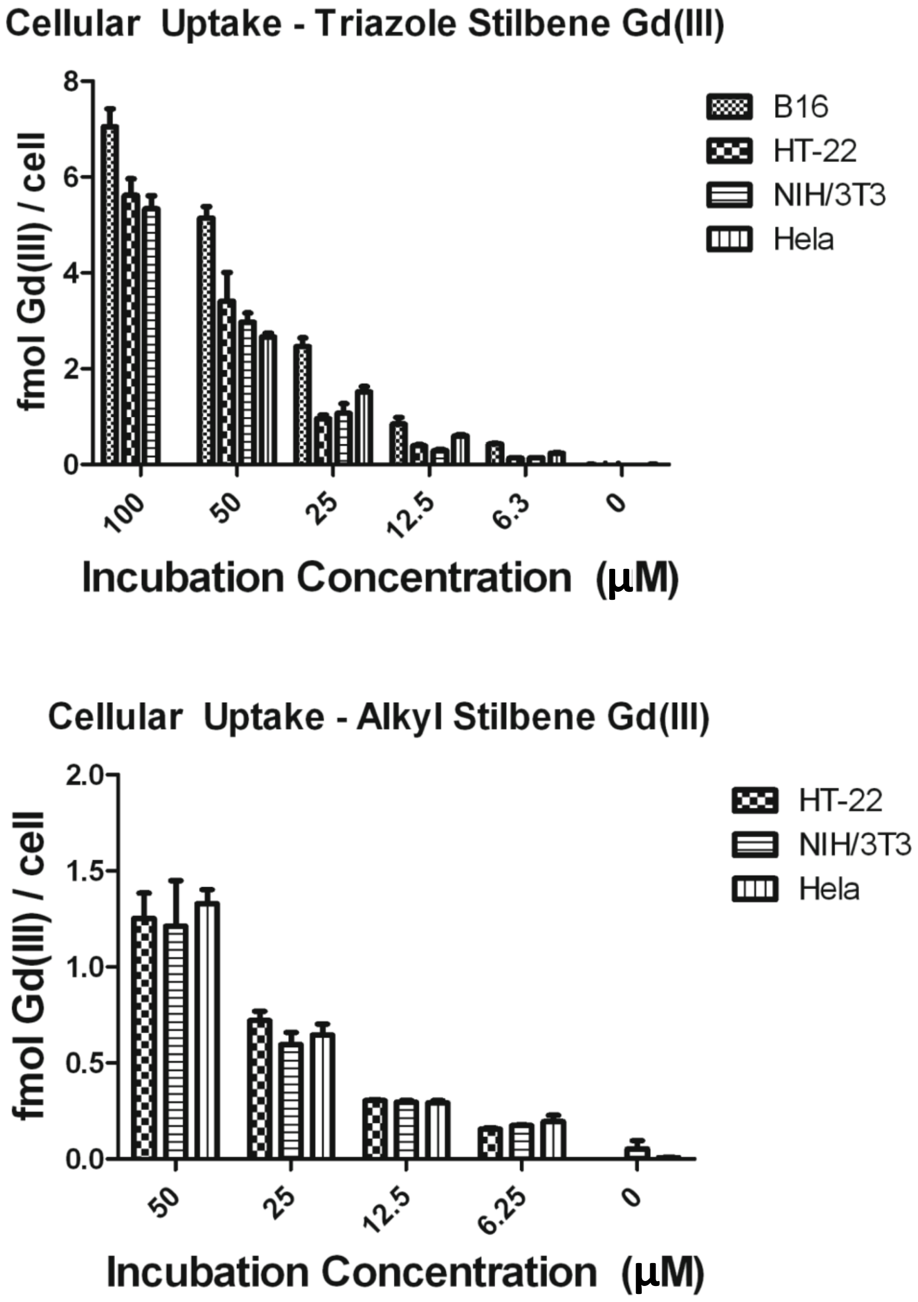

Cellular Uptake - Triazole Stilbene Gd(III)

Cellular Uptake - Alkyl Stilbene Gd(III)

Figure 3.8 The measured cellular uptake for both agents.

The cells were incubated at the indicated concentration for 24 h. Error bars indicate standard error of the mean.

Figure 3.9 Images of HT-22 cell pellets

Images were taken for both Gd-Alkyl-SB (a) and Gd-Triazole-SB (b). For each agent, clear contrast enhancement is apparent.

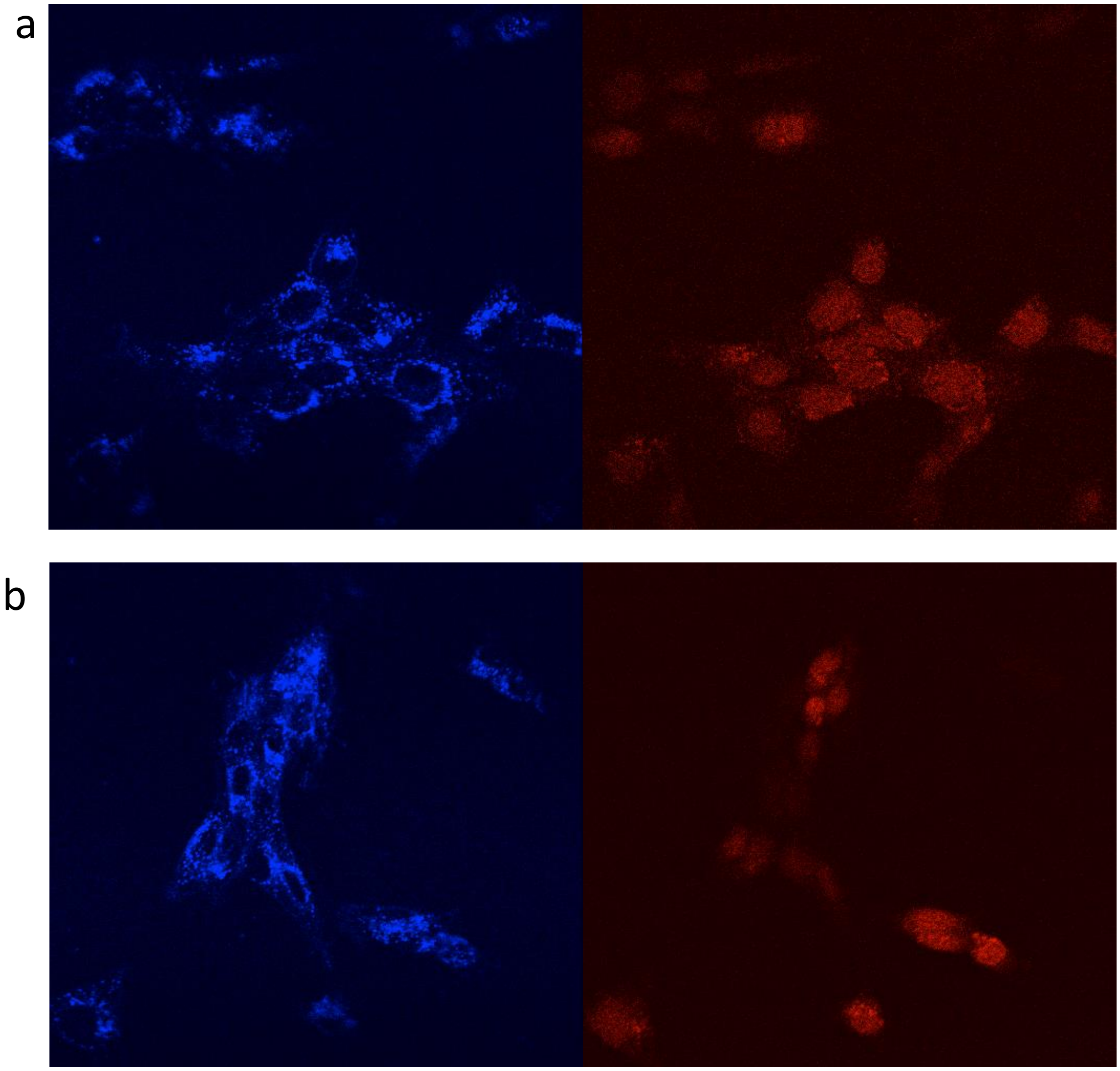

Figure 3.10 Confocal images of HT-22 cells

Cell were treated with either Gd-Triazole-SB (a) or Gd-Alkyl-SB (b). Stilbene fluorescence is indicated in blue. The red channel displays a nuclear stain.

While there are several in *vitro* tests that can be used to estimate the ability of an agent to cross the BBB, the most effective test is to measure it directly *in vivo*. A biodistribution study was preformed to determine how much of the agent can cross the BBB and which organs are responsible for clearance of the agent (Figure 3.11). Each agent was injected into six different mice, with groups of three being sacrificed at five minutes or one hour after tail vein injection. Organs were then harvest and the Gd(III) content measured by inductively-coupled plasma mass spectrometry (ICP-MS). The biodistribution pattern suggests clearance by both the renal and the reticuloendothelial systems. Both agents also displayed significant uptake in the lungs. Unfortunately, neither agent showed major uptake into the brain, and the measured values for brain uptake were tightly correlated with the measured value of Gd(III) in the blood, suggesting that the agent does not cross the BBB.

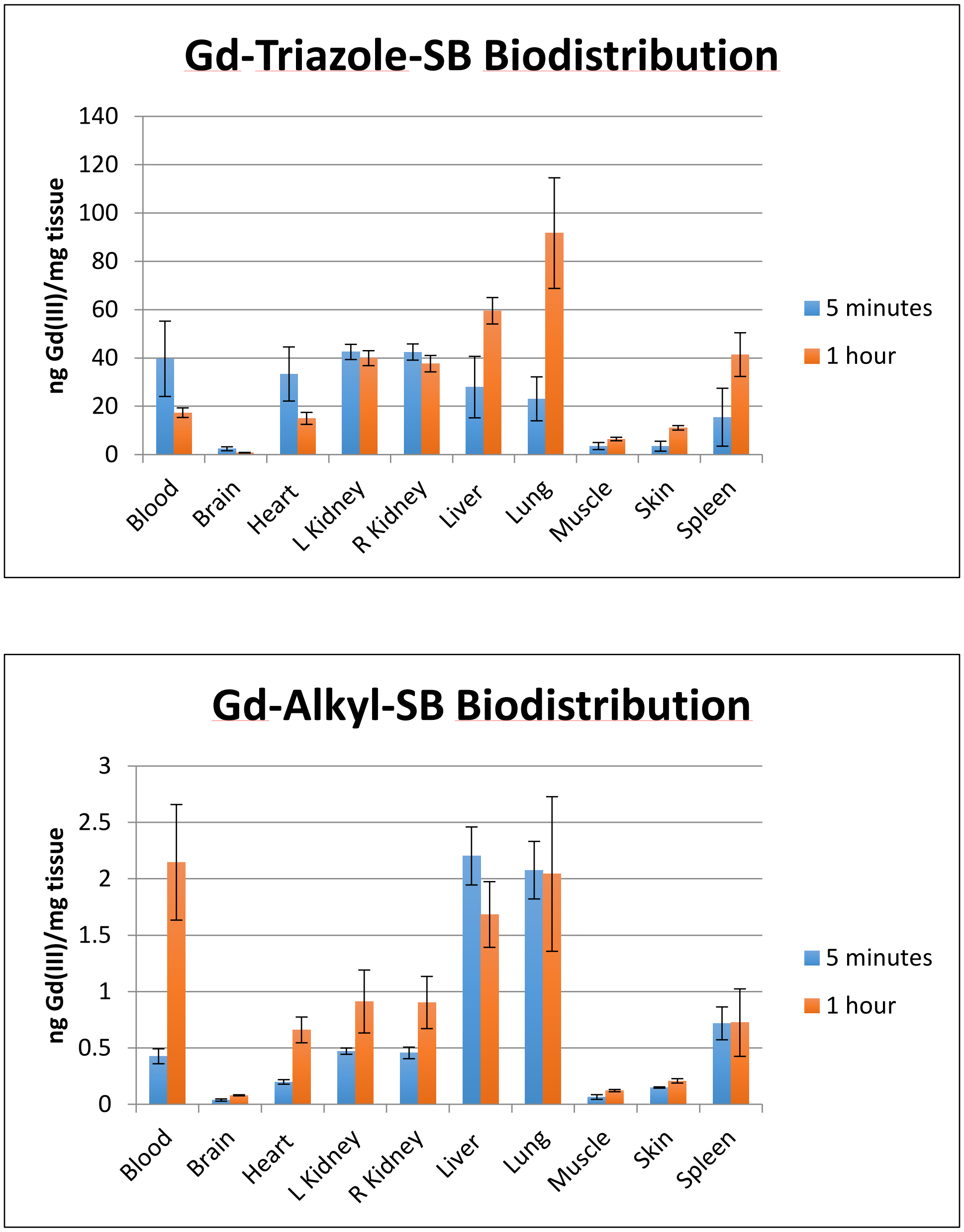

Figure 3.11 The results of a biodistribution study for both agents.

Both agents appear to display clearance through both the renal (kidneys) and reticuloendothelial (liver and spleen) systems. Neither agent shows appreciable accumulation in the brain. Error bars indicate standard deviation.

3.3 Conclusion and Future Directions

The biodistribution data strongly support the hypothesis that these agents are unable to cross the BBB. This result is somewhat surprising considering the literature precedent for similar agents being BBB permeable (22, 97). It should be noted that the BBB-crossing agents are all nuclear probes. Furthermore, none of their biodistribution studies describe methods of removing residual blood from the brain prior to measuring the presence of the probe. Considering that nuclear techniques do not have the spatial resolution to distinguish between blood vessels and brain plaques, and that the agents described here shown slow blood clearance, it is possible that previous reports did not adequately control for confounding variables. In addition, MR contrast agents would require significantly more uptake into the brain in order to cross the high detection limit of Gd(III). If one assumes a density of 1 g/ml tissue, then the peak concentration of less than 20 µM, very close to the minimum detectable amount (10 µM under ideal circumstances) and unlikely to be entirely past the BBB. These data call into question the utility of these agents for this goal.

Both agents displayed the capacity to serve as bimodal cell labeling agents. However, they do not appear to advance the field compared to recent breakthroughs in cell labeling technology. In 2015 the Meade lab reported an IR-783-Gd(III) bimodal cell labeling agent (98). This agent was able to achieve cellular uptake more than tenfold higher than the best stilbene agent. Furthermore, the IR-783 fluorophore excites and emits in the near infrared range (NIR) (Ex. 782 nm, Em. 800 nm). This region of the electromagnetic spectrum is preferable over the short wavelength fluorescence of stilbene (Ex. 350 nm, Em. 470 nm). The NIR is the region with the least absorption by biomolecules, and thus has the best penetrance for *in vivo* imaging. Stilbene fluorescence would be limited to histological sections.

3.4 Materials and Methods

3.4.1 Probe synthesis

Stilbene-isothiocyanate

Stilbene-NH_2 (1.00 g, 4.19 mmol) was added to a flask, dissolved in 50 ml DCM, and cooled to 0˚C. Separately, thiophosgene (0.48 g, 4.2 mmol) was dissolved in 30 ml DCM and K_2CO_3 (0.58 g, 4.2 mmol) was dissolved in 30 ml H_2O. The solutions of thiophosgene and K_2CO_3 were both added to the solution of Stilbene-NH_2 at the same time, and the mixture was allowed to stir for 5 h. It was then concentrated *in vacuo*, dissolved in DCM:H_2O, and extracted 3x into DCM. The organic layer was dried over Na_2SO_4. The product was purified by flash chromatography with a silica solid phase an 1:4 Hexanes:DCM mobile phase. It was then characterized by NMR.

Stilbene-Alkyne

To a flask was added stilbene-isothiocyanate (0.05 g, 0.18 mmol). 10 ml of dichloromethane (DCM) was added to flask and stirred to dissolve stilbene-isothiocyanate. To this flask was added 4-pentyne-1-amine (0.022 g, 0.26 mmol). The flask was allowed to stir for 18 hours. The resulting mixture was concentrated *in vacuo* yielding a yellow oil. This oil was purified by flash chromatography using a silica solid phase and 99.5:0.05 DCM:MeOH mobile phase. The resulting spot was characterized by NMR.

Gd-Triazole-SB

To a flask was added 10 ml dimethylformamide (DMF) and this was allowed to stir. To the solution was added stilbene-alkyne (0.01 g, 0.03 mmol), **1** (0.018mg, 0.03 mmol), $CuSO_4$ (1ml of a 10 mg/ml solution), and Sodium Ascorbate (0.01 mg, 0.05 mmol). **1** was synthesized using previously reported methods (82). This solution was allowed to stir for 62 hours at 45˚C. The resulting mixture was concentrated *in vacuo* yielding a yellow oil. The mixture was then dissolved in 1:1 MeCN:H_2O and purified by reverse phase HPLC using a C18 Atlantis column (Waters). The product was purified by HPLC.

Gd-Alkyl-SB

To a flask was added 10 ml of a 1:1 mixture of MeOH:DCM. **2** (0.05 g, 0.08 mmol) and stilbene-isothiocyanate (0.025 g, 0.09 mmol) were added to the stirring mixture. The solution was allowed to react for 72 hours at 40˚C. The reaction mixture was concentrated *in vacuo* to yield a yellow oil. The product was purified by dissolving the mixture in DCM, discarding the liquid portion and retaining the precipitant. This was then concentrated *in vacuo* to yield a solid yellow powder. This was then dissolved in H_2O, centrifuging at 21,000 g for 10 min, recovering the supernatant and discarding the pellet. This was once again concentrated *in vacuo*. Purity was verified by analytical HPLC and ESI-MS.

3.4.2 Chemical Characterization

Relaxivity

Relaxivity was calculated from serial dilutions of each agent. 1 mg of the agent was dissolved in 1 ml H_2O and serially diluted by halves ten times. The T_1 values were measured using a Minispec MQ60 Relaxometer (Bruker) for each solution. The T_1 value as determined by **METHOD**. As indicated by equation 1.3, the relaxivity can be determined as the slope of the line plotting contrast agent concentration and **RELAXATION TIME**. After relaxivity was measured, each sample was subjected to ICP analysis to verify the concentration of Gd(III).

Octanol-Water Partition Coefficient

For each contrast agent, 0.2 mg was dissolved in 1 ml of a 1:1 mixture of Octanol:H_2O in a 1.5 ml microcentrifuge tube. The solution was shaken for 30 s and allowed to gently rotate for 96 h to ensure equilibration. The solution was then allowed to settle for 24 h. A 10 µL was taken from each layer and analyzed by ICP-MS. The coefficient was calculated from Equation 3.1

Equation 3.1 $$\log P = \log(C_O/C_{H2o})$$

Dynamic Light Scattering

Aggregate size was determined by using a Malvern Instruments Zetasizer Nano Series-ZS. Samples were dissolved in water and measured in a polystyrene cuvette with a 10 mm optical window. The average size was calculated by Dispersion Technology Software. Four Gd-Triazole-SB solutions were made from 30 to 3.25 µM in water. Four Gd-Alkyl-SB solutions were made from 22 to 2.75 µM in water.

3.4.3 Cell Culture

HT-22 cells were cultured in DMEM (Life Technologies) supplemented with 10% FBS (VWR), 2 mM L-glutamine, 1 mM sodium pyruvate, and 0.02 mM non-essential amino acids. The MDA-231 cells were a gift from Dr. D. Welch. NIH-3T3 (ATCC) cells were cultured in DMEM supplemented with 10% FBS (VWR), 2 mM L-glutamine, 1 mM sodium pyruvate, and 0.02 mM non-essential amino acids. B16 F0 cells were cultured in DMEM supplemented with 10% FBS (VWR), 4 mM L-glutamine(Sigma), 1 mM sodium pyruvate, and 0.02 mM non-essential amino acids. HeLa (ATCC) cells were in MEM supplemented with 10% FBS (VWR), 2 mM L-glutamine, 1 mM sodium pyruvate, and 0.02 mM non-essential amino acids. All cells were maintained at 37°C in a 5% CO_2/95% humidified air atmosphere.

Gd-Alkyne-SB stock Solution Preparation

The limited solubility of Gd-Alkyl-SB required a specific procedure to produce a saturated stock solution. First, 0.8 mg Gd-Alkyl-SB was placed into a 1.5 ml microcentrifuge tube and dissolved in 80 µL DMSO. 1.92 ml Dulbecco's Phosphate Buffered Saline (DPBS) was placed into a separate 2 ml microcentrifuge tube. The 80 µL DMSO solution was carefully pipetted to the bottom of the DPBS solution, without allowing for mixing. The resulting solution was quickly vortexed at the highest speed for 1 min, and then sonicated for 45 min. The solution was then centrifuged at 21,000 g for 10 min at room temp. The supernatant was removed from the pellet and the Gd(III) content was measured using ICP-MS using a 10 µL sample.

Toxicity

Toxicity was measured using a MTS assay. HT-22 cells were plated at a density of 3,500 cells/well in a 96 well plate. After allowing cells to adhere overnight, the media from each well was removed and replaced with fresh media doped with the indicated concentration of contrast agent to a final volume of 100 µL per well. Each concentration was tested in triplicate. The cells were allowed to incubate for 24 h prior to measurement. To each well was added 20 µL MTS solution (Promega). The colorimetric assay was allowed to develop at 37°C for 30 minutes*.* The absorbance of each well was then measured at 550 nm. Each condition was compared to a control set treated with either media *(*Gd-Triazole-SB*)* or 4% DMSO in media *(*Gd-Alkyl-SB*).*

Cell Uptake

In order to perform cell uptake, each cell line was plated in 24 well plates at a density of 25,000 cells/well. After allowing them to adhere overnight, media was removed from each well and replaced with media doped with the indicated concentration of contrast agent, either in media alone (Gd-Triazole-SB) or 4% DMSO in media (Gd-Alkyl-SB) to a final volume of 300 µL. Each concentration was tested in triplicate. Cells were allowed to incubate for 24 h.

After the incubation cells were then rinsed in the plate once with DPBS, trypsinized with TypleE, treated with trypsin inhibitor, and collected into 1.5 ml microcentrifuge tubes. The cells were then pelleted at 1000g for 5 minutes at 4°C. Cell pellets were washed twice by resuspending in 400µL DPBS and pelleting.

Cells were counted using a Guava EasyCyte Mini Personal Cell Analyzer (EMD Millipore). After cell resuspension, an aliquot (50 µL) of the suspension was diluted in Guava ViaCount reagent (150 µL). Stained samples were vortexed for 10 s and then cells were counted using a Guava EasyCyte Mini Personal Cell Analyzer (PCA) using the ViaCount software module***.***

Quantification of gadolinium for cell uptake experiments was accomplished using ICP-MS of acid digested samples. Specifically, aqueous samples were digested in concentrated nitric acid (> 69%, Sigma) and hydrochloric acid (37% BDH) and heated to 75 °C for overnight. Samples were then diluted with ultra-pure H_2O (18.2 MΩ·cm) and multi-element internal standard (CLISS-1, Spex Certiprep) to 3.0% nitric acid (v/v) and 5.0 ng/mL internal standard in a total sample volume of 3 mL. Individual Gd elemental standards were prepared at 0.78125, 1.5625, 3.125, 6.25, 12.5, 25.0, 50.0, 100, and 200 ng/mL concentrations with 3.0% nitric acid (v/v) and 5.0 ng/mL internal standards up to a total sample volume of 10 mL.

Confocal Microscopy

HT-22 cells were plated onto 35mm circular cell culture dishes (World Precision Instruments) at a density of 20,000 cells/dish. The cells were allowed to adhere for 24 hours. The media was removed and replaced with media including either 50 µM Gd-Alkyl-SB or 50µM Gd-Triazole-SB. Cells were left to incubate with the agents for another 24 hours. The media in the dishes was removed and replaced with fresh media. Prior to imaging, each dish was treated with one drop of NucRed (Themo Fisher Scientific) to serve as a nuclear stain.

Cells were imaged with a Zeiss 510 Inverted Confocal Microscope. In order to ensure cell viability, cells were imaged with the assistance of a temperature and CO_2 controlled cell culture chamber (Zeiss).

Cell Pellet Images

T75 flasks were used to plate 300,000 HT-22 cells. After allowing them to adhere overnight, each flask had media removed and replaced with media doped with the indicated concentration of contrast agent, either in media alone (Gd-Triazole-SB) or 4% DMSO in media (Gd-Alkyl-SB). After a 24 h incubation the media was removed and the cell were dissociated with trypsin. The trypsin was inhibited with 0.5 ml fresh media and cells were collected into 1.5 ml microcentrifuge tubes. Cells were then centrifuged at 1000 g for 5 min at room temperature and resuspended in 500 µL DPBS. This was step was repeated two more times to remove residual contrast agent.

Flame-sealed pipettes were prepared to serve as MR compatible vessels. Nine inch Pasteur pipettes were flame sealed and the cells were transferred into them. The pipettes were then cut to enable centrifuging at 100 g for 5 m at room temperature. Finally, the pipettes were cut again to yield a two inch glass tube containing the cells. These were finally sealed with Parafilm and imaged by MR.

In order to determine Spin-lattice relaxation times (T_1), a rapid-acquisition rapid-echo (RARE-VTC) T_1-map plus sequence with static TE (11 ms) and variable TR (150, 250, 500, 750, 1000, 2000, 4000, 6000, 8000, and 10000 ms) values was used. The imaging parameters were: field of view (FOV) = 25×25 mm^2, matrix size (MTX) = 256×256, number of axial slices = 4, slice thickness (SI) = 1.0 mm, and averages (NEX) = 3 (total scan time = 2 h 36 min). T_1 analysis was carried out using the image sequence analysis tool in Paravision 5.0 pl3 software (Bruker, Billerica, MA, USA) with monoexponential curve-fitting of image intensities of regions of interest (ROIs) for each axial slice.

3.4.4 Amyloid Binding Assays

Insulin amyloid fibrils were created from a solution of soluble insulin. A 10 mg/ml solution of human insulin (Sigma) was diluted to 0.5 mg/ml with phosphate buffer (100mM pH 7.4). This solution was then heated to 57˚C and allowed to stir overnight.

The presence of insulin amyloids was verified by using a Thioflavin T (THT) assay. THT absorbs at 450 nm and emits weakly at 482 nm. However, when bound to amyloid fibrils, THT becomes brightly fluorescent. THT (Sigma) was dissolved in H_2O to a concentration of 20 µM. The fluorescence of this solution before and after the addition of insulin fibrils. Fibrils were indicated by a fluorescence increase at 250 nM insulin.

FLINT 1 assays were performed by creating 100 µL solutions of 5 µM Gd-Triazole-SB and the indicated concentration of insulin in a 96 well plate, each in triplicate. Fluorescence was compared to matched concentrations of Gd-Triazole-SB and non-fibrilized insulin. The fluorescence of each well was measured by a plate reader (Gemini EM Fluorescence/Chemiluminescence Plate Reader) with excitation of 350 nm and emission at 470 nm. FLINT 2 assays were performed using the same procedure but maintaining an insulin concentration of 250 nM and varying the Gd-Triazole-SB concentration. In both cases, the K_d value was calculated using GraphPad (Prism).

3.4.5 Biodistribution

Two saturated solutions of both Gd-Alkyl-SB and Gd-Triazole-SB solutions were made. 19 mg of each agent was dissolved in 1.5 ml DPBS with 2% Tween-20. Solutions were vortexed, sonicated, and finally centrifuged at 21,000 g for 10m at room temperature. The supernatant was collected and the pellet discarded. This procedure was repeated a total of three times. Finally, the solutions were passed through a 0.2 µm filter.

Samples were taken from each solution to determine the concentration of agent by ICP. Each ICP sample was made by first digesting 10 µL saturated solution in 200 µL concentrated nitric acid (> 69%, Sigma). This solution was heated to 70˚C for 12 hours. Samples were then diluted with ultra-pure H_2O (18.2 MΩ·cm) and multi-element internal standard (CLISS-1, Spex Certiprep) to 2.0% nitric acid (v/v) and 5.0

ng/mL internal standard in a total sample volume of 10 mL. Individual Gd elemental standards were prepared at 0.78125, 1.5625, 3.125, 6.25, 12.5, 25.0, 50.0, 100, and 200 ng/mL concentrations with 3.0% nitric acid (v/v) and 5.0 ng/mL internal standards up to a total sample volume of 10 mL.

Mice were divided into four groups. Six mice were assigned to receive each agent, with measurements taken at two different time points (5 m and 1 hr) in triplicate. Each mouse received a 200 µL tail vein injection. At the appointed time, mice were sacrificed and their organs harvested. The organs were immediately weighed and placed into 1.5 ml microcentrifuge tubes and stored at -80 ˚C.

Each mouse organ was prepared for analysis by ICP. Organs were allowed to thaw for 10 min and distributed into weighed microwave tubes. Any organ larger than 0.4 g was cut to fit. Concentrated nitric acid was added at 2 µL/mg tissue. Tubes were then microwaved at 800 W for until the organs were digested. Digest organs were distributed into 2 ml tubes. A sample of each was placed into a weighed 15ml conical tube along with internal standard and H_2O to 5ml. These samples were then subjected to Gd(III) analysis by ICP.

Chapter Four

Multimodal quantification of micrometastases in the brain after intracardiac injection of labeled cells

4.1 Introduction

Between 100,000 and 170,000 people per year in the United States are estimated to have metastatic brain tumors. Melanoma, lung, colon, kidney and breast cancers all have a high propensity to metastasize to the brain. The improved treatment of primary cancers has allowed patients to survive longer with the disease. This prolonged survival, which maintains the disease in a chronic condition, is hypothesized to allow time for brain metastases to grow. Breast cancer patients with brain metastases often manifest within 5 years of diagnosis of the primary tumor. These patients typically survive for only 2-16 months after diagnosis of the brain metastases (99-101). Understanding mechanisms of breast cancer metastasis to the brain is of critical importance for improvements in clinical treatment of the disease. After years of research, still little is known about how breast cancer cells arrive to the brain and grow within the microenvironment of the brain. The objective of this research is to quantify the arrival of breast cancer cells in the brain after injection into the left ventricle of the mouse heart.

The study of brain metastases present several technical challenges (102). The complex nature of cancer metastasis makes it difficult to obtain informative studies without taking an *in vivo* approach (102). Therefore, appropriate imaging experiments become essential to metastasis research. However, no single modality is able to provide tomographic in vivo imaging with single cell resolution. MR imaging has the highest spatial resolution of any *in vivo* imaging modality with unlimited depth of penetration, however it cannot attain cellular resolution. Fluorescence can achieve the resolution required to visualize individual cells, but only for select tissue slices *ex vivo*. Bioluminescence is highly sensitive and allows for rapid screening, but light scattering *in vivo* limits the spatial resolution for deep tissue imaging (8).

Here, we present a procedure to leverage the advantages of each imaging modality while minimizing their weaknesses. This was achieved by using bioluminescence to rapidly screen mice for successful injection, MR imaging of labeled cells to quantify metastases in the brain, and fluorescence and histology to verify that the observed MR signal was produced by labeled cells.

Tracking cells by MR imaging requires an appropriate cell labeling agent (98, 103, 104). Superparamagnetic iron oxide nanoparticles (SPION) and micron-sized superparamagnetic iron oxide particles (MPIO) are commonly used MRI contrast agents to track labeled cells *in vivo (105, 106).* These particles create local magnetic inhomogeneities that shorten the transverse relaxation time (T_2) of nearby protons, thereby creating negative contrast in MR images (107). Cells labeled with SPIONs or MPIO's produce hypointense voxels in MR images. Due to the "blooming artifact," iron oxide can produce hypointense voxels much larger than the size of the labeled cells (108). This is an advantageous property because single cells can be detected even though the spatial resolution of MR imaging cannot reach the single cell level (109, 110). However, in order to image single cells a very high dose of iron must be internalized into the cell (109). Because some cell types have shown subtle differences in motility and differentiation after labeling with iron particles, there is growing interest in using high-relaxivity particles that can be detected at lower concentrations (111, 112).

Attaining single cell detection with lower levels of iron agents requires the development of high-relaxivity SPIONs. The relaxivity and cellular uptake of iron oxide nanoparticles increases with the size of the particle (113, 114). However, iron oxide particles larger than 30nm have reduced relaxivity, which diminishes their effectiveness as contrast agents (113). We have addressed this limitation by using controlled aggregation to bring together small nanoparticles into larger clusters. These "nanoflowers" display high relaxivity (238 $mM^{-1}s^{-1}$) and are biocompatible at concentrations as high as 60 mg/L Fe (113). Furthermore, they are colloidally stable across a wide range of ionic strength and pH (113). Therefore, we chose to use our nanoflower contrast agent to detect the human breast cancer cells as they cross into the brain and grow.

In order to validate the MR imaging results, the cells injected into the heart express both mCherry fluorescent protein and luciferase. The bioluminescence produced by luciferase was used to screen for successful cell delivery to the brain after injection, as well as confirming the continued presence of live cells in the brain several days later. mCherry fluorescence enabled co-registration of injected cells with iron detected by Prussian blue staining in histological sections. Cell tracking with highly sensitive iron oxide nanoflowers offers a promising approach to the study of factors controlling brain cancer metastasis.

4.2 Results and Discussion

The MDA-231 human breast cancer cells were transfected with a retroviral vector carrying mCherry fluorescent and luciferase reporter genes. These cells were labeled with iron oxide nanoflowers. These nanoflowers had an average size of 162 nm as measured by dynamic light scattering, and an average r_2 of 207$s^{-1}mM^{-1}$. MDA-231 cell viability was unaffected by a 24h incubation with a nanoflower solution containing iron concentrations up to 60 mg/L Fe. Nanoflower uptake increased approximately linearly with iron concentration to 546.5±53 fmol/cell Fe at an incubation concentration of 60 mg/L Fe (Figure 4.1).

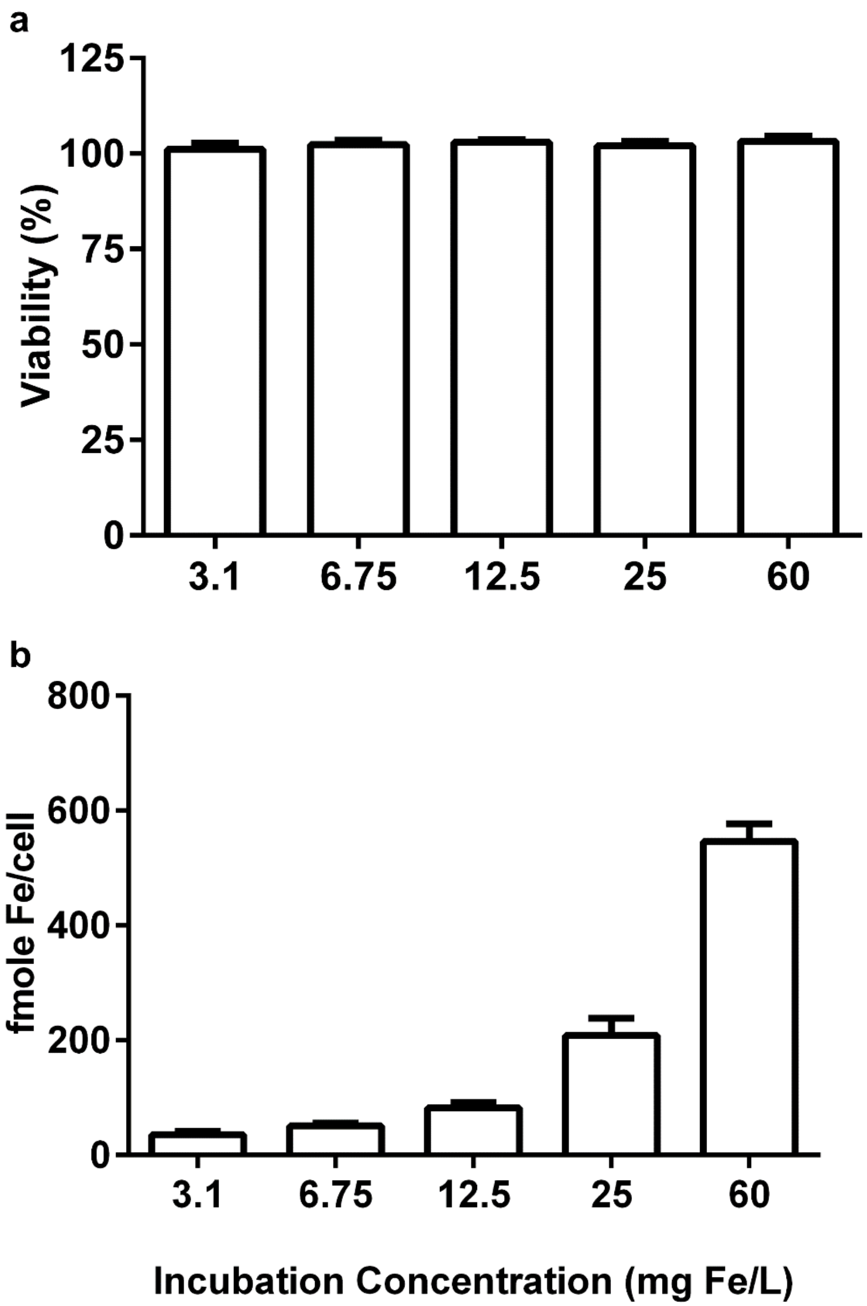

Figure 4.1 Nanoflowers display biocompatibility and high cellular uptake.

a) Viability remains high up to 60 mg Fe/L. b) Cellular uptake of Fe increases linearly with incubation concentration. Error bars indicate standard error of the mean.

Bioluminescence imaging allows for screening of the mice to prevent inclusion of animals where cells were not injected completely into the left ventricle (Figure 4.2). Of 12 mice injected with Fe_3O_4 nanoflowers labeled MDA-231 cells, 3 showed significant bioluminescent signal in the lungs, indicating failed intracardiac injection (Figure 4.2). Of the remaining 9 mice, 6 were selected to proceed to the MR imaging study based on IVIS signal in the brain and signal detected in the spine or long bones (Figure 4.2). Mice were re-screened with the IVIS 7 days post cell injection to confirm metastasis formation, and all 6 mice had live tumor cells in the brain and bone at that time (Figure 4.2).

Mice with successful intracardiac injections were imaged by MR. Labeled tumor cells were visualized as signal voids on the MR images and were distributed throughout the brain (Figure 4.3). Amira 5.4 software was used for analysis of the images. The repetitions were averaged, resliced to an axial orientation, and then skull-stripped (Figure 4.3). To avoid double-counting metastases that appear on multiple slices, metastases were segmented on all slices and a connected component analysis was applied (Figure 4.2). Metastases were rendered in 3D and overlaid on a time-of-flight MR angiogram to aid visualization (Figure 4.3). An average of 37±25 metastases were detected across the study group (Figure 4.3).

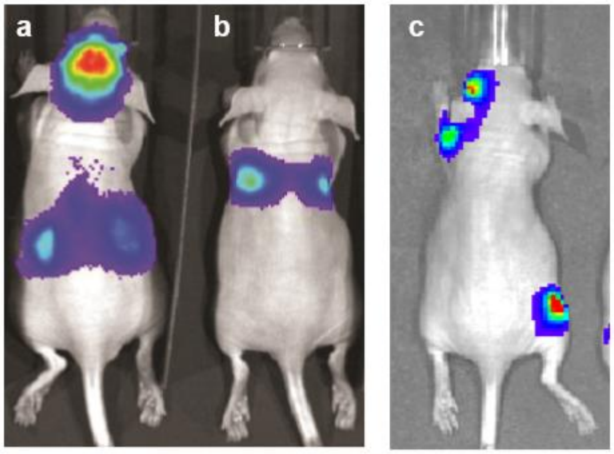

Figure 4.2 Bioluminescence imaging allows for screening of the mice

Forty-five minutes after injection of the MDA-231 cells into the left ventricle of the mouse heart, bioluminescence imaging was performed. a) An example of a mouse that was accepted for MRI analysis based on strong single in the brain and signal in the spine. b) An example of a mouse that was excluded for MRI analysis based on all the signal being detected in the lung. c) Bioluminescent signal in the brain and bone of a mouse 7 days after injection of the tumor cells.

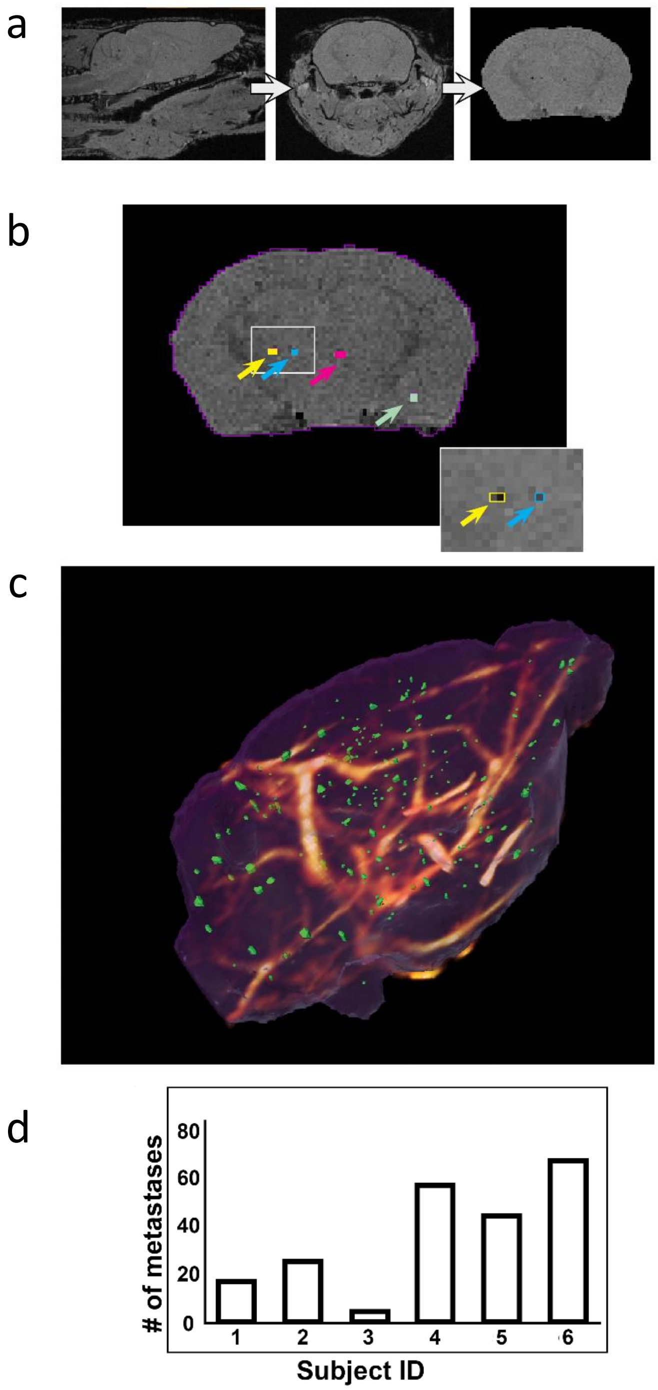

Figure 4.3 Metastases were detected by MRI.

Analysis was performed in Amira 5.4. a) Repetitions were averaged, resliced to an axial orientation, and the skull-stripped. b) Metastases were segmented, and a connected component analysis applied to avoid double-counting metastases appearing on multiple slices. c) Metastases were rendered in 3D and overlaid on a time-of-flight MR angiogram to aid visualization. d) The total number of metastases was counted for each animal with an average of 37 ± 25.

To confirm that signal voids were the MDA-231 breast cancer cells, the brains were frozen and Prussian Blue was used to detect Fe-labeled tumor cells. Single MDA-231 breast cancer cells were detected near blood vessels throughout the brain (Figure 4.4). Additionally in serial sections the tumor cells could be detected by mCherry fluorescent protein (Figure 4.4).

It has been previously shown that single cells can be detected by MR imaging in mouse brains 5 h post-injection of MDA-231 breast cancer cells into the left ventricle of the mouse heart (109). Heyn et al. found that approximately 3% of cells injected into the mice arrested in the brain on day 0 and by day 3, 81% of these cells were no longer detectable; however, some cells grew and formed tumors which were detected by MR imaging at day 28(109). In a complementary study, Lorger et al.(115) showed by immunofluorescent staining that breast cancer cells arrive to the brain within 15-20 minutes after intracardiac injection, survive in blood vessels in the brain for up to 3 days, and are localized as single cells outside and around blood vessels 5 to 7 days after injections. Based on these time points we sought to examine arrival of MDA-231 breast cancer cells in the brain 7 days after injection of breast cancer cells into the left ventricle of the mouse heart using the superparamagnetic iron oxide nanoflower probe.

Brain metastases labeled with iron oxide nanoflowers were readily detected in all animals. Cell tracking with these highly sensitive nanoflowers offers a promising approach to the study of factors controlling brain metastasis. The use a nanoflower probe allows detection of cells as they cross into the brain and proliferate. While it is difficult to conclusively determine that hypointense voxels observed by MR imaging are produced by single cells, histology showed that cells were primarily solitary. The high relaxivity of nanoflowers enables detection with lower levels of Fe than would be required using MPIOs or SPIONs and thus should reduce the effect of the Fe on cell viability, migration, and invasion.

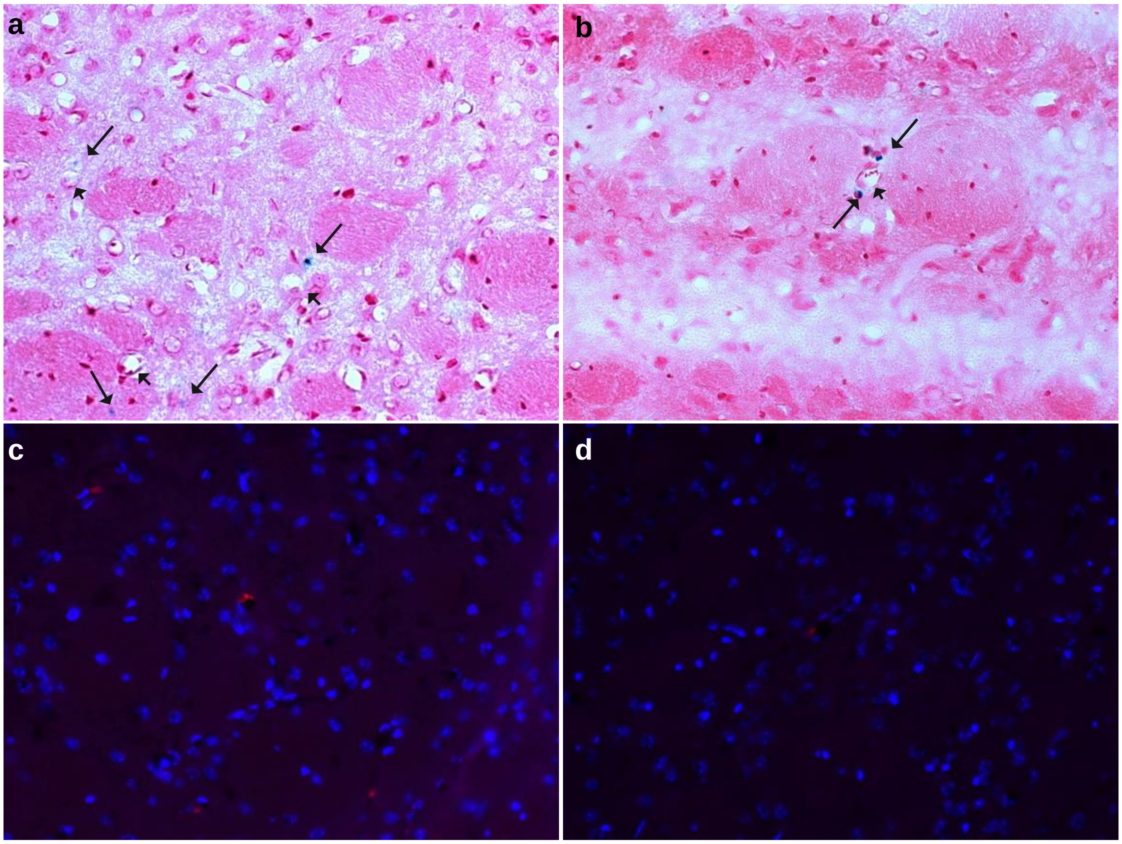

Figure 4.4 Histological validation of experimental metastases.

Prussian blue staining (a and b) for iron labeled MDA-231 breast cancer cells detects single cells (arrow) near blood vessels (arrowheads). Confirmation of that the Prussian blue is staining tumor cells is seen by detection of mCherry fluorescent (arrows) that was retained in the MDA-231 breast cancer cells in the frozen sections (c and d). Blue, DAPI staining for detection of nuclei of the brain section.

In previous studies, investigators have segmented signal voids on a widely spaced subset of image slices to avoid double-counting metastases that may appear on two consecutive slices (116). In this study, significant heterogeneity was observed in the spatial distribution of signal voids; therefore voids were segmented in all image slices. To avoid over counting metastases appearing in multiple slices, a connected component analysis was applied to obtain a final count. Connected component analyses have been used in applications such as cell counting in microscopy data, but have not been previously applied to metastasis detection in MRI (117). In this study, the connected component analysis had the additional benefit of reducing the accidental inclusion of blood vessels in the metastasis count, as it would reveal blood vessels as a coherent structure spanning several slices.

4.3 Conclusion and Future Directions

This study highlights the advantages of multiple imaging modalities for cross validation. Using bioluminescence imaging for rapid high-throughput screening of animals allows study inclusion of only animals with successful cell delivery to the brain, and can indicate that living cells are still present at 7 days. MR imaging allows accurate quantification of the number of brain metastases. Fluorescence ensures that the iron detected by MR imaging is co-localized with the cells of interest and confirm that the cells are alive. Thus, combining multiple imaging approaches improves the quality of the data and provides a sensitive way to detect single cell breast cancer cells as they cross into the brain microenvironment. This platform will support a variety of future studies on the effects of cancer cell gene expression, mouse knockout models, and new therapies on metastatic growth in the brain.

4.4 Materials and Methods

4.4.1 Cell Culture

The human breast carcinoma cell line MDA-231 was grown in DMEM/F-12 supplemented with 5% FBS (Gemini), 2 mM L-glutamine, 1 mM sodium pyruvate, 0.02 mM non-essential amino acids, puromycin (1 mg/ml) (EMD Millipore), and fungizone (2.5 ml/ml) (Sigma). The MDA-231 cells were a gift from Dr. D. Welch (University of Kansas Medical Center, Kansas City, KS). These cells were transduced with a pBABE retroviral vector containing the mCherry fluorescent as well as luciferase genes (a kind gift from Drs. Brandon Parker and Debabrata Chakravarti, Northwestern University School of Medicine, Chicago, IL). The cells having the top 2% of mCherry expression were sorted by flow cytometry. All cells were maintained at 37°C in a 5% CO_2/95% humidified air atmosphere.

Cell Uptake

MDA-231 cells were incubated at the indicated concentration of nanoflowers in media for 24 hours. The labeling media was removed, cells were trypsinized until suspended, and the trypsin was inhibited with Trypsin Inhibitor. The resulting cell suspensions were collected into microcentrifuge tubes and the cells were washed by centrifuging at 1,000x g for 5 min at 4˚C, removing the supernatant and resuspending the cell pellet in 500 μl Dulbecco's Phosphate Buffered Saline (DPBS). This wash step was performed three times. After the final wash the cells were resuspended in 200 μl DPBS. The suspended cells were separated for ICP-MS and Guava analysis.

ICP-MS

Quantification of ^{57}Fe was accomplished by ICP-MS of 135 μl samples of the suspended, washed cells after acid digestion. Aqueous samples were digested in concentrated trace nitric acid (>69%, Sigma) and heated to 75 °C for at least 4 hours to fully digest the sample. Ultra pure H_2O (18.2 MΩ·cm) and multi-element internal standard containing Bi, Ho, In, Li(6), Sc, Tb, and Y (CLISS-1, Spex Certiprep) were added to produce a final solution of 3.0% nitric acid (v/v) and 5.0 ng/mL internal standard in a total sample volume of 3 mL. Individual iron elemental standards were prepared at 0.78125, 1.5625, 3.125, 6.25, 12.5, 25.0, 50.0, 100, and 200 ng/mL concentrations with 3.0% nitric acid (v/v) and 5.0 ng/mL internal standards up to a total sample volume of 10 mL.

ICP-MS was performed on a computer-controlled (Plasmalab software) Thermo X series II ICP-MS (Thermo Fisher Scientific) operating in standard mode equipped with a CETAC 260 autosampler (Omaha). Each sample was acquired using 1 survey run (10 sweeps) and 3 main (peak jumping) runs (100 sweeps). The isotopes selected for analysis were ^{57}Fe, and ^{115}In and ^{165}Ho (chosen as internal standards for data interpolation and machine stability). Instrument performance is optimized daily through autotuning followed by verification via a performance report (passing manufacturer specifications).

Cell Counting and Viability

A Guava EasyCyte Mini Personal Cell Analyzer (EMD Millipore) was used for cell counting and viability. A 50 µL aliquot of the cell suspensions was diluted in 150 µL Guava Viacount reagent and allowed to incubate at room temperature for 5 min. Stained samples were counted using a Guava EasyCyte Mini Personal Cell Analyzer (PCA) using the ViaCount software module. 100 Event were acquired for each sample with dilution factors chosen to optimize machine performance (20-70 cells/µL).

4.4.2 Animal Model

All studies were approved by Northwestern University Institutional Animal Care and Use committee. Mice were maintained in approved pathogen-free housing facilities. MDA-231 breast cancer cells expressing mCherry-luciferase were collected with Versene (Life Technologies, Frederick, MD). The cells were incubated for 24 hr in serum media with 50 mg Fe/L of Fe_3O_4 nanoflowers. These labeled MDA-231 cells were then collected with Versene and were injected (2×10^5 cells/mouse in 200 μl of PBS) using 26-gauge needles into the left cardiac ventricle of 4-week-old athymic female nude mice (n=12; Harlan Laboratories). The mice were anesthetized for the intracardiac injection and imaging procedures using isoflurane inhalation (1-2% isoflurane, 1 L/min O_2). Body temperature was maintained throughout the experiments using heating pads or a heated platform.

Bioluminescence imaging

Within 45 min after injection of the labeled breast cancer cells, bioluminescence imaging was performed on mice using an IVIS Spectrum (PerkinElmer) to determine if the intracardiac injection was successful. Mice were administered 150 mg/kg D-luciferin Firefly (Gold biotechnology) intraperitoneally and bioluminescence was recorded 12 min later. Mice that had bioluminescence detected in the lung (indicating a failed injection) were excluded from further analysis. Six mice with bioluminescence detected in the brain and bones 45 min after intracardiac injection were selected for further analysis. The mice were reinjected with D-luciferin and imaging was repeated in the same way 3 and 7 days after injection to confirm the presence of live tumor cells in the brain.

Magnetic resonance imaging

Magnetic resonance imaging was performed 7 days post injection of tumor cells, after confirming the presence of tumor cells in the brain using bioluminescence as described. Images were acquired using a 7 T Bruker PharmaScan MRI system (Bruker Biospin) and a 23 mm quadrature fixed-tune volume coil optimized for mouse brain imaging. Mice were placed in an induction chamber and anesthetized using 3% isoflurane delivered in 100% oxygen. Anesthesia was maintained at 1-1.5% using a nosecone integrated into a dedicated animal bed. Respiration and temperature were monitored using an MR compatible SA Instruments small animal monitoring system (Small Animal Instruments); physiologic temperature was maintained using a warm water circulating system. Respiratory gated 3D gradient echo (FLASH) images were acquired with TR/TE/α = 20 ms/6 ms/7°, field of view = 20 mm x 15 mm x 17.5 mm, and matrix = 167 x 125 x 146 for an isotropic resolution of 0.120 mm. Scan times were approximately 13 minutes depending on gating efficiency. Three scan repetitions were acquired and averaged offline to increase signal to noise ratio. The repetitions were acquired separately so that respiratory gating issues during one scan would not affect the entire dataset.

Data analysis was performed using Amira 5.4 (FEI). The three scan repetitions were averaged, and the brain was segmented for skull stripping. Clusters of iron labeled cells appearing as signal voids on the image were manually segmented on each slice by an experienced observer, taking care to avoid including large blood vessels with similar appearance. A connected component analysis was used to count the total number of metastases, to avoid over counting metastases appearing on more than one image slice.

Prussian Blue Staining and Fluorescent Imaging

At the conclusion of MR imaging, mice were euthanized with CO_2. Brains were rapidly removed from the skull, OCT embedded and frozen. Serial sections (eight microns) were fixed with 4% paraformaldehyde, stained with Pearl’s Prussian blue (PolySciences) to detect iron labeled cells in tissue or DAPI (Life Technologies). The DAPI allowed for florescent detection of nuclei of the brain section and tumor cells were detected by mCherry fluorescent that was retained in the cells. Images were obtained using a Zeiss Axioimager A1 fluorescent microscope equipped with an AxioCam MRc color CCD camera.

Chapter Five

MR Detection of endogenous cell surface receptors

5.1 Introduction

A thorough consideration of the Gd(III) detection limit has revealed a need for significant multiplexing in order to cross the detection limit, likely in the form of a nanoconstruct. This precludes the use of Gd(III) to detect intracellular proteins. However, cell surface receptors are among the most functionally important class of proteins both for understanding cellular function and in clinical diagnosis. Their accessibility make them promising targets for Gd(III)-based molecular imaging. In addition, many of them have small-molecule targeting groups that can be incorporated into existing nanoparticle designs.

Despite their status as a desirable target, imaging cell surface receptors by MRI has been challenging. Typically, these receptors are expressed at a low level, increasing the need for multiplexing Gd(III) chelates. Furthermore, cell surface receptors often have complex subcellular localization, such as receptor-induced endocytosis and cycling through the endoplasmic reticulum back to the plasma membrane (118). While these are still outstanding problems, there is sufficient data about cell surface receptor expression levels to begin selecting targets that may qualify for MR detection. Such a receptor would require an expression level of several hundred thousand copies per cell, at minimum. Also, a target would ideally have a small molecule binding group to act as a targeting moiety. Small molecules are desirable because in they minimally interfere with the nanoparticle surface characteristics, as opposed to an antibody which would have a large effect.

AuDNA-Gd(III)-HA can serve as a valuable starting point for designing surface receptor-targeted nanoparticles, however several improvements on previous designs are required (119). Some evidence suggested that the first generation design had limited stability in media. This can be seen from the observation that cellular uptake was maximized with an eight hour incubation, rather than continually increasing. Also, when the Gd(III) to Au ratio was measured from the cell uptake data, the value appeared to depend on HaloTag expression (Figure 5.1). Both of these properties can be explained by limited stability in media. If eight hours is sufficient to saturate surface HaloTag, then any additional incubation time will not increase Gd(III) uptake, but could decrease it if particle degradation caused Gd(III) to cease being cell associated. Furthermore, HaloTag expression causes changes in the subcellular localization of nanoparticles. Differences in the Gd(III) to Au ratio could reflect different degradation capacities for different locations. In addition to stability concerns, the first generation particles suffered from a complex purification scheme that limits the ability to iterate the design over a library of potential targets. Simplifying the particle construction in effect increases the range of potential targets that can be explored. Finally, every increase in Gd(III) payload opens additional parts of the proteome to MR analysis.

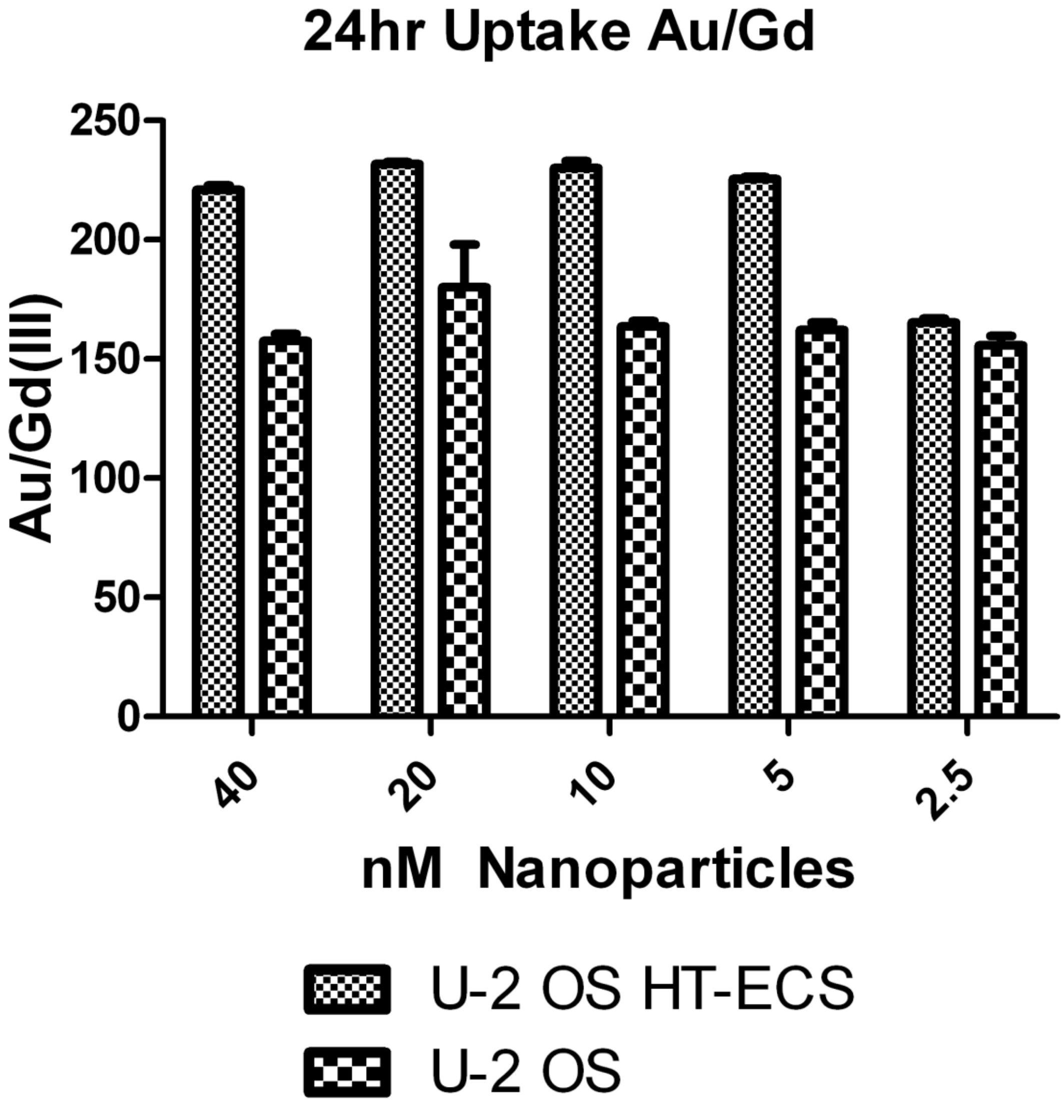

Figure 5.1 Analysis of Au/Gd(III) for first generation nanoparticles.

The dependence on HaloTag expression could be explained by particle instability. Nanoparticle uptake for HT- cells results in endosomal localization, in which case nanoparticle degradation would not result in a loss of Gd(III). For HT+ cells, a significant portion of nanoparticles are on the cell surface, where particle degradation would result in loss of Gd(III). Error bars indicate standard error of the mean.

5.2 Results and Discussion

Improvements in the core nanoconstruct were inspired by recent work in the Meade lab (120). During synthesis of first generation nanoparticles, DNA was added until the surface of the particle became saturated. It is important to note, that this saturation is a result of electrostatic repulsion between negatively charged DNA strands, not due to space limitations (80). Ligand density for a DNA functionalized gold nanoparticle is 0.1 DNA strands/nm^2, whereas neutral polyethyleneglycol can achieve surface densities as high as 6.26 strands/nm^2 (121). It is therefore possible to make use of the remaining space on the nanoparticle. To that end, a neutral Gd(III) chelate was designed with a dithiolane moiety that is capable of binding to the gold surface (Figure 5.2). This discovery enabled a redesign of the previous nanoparticle. As with the previous generation, a thiol-bearing poly-T strand will be used to initially functionalize the Au surface. As before this strand will be equipped with a 5’ amine that will enable coupling chemistry to any suitable targeting group. Unlike the previous version however, this strand will not include any modified bases to attach Gd(III) chelates with click chemistry. Instead, the Gd(III) will be supplied by “backfilling” the neutral Gd(III) chelate onto the remaining space after DNA functionalization Figure 5.3).

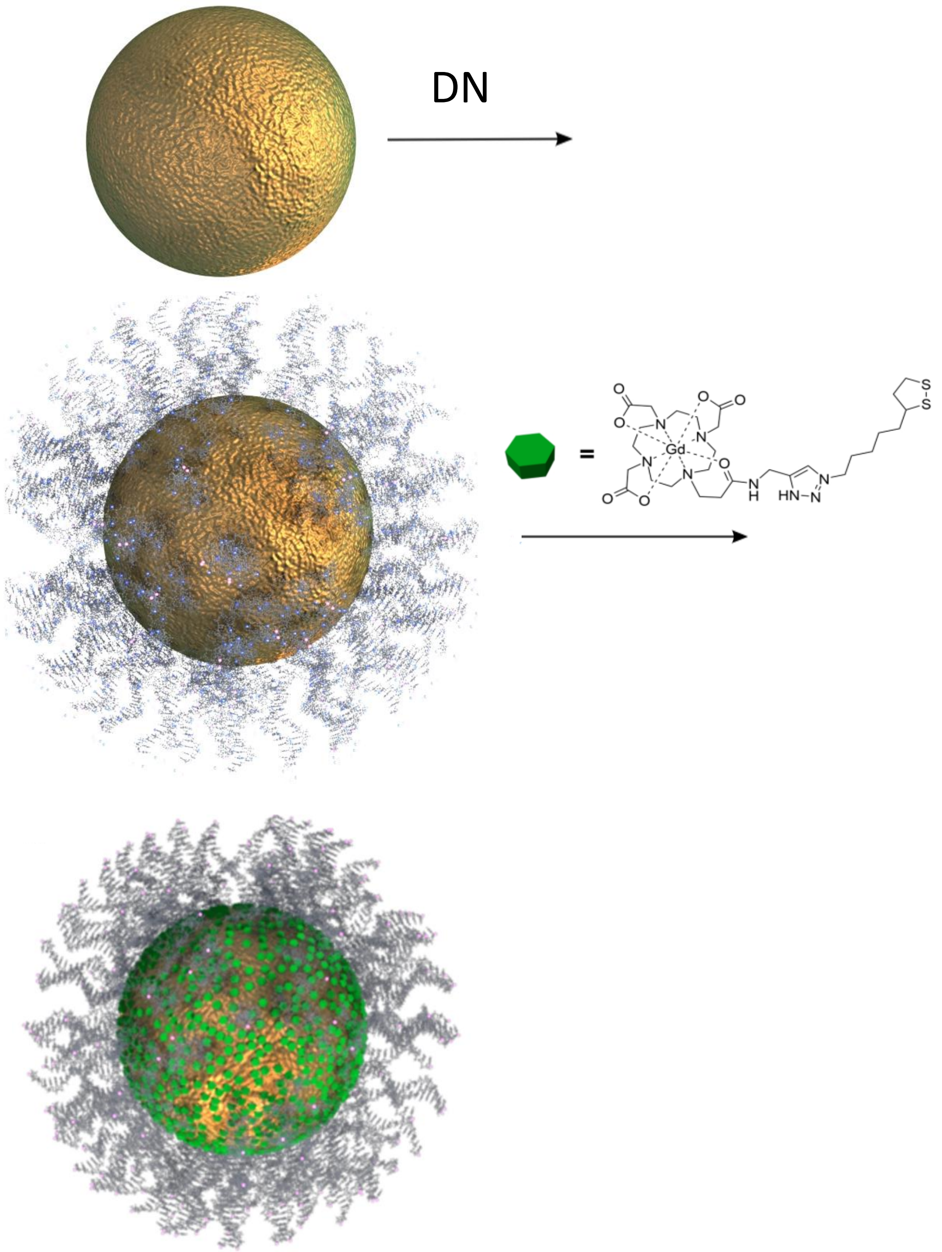

Figure 5.2 Schematic of second generation nanoparticles.

A Au core was saturated with DNA targeted to the chosen surface receptor. After DNA saturation, there is enough remaining space to “backfill” with several hundred neutral Gd(III) chelates.

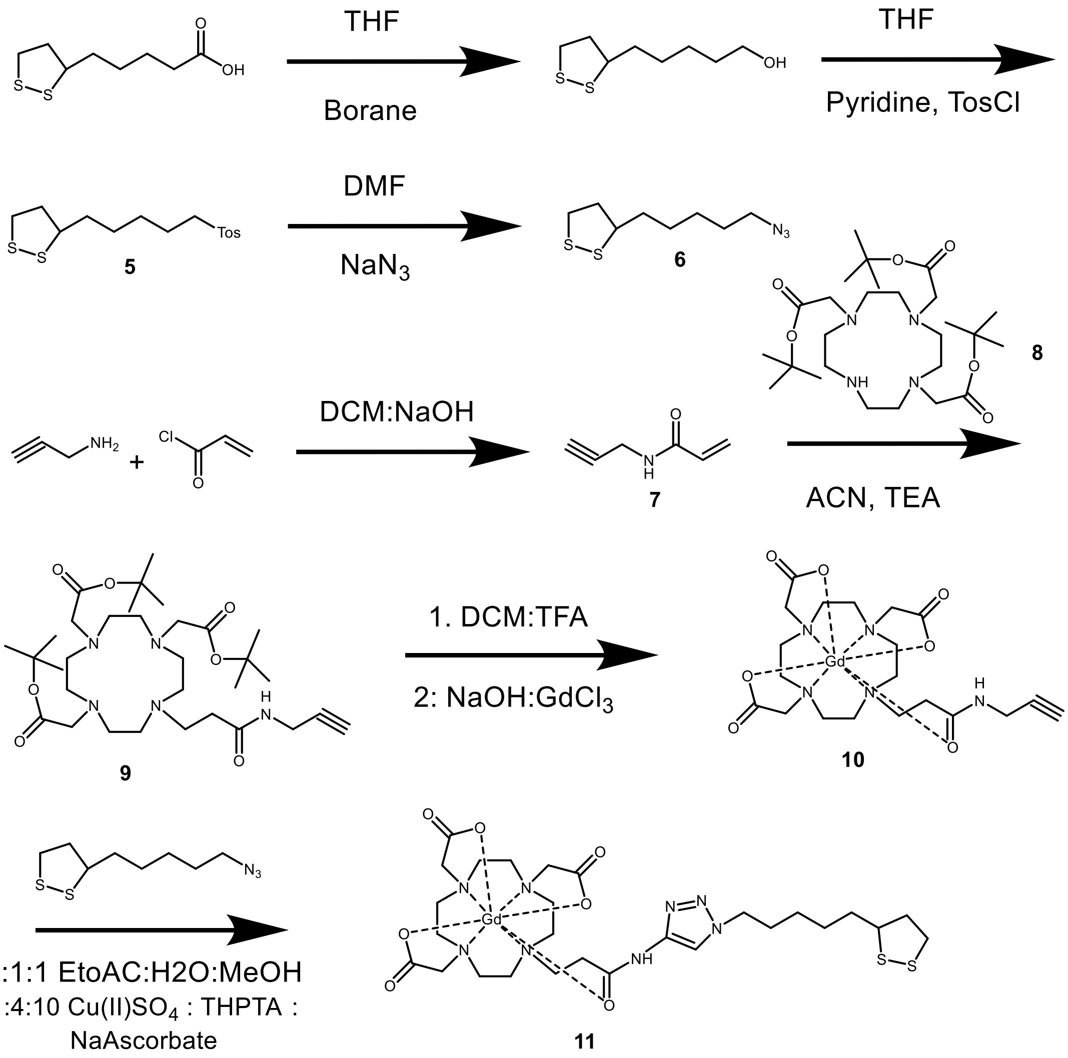

Figure 5.3 Synthetic scheme for Lip603

A chelate with a fast water exchange rate functionalized with a dithiolane from lipoic acid. The sulfur groups will readily bind to a Au surface.

The second generation targeted nanoconstruct improves on the previous generation in several ways. First, Gd(III) payload was increased. Second-generation particles of similar size showed 700 Gd(III) chelates per nanoparticle, whereas first generation particles averaged 560 Gd(III) per nanoparticle. This represents a 25% increase. Second, synthesis of the DNA strand was greatly simplified. The final strand required only one synthetic step to attach the targeting group and one purification step. In addition, the second generation took advantage of recent advances in the Meade lab by using a Gd(III) chelate core with a faster water exchange rate. For each surface receptor target, the basic nanoparticle could be retained, with the only difference being attachment of a targeting group to the DNA strand.

The goal of this study is to determine how broadly applicable this nanoconstruct is for detecting surface receptors. Targets were chosen if they fulfilled several specific criteria. Each had to express at a high level and have a synthetically accessible small-molecule binding group. In addition, the set of targets was chosen to cover a broad variety of surface receptor classes. Folate receptor was chosen because there are commercially available cell lines that express more than 1,000,000 copies per cell, folic acid can be functionalized at the gamma carboxyl and retain binding capacity, and folate receptor can represent targets that undergo receptor-mediated endocytosis (122, 123). Prostate-Specific Membrane Antigen (PSMA) was chosen because it is known to be highly expressed in prostate cancer, has a corresponding small molecule (ZJ-43) that can bind with nanomolar affinity after functionalization, and represents the class of receptor that remain associated with the plasma membrane (124, 125). Finally, HaloTag was included to enable direct comparison to the previous generation of nanoparticles. The modular nature of the nanoparticle core requires that the only feature that changes between targets is the DNA strand. For all three targets and NHS-ester of the targeting group was peptide coupled to an amine-bearing DNA strand (Figure 5.4).

In order to measure target engagement by flow cytometry, each target surface receptor required a corresponding fluorescent targeting group. HaloTag-targeted fluorophores are commercially available. For Folate Receptor and PSMA, fluorescent conjugates of folic acid and ZJ-43 were synthesized (Figure

5.5). In both cases an NHS ester was created to facilitate peptide coupling to an amine functionalized fluorophore. ZJ-43 was coupled to AlexaFlour488 and folic acid was coupled to CF488, a similar fluorophore. In both instances the resulting fluorophore was purified by HPLC and characterized by MALDI.

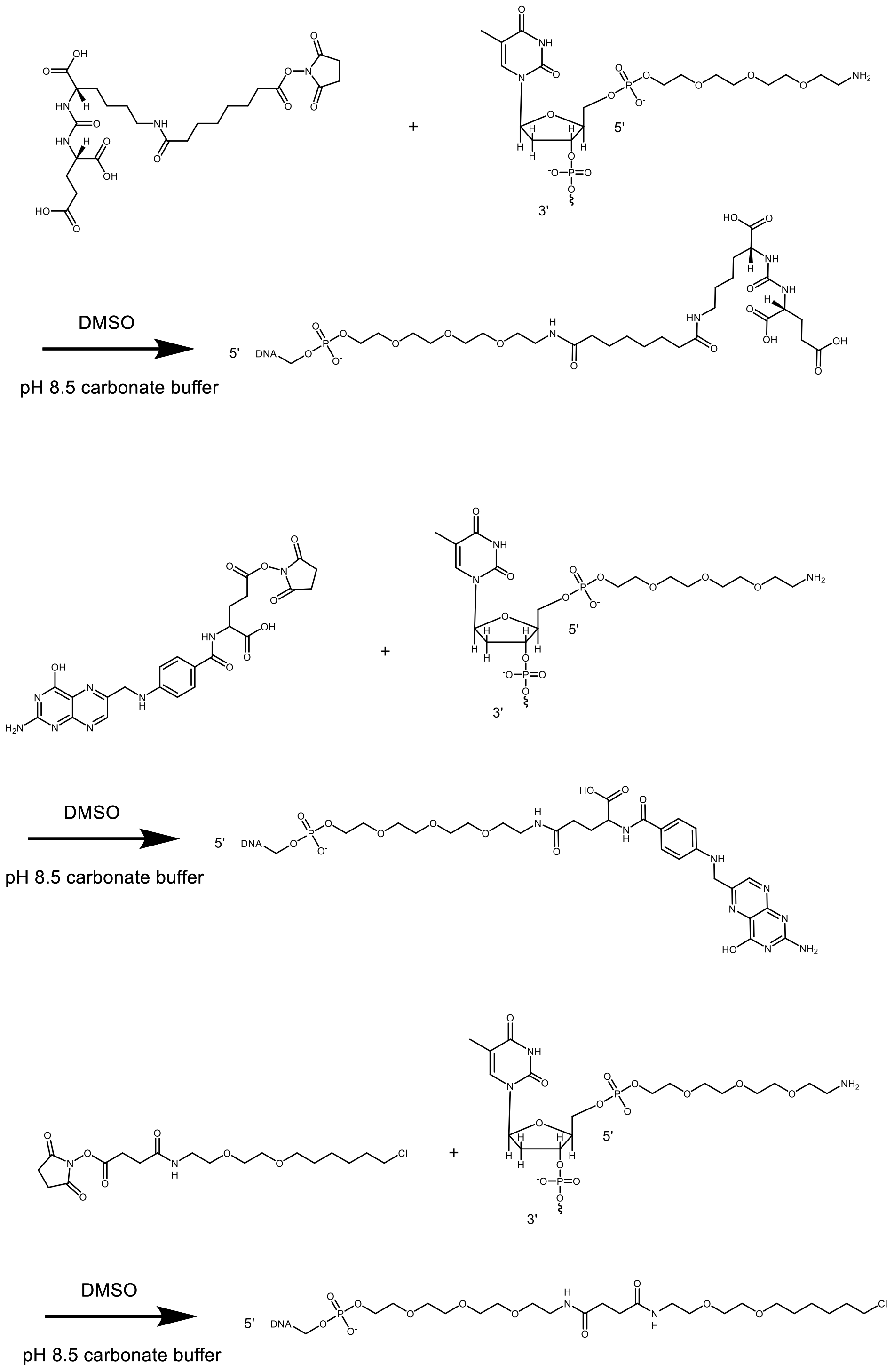

Figure 5.4 The synthetic scheme for each targeted DNA strand.

Folate-NHS synthesis is described in Figure 5.4

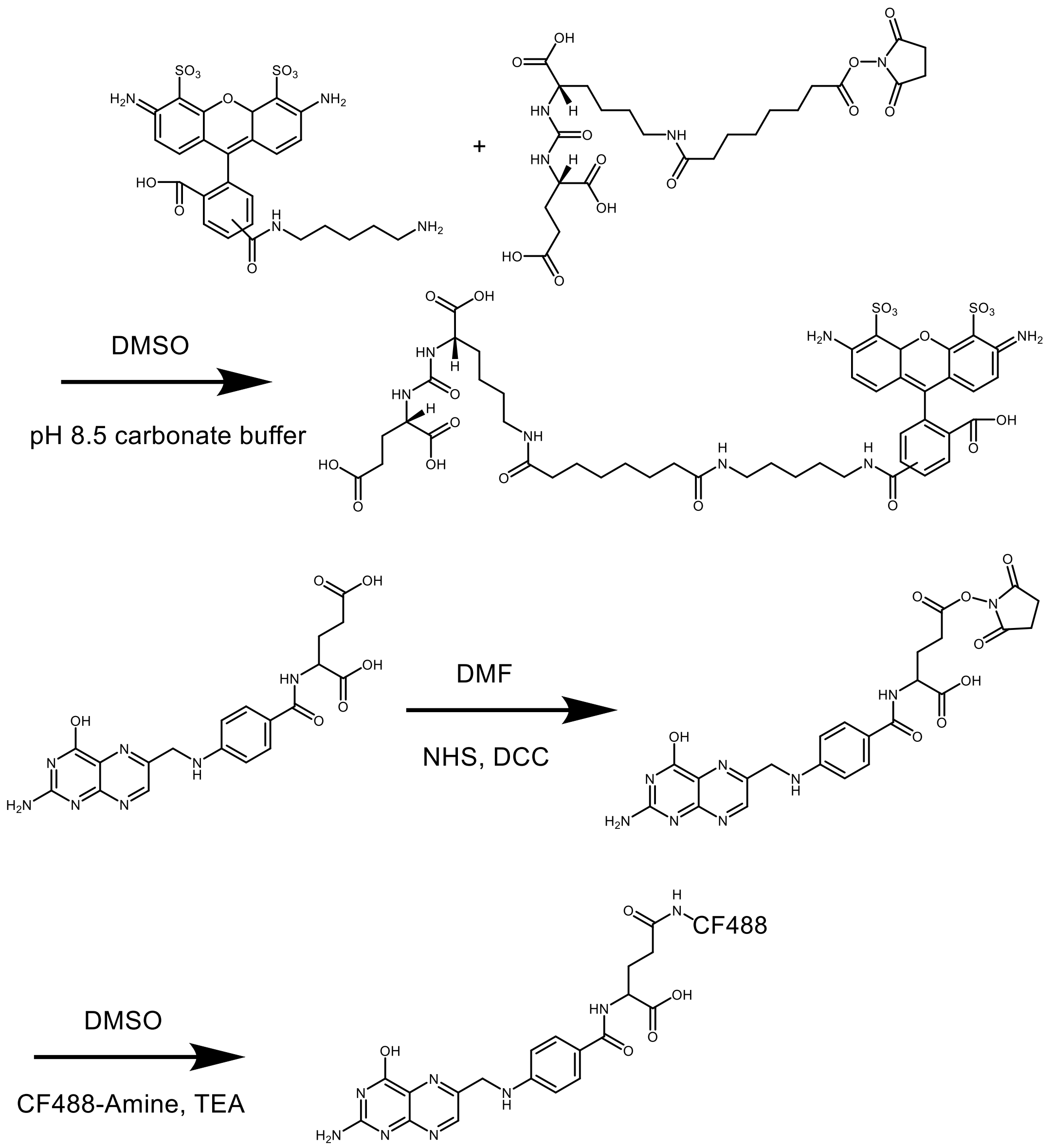

Figure 5.5 The synthetic scheme for surface receptor-targeted fluorophores.

ZJ-43 was attached to AlexaFluor488 and folate was attached to CF488, a similar fluorophore with a proprietary structure.

First and second generations nanoparticles were directly compared for both binding and cellular uptake using HaloTag-targeted DNA. Binding was measured using a modified competition assay. Nanoparticles compete with a HaloTag-targeted fluorophore for binding sites, and the degree of binding can be measured as a loss of fluorescence by flow cytometry (Figure 5.6). First and second generation nanoparticles display very similar concentration dependent binding. Second generation nanoparticles displayed somewhat slower binding kinetics (Figure 5.7). However, both first and second generation approached saturation after 8 hours. Measuring the uptake of both Gd(III) and Au revealed several superior properties for second generation nanoparticles. First, second generation nanoparticles achieved threefold more Gd(III) in HT+ cells vs HT- cells (Figure 5.8). Second, second generation nanoparticles showed measurably higher uptake at all dosed concentrations, whereas first generation nanoparticles required a minimum of 20nM to induce differential uptake. Finally, the Gd(III)/Au ration indicated that the particles had improved stability, as there was no difference in the ratio between HT+ and HT- cells (Figure 5.8).

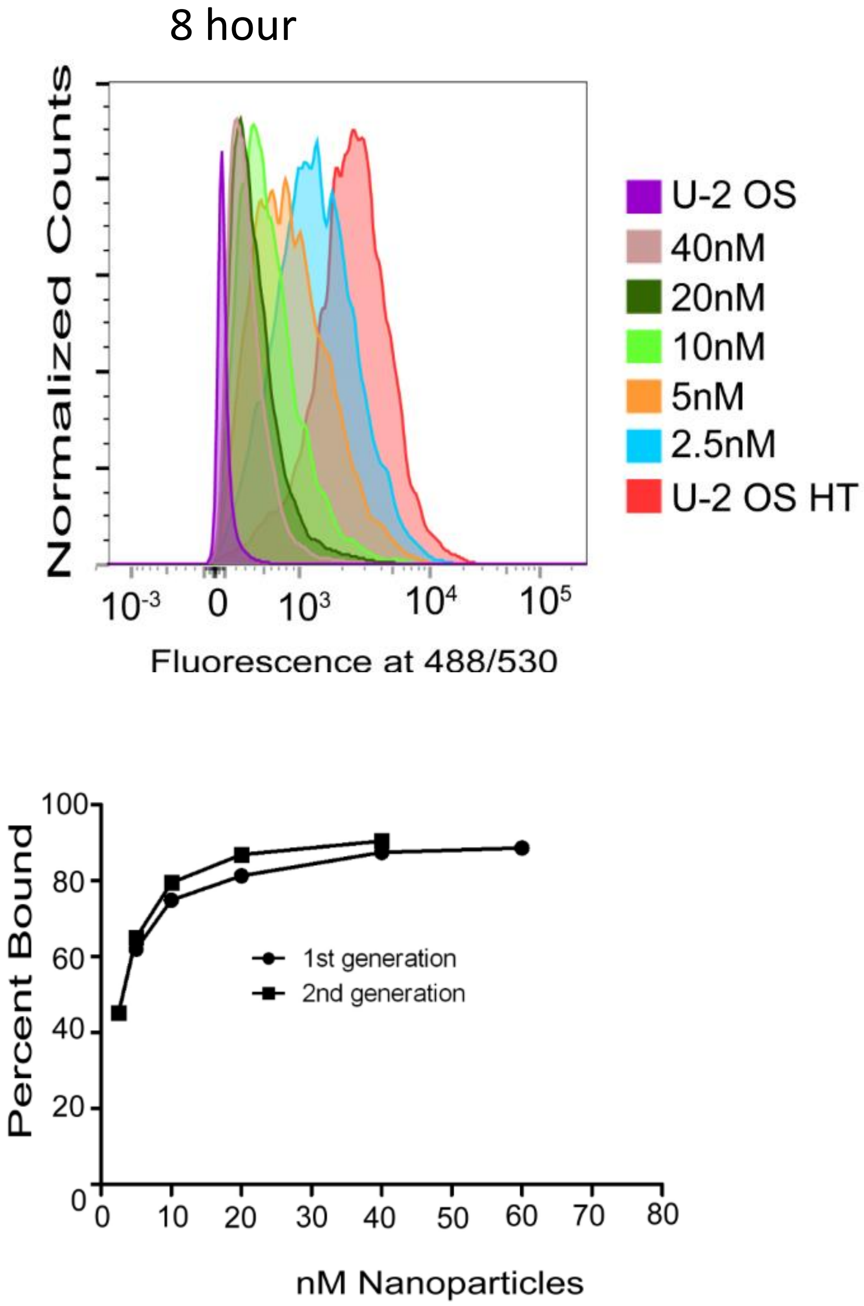

Figure 5.6 Comparison of the concentration-dependent binding for first and second generation nanoparticles.

Cells were incubated for 8 h at the indicated concentration before being labeled with a HaloTag targeted fluorophore. Binding is largely similar between the two constructs.

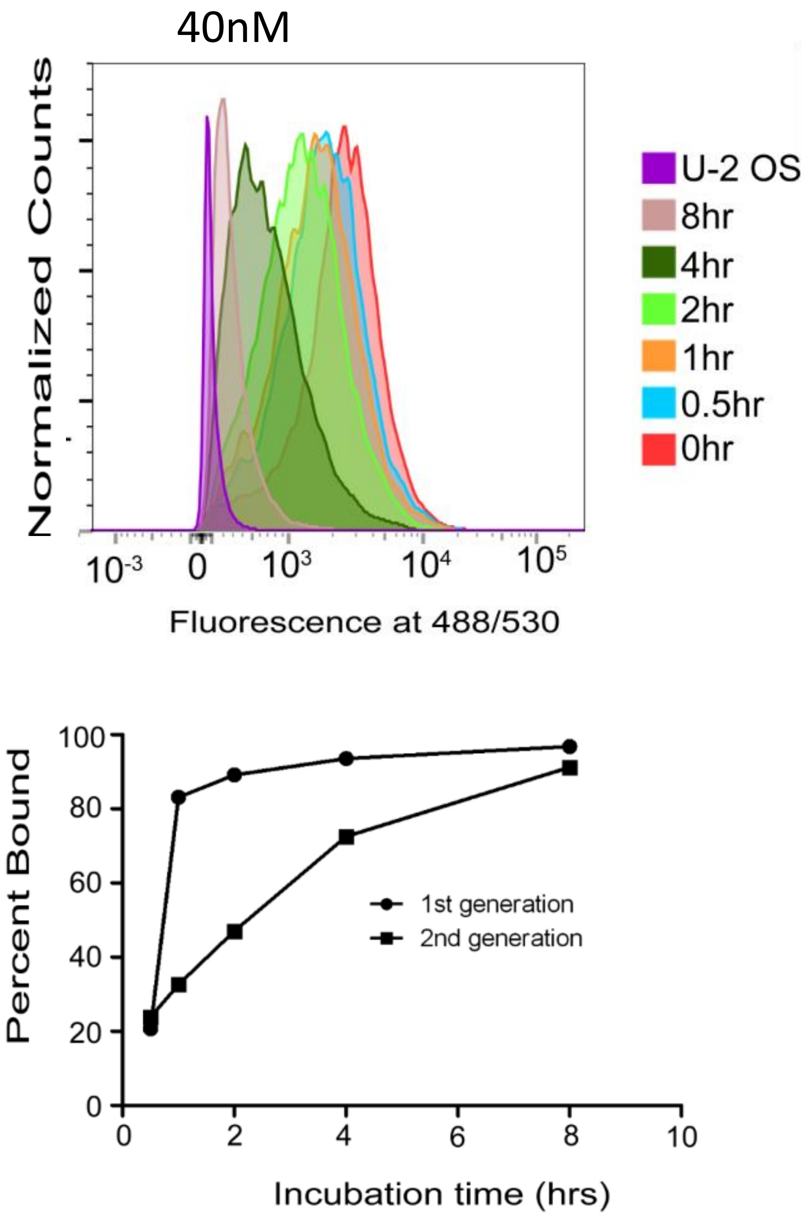

Figure 5.7 Comparison of time course binding between first and second generation nanoparticles. Cells were incubated with 40 nM nanoparticles for in the indicated amount of time before being labeled with a HaloTag-targeted fluorophore. While second generation nanoparticles display slower kinetics, both become saturated after 8 h.

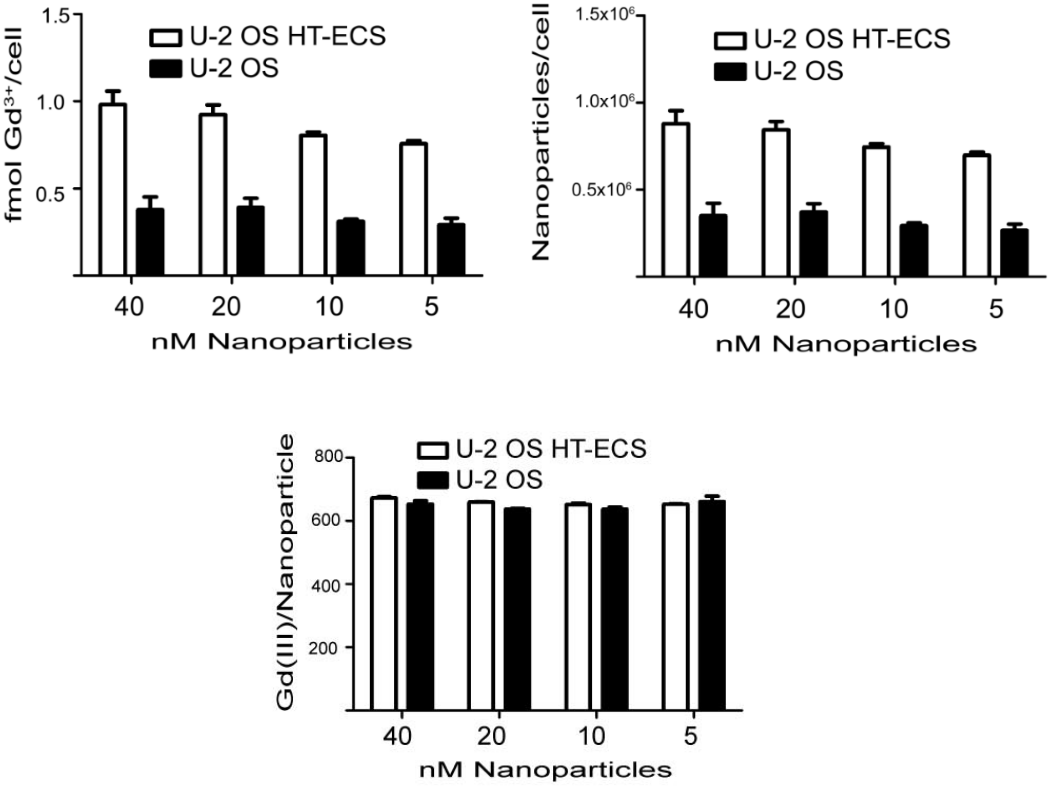

Figure 5.8 Uptake of Au and Gd(III) after an incubation with second generation nanoparticles.

Even at 5 nM, there is significantly more Gd(III) and Au in HT+ cells. In addition, the Gd(III)/Au ratio was used to back calculate the loading of Gd(III) onto nanoparticles. This value is constant between HT+ and HT- cells and reflects the value of 700 Gd(III)/nanoparticle measured prior to cell studies. Total incubation time was 8 h. Error bars indicate standard error of the mean.

After verifying that second generation nanoparticles can deliver more Gd(III) with higher stability, their ability to bind to folate receptor was measured. This measurement was performed using the same methods as the HaloTag binding experiment above, replacing HaloTag-targeted DNA and fluorophores with folate receptor targeted versions. KB cells were used due to their high expression level of folate receptor, and when being treated with either probe the cells were cultured in folate-free media. In order to produce a negative control, cells were pre-treated with a saturated solution of folate to compete with the probe. Cells were exposed to a variety of nanoparticle concentrations for 8 h (Figure 5.9). Interestingly, more than 60% binding was observed at all measured concentrations, down to 1.3 nM. For comparison, HaloTag-targeted nanoparticles displayed 42% binding at 5 nM. This increase in efficiency can be explained by the low K_d of folate for its receptor. Even at 1.3 nM nanoparticles, the concentration of folate could be as high as 260 nM (assuming 200 DNA strands per particle), well above the K_d of 0.4 nM (126).

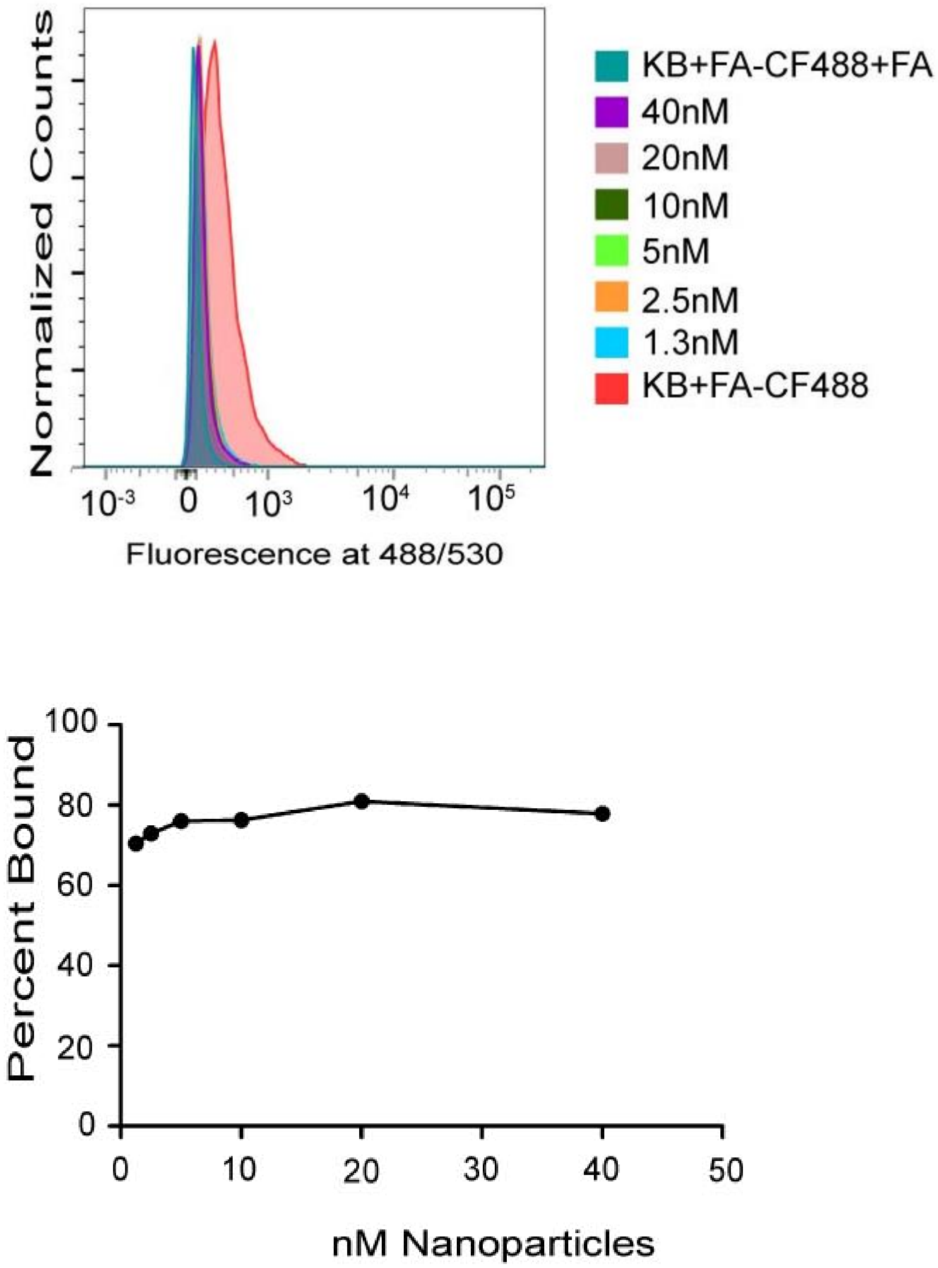

Figure 5.9 The concentration-dependent binding for folate receptor-targeted nanoparticles. Cells were incubated for 8 h at the indicated concentration before being labeled with a folate receptor targeted fluorophore. Binding is above 60% at all measured concentrations.

5.3 Conclusion and Future Directions

This preliminary study has yielded several promising results for imaging cell surface receptors by MRI. By moving the Gd(III) onto the surface of the nanoparticle, stability was greatly increased. This improved the likelihood that these agents will maintain their functionality in an *in vivo* setting, where there may be several days between injection and imaging. A surprising second benefit of moving the Gd(III) is a sharp reduction in the concentration of nanoparticles required to generate differential uptake, from 20 nM in first generation nanoparticles to 5 nM in second generation. Additionally, there appears to be a large benefit to multiplexing the targeting group in the case of folate receptor, with a 1 nM dose being capable of binding more than half the available receptors.

In addition to promise, there are also several additional challenges that must be addressed. Chief among them is the transition to *in vivo* models. Each of the selected targets have suitable xenograft models in mice that can be used to show that the promising *in vitro* results will translate. This is the only experiment that can prove broad applicability. In addition, there are several minor characterization problems that need to be addressed. Folate receptor requires an uptake study to validate the predicted expression level, and PSMA requires both binding data and uptake data before an *in vivo* model can be explored. In addition, improvements to the purification procedure for the targeted-DNA could improve binding capacity, as MALDI indicated a significant amount of untargeted DNA.

5.4 Materials and Methods

5.4.1 Chemical Synthesis and Characterization

Synthesis of Targeted DNA

Addition of the targeting functionality was performed by peptide coupling. HaloTag (1 mg), ZJ-43 (0.4 mg), or folate (10 mg) NHS esters were dissolved in 400 µL DMSO and combined with 1 µM 3’-disulfide-$(T)_{24}$-amine-5’ DNA from IDT dissolved in 400 µL pH 8.5 carbonate buffer (Figure 5.3). The reaction is allowed to stir overnight. The mixture was concentrated *in vacuo,* dissolved in H_2O, and purified on a pre-packed G25 sephadex column (NAP-5, GE life sciences)

Folate-NHS

To a flame-dried flask was added folic acid (50 mg, 0.113 mmol) and NHS (13 mg, 0.133 mmol). This vessel was placed under vacuum for 60 min. The flask was then placed under dry N_2 and 20 ml anhydrous DMF was added to flask and allowed to stir for 60 min. DCC (15 mg, 0.076 mmol) was then added and the mixture was allowed to stir 16 h protected from light. A 20 ml solution of 30% acetone in ether was added to the solution, resulting in the formation of a yellow precipitant. This was filtered over a glass frit and used immediately without further purification.

ZJ-43-AlexaFluor488

To a 1.5 ml microcentrifuge tube was added AlexaFluor488 Cadaverine (Sigma, 0.75 mg, 1.17 µmol) and dissolved in 0.75ml pH 8.5 carbonate buffer. Separately, ZJ-43-NHS (0.1 mg, 1.76 µmol) was dissolved in DMSO. The two solutions were mixed together and allowed to stir overnight. The mixture was then concentrated *in vacuo,* purified by reverse phase HPLC, and characterized by MALDI-MS

Folate-CF488

Folate-NHS (10 mg, 0.02 mmol) was dissolved in 1 mL DMSO. Separately, CF488-NH_2 (Sigma) was dissolved in 1 ml DMSO along with one drop TEA. The solutions were then combined and allowed to stir 16 h protected from light. The resulting mixture was concentrated *in vacuo*. The mixture was dissolved in H_2O and the soluble portion used for reverse phase HPLC purification. The product was characterized by MALDI-MS

*Tosyl-protected Lipoic Alcohol (**5**)*

To a flask was added lipoic acid (0.10 g, 0.48 mmol) and 10 ml THF. The solution was cooled to 0˚C and allowed to stir. A 1.0 M solution of BH_3 in THF (2.4 ml) was added to the stirring solution. The mixture was slowly warmed from 0˚C to room temperature over 3 h. The reaction mixture was then cooled to 0˚C again and quenched with 5 ml MeOH. The mixture was extracted three times into ethyl acetate, washed with saturated sodium bicarbonate, and dried over sodium sulfate. The reaction mixture was concentrated *in vacuo*. To this mixture was added 5 ml THF and 15 ml pyridine and the mixture was cooled to 0˚C and allowed to stir. Tosyl chloride (0.19 g, 0.96 mmol) was dissolved in 2 ml THF and added to the stirring mixture. It was allowed to stir an additional 16 h. The mixture was extracted three times into ether, washed with saturated sodium bicarbonate, washed in brine, and dried over sodium sulfate. The reaction mixture was concentrated *in vacuo* and purified by flash chromatography on silica with a 1:1 Ethyl Acetate:Hexanes mobile phase. The product was characterized by NMR

*Lipoic Azide (**6**)*

To a flask was added Tosyl-protected Lipoic Alcohol (1.58 g, 4.8 mmol), sodium azide (0.468 g, 7.2 mmol), and 20 ml DMF. The mixture was heated to 60˚C and stirred. Trace amounts of KI were added. The mixture was allowed to stir for 72 h. The mixture was concentrated *in vacuo*, extracted three times into ether, washed with saturated sodium bicarbonate, washed in brine, and dried over sodium sulfate and once again concentrated *in vacuo*. The product was characterized by NMR.

*Alkyne Arm (**7**)*

To a flask was added propargylamine (1.29 g, 23.4 mmol), acryloyl chloride (6.36 g, 70.3 mmol), and 125 ml DCM. 50 ml of 1.25 M NaOH was added and the biphasic mixture as allowed to stir 16 h. The aqueous layer was removed and extracted with 20 ml DCM three times. The solution was then washed with saturated sodium bicarbonate and dried over sodium sulfate. It was then concentrated *in vacuo*, purified by flash chromatography on silica with a 1:1 Ethyl Acetate:Hexanes mobile phase, and characterized by ESI-MS and NMR

9

T-butyl DO3A was synthesized using previously reported methods (119).To a flask was added T-butyl DO3A (1.95 g, 3.26 mmol), K_2CO_3 (2.25 g, 16.3 mmol), and 230 ml anhydrous ACN. The mixture was allowed to stir for 5 min at which time **7** (1.6 g, 14.9 mmol) was added. The mixture was stirred at reflux for 96 h. The mixture was filtered over celite and concentrated *in vacuo*. It was used immediately without any further purification. The product was characterized by ESI-MS

10

To a flask was added crude **9** and 25 ml 1:1 DCM:TFA. The mixture is stirred at room temperature for 12 h. Reaction progress is measured by ESI-MS. The mixture was then concentrated by blowing N_2, dissolving in methanol, and finally concentrating *in vacuo* (3x25 ml) to remove any residual TFA. To this brown oil was added 25 ml H_2O and Gd(III)Cl_3 6H_2O (1.46 g, 3.9 mmol). 1M NaOH was added dropwise to maintain a pH of 5.5. The mixture was then allowed to stir for 24 h. The product was purified by HPLC and characterized by ESI-MS.

11

To a flask was added lipoic azide (**6**) (0.036 g, 0.16 mmol), **10** (0.1 g, 0.16 mmol), Tris(3-hydroxypropyltriazolylmethyl)amine (0.026 g, 0.06 mmol), and Cu(II)SO_4 5H_2O (0.007 g, 0.03 mmol). The components were dissolved in a 1:1 mixture of ethyl acetate and H_2O (20 ml total) and allowed to stir. MeOH (10 ml) was then added and the reaction allowed to stir 16 h. The mixture was concentrated *in vacuo*, purified by reverse phase HPLC, and characterized by ESI-MS.

Nanoparticle construction

The second generation nanoparticle was constructed by binding the DNA strand to the nanoparticle using a salt aging procedure. Specifically, 29 OD (260 nm) of DNA (corresponding to ~200 strands of DNA per nanoparticle) was dried into a 1.5 mL microcentrifuge tube, to which is added 300 µL of 100 mM dithiothreitol in 180 mM (pH 8.0) phosphate buffer. The solution is left to stir at room temperature for 1 hour. After such time, the DNA is run through a pre-packed G25 sephadex column (NAP-5, GE life sciences) using 180 mM phosphate buffer as the mobile phase, monitoring elution by UV/Vis at 260 nm.

To 50 mL of 10 nM citrate stabilized gold nanoparticles in water is added 54 µL of tween 20 (for a total concentration of 0.01% v/v) and deprotected and purified DNA in 4 mL 180 mM phosphate buffer. The solution is then sonicated for 30 seconds and left to stir for 30 minutes. Over the subsequent five hours, a solution of NaCl (4.753 M), phosphate buffer (10 mM) and 0.01% tween 20 is added in increments of 1.25, 1.29, 1.32, 1.35 and 1.38 mL per hour, with each addition followed by 30 seconds of sonication. During the intervening time, the solution is left to stir at room temperature. The final concentration of NaCl is 600 mM. The solution is left to stir for a further 48 hours. At this time **11** (0.005 g, 6 µmol) was added to the solution, corresponding to >1000 chelates per nanoparticle. This solution was allowed to rotate 16 h.

Purification of AuDNA-Gd(III)-HA is conducted by three rounds of centrifugation at 4 °C (30 minutes at 21.1 x g), followed by resuspension in fresh DPBST (0.01% Tween20). This procedure yielded up to 4 nmol AuDNA-Gd(III)-HA from 5 nmol citrate stabilized gold nanoparticles.

5.4.2 Cell Culture

U-2 OS (ATCC) and U-2 OS HT-ECS (Promega) cells were cultured in McCoy's 5A supplemented with 10% FBS (VWR). U-2 OS HT-ECS media was supplemented with 800 µg/ml G418 (Life Technologies). KB (ATCC) cells were cultured in in McCoy's 5A (Life Technologies), either with or without folate, and supplemented with 10% FBS (VWR). PC-3 PIP and PC-3 Flu (Dr. Martin Pomper) were cultured in in RPMI supplemented with 10% FBS (VWR). All cells were maintained at 37°C in a 5% CO_2/95% humidified air atmosphere.

Cell Uptake

Cells were incubated with the indicated concentration of nanoparticle probe for 8 h. They were then rinsed in the plate once with Dulbecco's phosphate buffered saline (DPBS), trypsinized, treated with trypsin inhibitor, and collected into microcentrifuge tubes. The cells were then pelleted at 1000g for 5 minutes at 4°C. Cell pellets were washed twice by resuspending in 400µL DPBS and pelleting. The pellet was suspended in 200 µL DPBS and resulting suspension of cells was split into two groups, 50 µL for cell counting and 140 µL for ICP analysis.

Cells were counted using a Guava EasyCyte Mini Personal Cell Analyzer (EMD Millipore). After cell resuspension, an aliquot (50 µL) of the suspension was diluted in Guava ViaCount reagent (150 µL).

Stained samples were vortexed for 10 s and then cells were counted using a Guava EasyCyte Mini Personal Cell Analyzer (PCA) using the ViaCount software module***.***

Quantification of gadolinium for cell uptake experiments was accomplished using ICP-MS of acid digested samples. Specifically, aqueous samples were digested in concentrated nitric acid (> 69%, Sigma) and hydrochloric acid (37% BDH) and heated to 75 °C for overnight. Samples were then diluted with ultra-pure H_2O (18.2 MΩ·cm) and multi-element internal standard (CLISS-1, Spex Certiprep) to 3.0% nitric acid (v/v) and 5.0 ng/mL internal standard in a total sample volume of 3 mL. Individual Gd elemental standards were prepared at 0.78125, 1.5625, 3.125, 6.25, 12.5, 25.0, 50.0, 100, and 200 ng/mL concentrations with 3.0% nitric acid (v/v) and 5.0 ng/mL internal standards up to a total sample volume of 10 mL.

ICP-MS

ICP-MS was performed on a computer-controlled (Plasmalab software) Thermo X series II ICP-MS (Thermo Fisher Scientific) operating in standard mode equipped with a CETAC 260 autosampler (Omaha). Each sample was acquired using 1 survey run (10 sweeps) and 3 main (peak jumping) runs (100 sweeps). The isotopes selected for analysis were ^{57}Fe, and ^{115}In and ^{165}Ho (chosen as internal standards for data interpolation and machine stability). Instrument performance is optimized daily through autotuning followed by verification via a performance report (passing manufacturer specifications).

Receptor Binding Assay

Cells were plated and treated with the nanoparticle probes in media. In the case of KB cells, the negative control was treated a solution of saturated folate in DMSO, 1:300 DMSO:media. Doped media was then removed and labeled with receptor-binding fluorophores. Cells were labeled by first treating them with trypsin, follow by inhibition with media, and collected into microcentrifuge tubes. The cells were then pelleted at 1000g for 5 minutes at 4°C. Media doped with 1 µM fluorophore was used to resuspend the cells. After a 15 minute incubation at 37°C, cells were pelleted at 1000g for 5 minutes at 4°C, resuspended in 400µL DPBS, spun down again, and finally resuspended in DPBS with 2% bovine serum albumin (Sigma-

Aldritch) for flow cytometry. Analysis was performed on a LSR II (BD) flow cytometer and data were analyzed using FlowJo software (Treestar). For experiments on the folate receptor, folate free media was used. In addition, for blocking experiments, a saturated solution of folate in DMSO was added to each well 1:500 v/v.

Chapter Six - Appendix

Targeted Inhibition of Snail Activity in Breast Cancer Cells Using a Co(III)-Ebox Conjugate

Reproduced from Vistain *et al*. ChemBioChem, 2015 with permission from The Royal Society of Chemistry

6.1 Introduction

Tumor metastasis is the process whereby cells disseminate from a primary tumor and are established as secondary tumors at a distal site. This process is the leading cause of cancer-related deaths. Because most tumors are of epithelial origin, metastasis requires that these cells lose their cell-cell adhesions and adopt a mobile, invasive phenotype. Although inhibition of this process may lead to successful treatment of many cancers, it is a complex, multistep process that has been difficult to target for therapy. Current strategies include inhibition of tumor cell survival in the bloodstream, (127) prevention of cell attachment at the secondary tumor site (128) and inhibiting extracellular proteins such as matrix metalloproteinases to prevent degradation of the extracellular matrix (129). Notably, none of these approaches effectively treat metastasis *in vivo*. Antimetastatic capacity could be improved if drugs were able to suppress multiple metastatic traits simultaneously.

The Snail TF has been associated with metastatic tumors and it is believed that this is a result of Snail's involvement in cellular adhesion and motility (130-133). Snail is most commonly associated with a distinct phenotypic change called the epithelial-to-mesenchymal transition (EMT) and is integral to embryogenic morphogenesis and fibrosis.(134) It is widely recognized that there are significant similarities between EMT and the progression to an invasive phenotype that develops in cancer (135-137). Furthermore, Snail is believed to be a key component of both phenotypes. Snail family TFs bind to a consensus CAGGTG sequence known as the Ebox sequence via a Cys_2His_2 type zinc-finger where it acts as a transcriptional repressor, inhibiting the expression of target genes such as E-cadherin and other epithelial markers (138). This transcriptional repression leads to the development of a mobile phenotype (139) (Figure 6.1). It has been well documented that epithelial tumors reduce E-cadherin as they progress toward malignancy (140-143). Beyond repression of E-cadherin, Snail expression results in a decrease in cell-cell adhesions, an increase in cellular motility, an upregulation of cell survival genes, and expression of extracellular matrix remodeling proteins (133).

A critical barrier to inhibiting TFs is that pharmacological manipulation remains elusive (144). Unlike enzyme active sites, TFs generally lack specific binding sites for small molecules to inhibit the function of the protein (144). With the exception of drugs targeting TFs of the nuclear hormone-receptor super family, TFs are generally considered “undruggable.”(144) For example, most TF-targeted drugs rely on reversible interactions to disrupt TF-DNA binding, necessitating the use of high concentrations of the drug to achieve effective modulation (144, 145). An alternate approach to targeting TFs is to use DNA as a decoy to bring TFs into proximity with an effector moeity capable of disabling the TF (146, 147).

Co(III)-Schiff base complexes (Co(III)-sb consisting of the tetradentate bis(acetylacetone)ethylenediimine (acacen) as the equatorial ligand and ammines as axial ligands have been shown to irreversibly inhibit the activity of histidine(His)-containing proteins such as thermolysin, α-thrombin and matrix-metalloproteinases (148-151). The labile axial ligands of the Co(III)-sb moiety undergo dissociative ligand exchange with the imidazole ring of essential His residues in the binding site of the protein, causing irreversible disruption of protein structure and loss of function (152-154).

Specificity can be incorporated into Co(III)-sb inhibitors by conjugation to a targeting moiety such as a peptide or oligonucleotide (148, 150, 155, 156). A Co(III)-sb complex tethered to a decoy Ebox sequence oligonucleotide (Co(III)-Ebox; (Figure 6.1) has been previously reported and has shown remarkable specificity and efficacy in the inhibition of Snail family TFs involved in embryonic neural crest development of *Xenopus laevis*.(148, 155) When Co(III)-Ebox is administered to cells undergoing EMT, Snail family TFs are expected to reversibly bind to the decoy oligonucleotide. This binding event will bring the TF in close proximity to the inhibitor and allowing for specific inhibition (Figure 6.1). Considering the high specificity and efficacy of the Co(III)-Ebox conjugate, this strategy has the potential to overcome the shortcomings of previously studied TF inhibitors.

Based on the highly specific and efficient inhibition of EMT by Co(III)-Ebox observed in embryonic neural crest development, this approach has strong potential as a TF inhibitor that could be used in the treatment of metastasis (148, 155). To further investigate this, the capability of Co(III)-Ebox to inhibit artificially induced EMT was studied in breast cancer cells. EMT induction was achieved in SKBR3 and MCF7 epithelial breast cancer cells by treatment with heregulin-β1 (HRG, or neuregulin), a known inducer of EMT in these cell lines (157). Snail has explicitly been shown to be essential for this transition for

SKBR3 cells, and in both cell lines Snail has been shown to localize to the nucleus after exposure to HRG (157, 158). It is hypothesized that inhibition of Snail activity with Co(III)-Ebox will result in attenuation of multiple mesenchymal traits in these cells. The effects of Co(III)-Ebox were analyzed from multiple aspects to characterize its *in vitro* efficacy as an antimetastatic agent with particular emphasis on studying the functional aspects of inhibition of Snail.

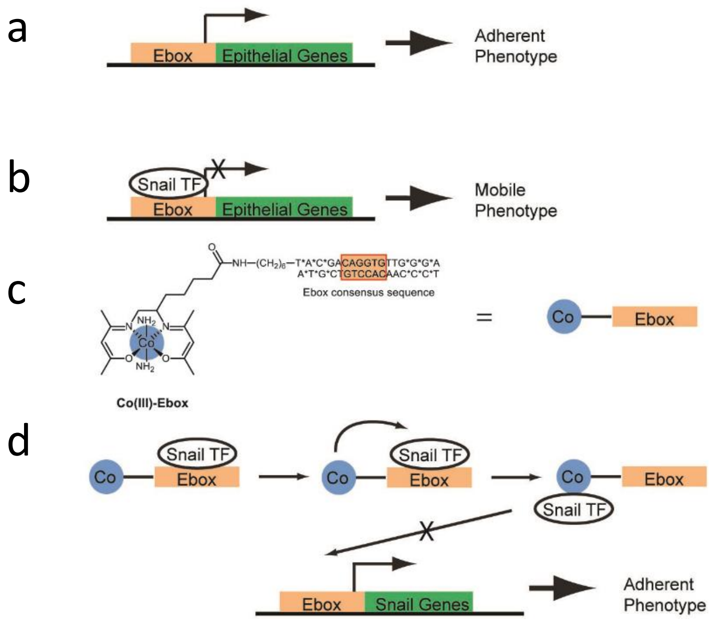

Figure 6.1 Schematic showing the predicted mode by which Co(III)-Ebox inhibits Snail family TF-mediated metastasis.

a) The cells remain adherent when the Ebox consensus sequence is unoccupied (139). b) The cells acquire a mobile phenotype when Snail family TFs bind to the Ebox consensus sequence and inhibit target gene transcription (139). c) The structure of Co(III)-Ebox. Co(III)-Ebox is a conjugate of Co(III)-sb peptide-coupled to an amine-modified Ebox oligonucleotide. * indicates the nucleotides with phosphorothioate bonds that prevent nuclease degradation. d) Co(III)-Ebox inhibits Snail family TFs from binding to the Ebox consensus sequence. Snail family TFs are believed to reversibly bind to the targeting decoy oligonucleotide, bringing the TF into close proximity of the Co(III)-sb inhibitor to elicit irreversible inhibition.

6.2 Results and Discussion

The ability of Co(III)-Ebox to selectively block Snail-induced motility in tumor-derived cells was examined. In previous studies Snail-mediated transcriptional repression was shown by transfecting epithelial cells with murine *Snai1* to achieve selective expression of Snail. This was to determine a clear link between the effects of Co(III)-Ebox and the presence of its target (148, 155). In the present study the ability of Co(III)-Ebox to prevent phenotypic changes from endogenous Snail induced by HRG in cancer cells is explored.

HRG is a member of the EGF-like growth and differentiation factors that binds with high affinity to the receptors ErbB3 and ErbB4 (159). HRG is overexpressed in breast cancers and is strongly associated with cancer progression, metastasis, aggressive clinical course and poor prognosis of the disease (160-162). *In vitro*, HRG is known to transform MCF7(163) and SKBR3(158) epithelial breast cancer cell lines to a more invasive and aggressive phenotype, and has been associated with induction of EMT (157). Since HRG is capable of inducing EMT in these cell lines within 48 h, it was used to test the efficacy of Co(III)-Ebox at inhibiting the effects of Snail.

The ability of Co(III)-Ebox to alleviate transcriptional repression of the E-cadherin promoter was examined. 20 ng mL^{-1} HRG causes a time-dependent decrease of E-cadherin expression in cells transfected with the wildtype luciferase reporter gene construct (Ecad-luc) (Figure 6.2). To ensure that this is an effect mediated by Snail binding to the E-cadherin promoter, the experiment was repeated using the mutated luciferase reporter gene construct (EcadMut-luc) that does not bind Snail (164). Cells transfected with EcadMut-luc did not show a decrease in E-cadherin expression in response to HRG (Figure 6.3). To test the inhibitory effect of Co(III)-Ebox, the cells were cotransfected with 40 nM Co(III)-Ebox and the Ecad-luc construct. As a result of having a nuclear export sequence, Snail resides in the cytosol in unstimulated cells(165). Therefore, transfection agents which deposit cargo into the cytosol can effectively deliver Co(III)-Ebox to Snail (41). The concentration of Co(III)-Ebox and transfection agent used has previously been shown to be non-toxic to the cells (155). HRG-induced decrease in E-cadherin expression was inhibited, showing that Co(III)-Ebox alleviates the repression of E-cadherin expression (Figure 6.2).

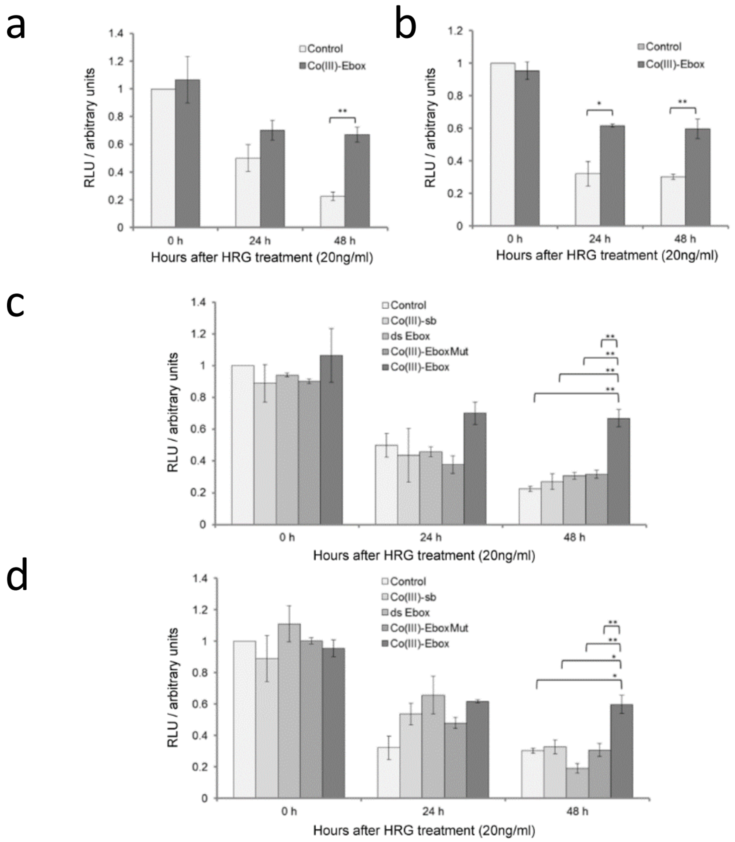

Figure 6.2 Co(III)-Ebox treatment alleviates the HRG-induced decrease in E-cadherin expression in breast cancer cells.

a) SKBR3 and b) MCF7 cells transfected with the luciferase reporter show a time-dependent decrease in E-cadherin expression in response to HRG. This effect of HRG is alleviated when co-treated with Co(III)-Ebox. Error bars indicate standard error of the mean. n = 3. Student's t-tests determined statistical significance from control treatment groups where *P<0.05 and **P<0.005. c) SKBR3 and d) MCF7 cells do not show the same inhibition of E-cadherin expression as Co(III)-Ebox following treatment with Co(III)-sb, ds Ebox or Co(III)-EboxMut. Error bars indicate standard error of the mean. n = 3. Student's t-tests determined statistical significance from control treatment groups where *P<0.05 and **P<0.005.

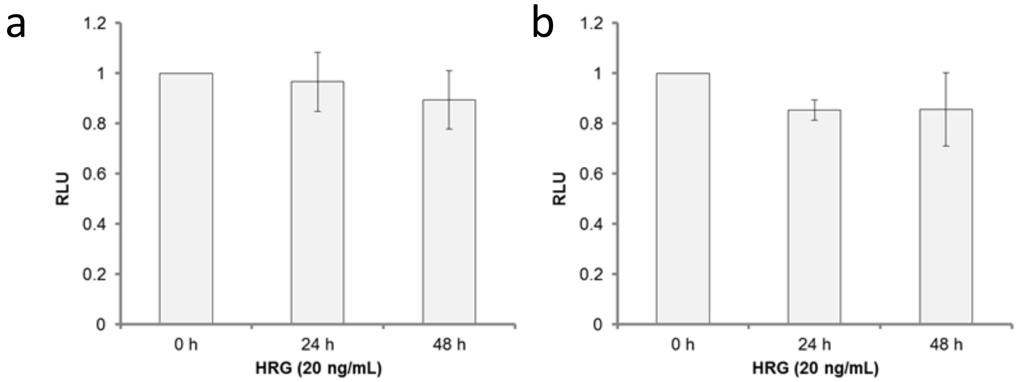

Figure 6.3 EcadMut-luc does not reduce E-cadherin expression.

Either a) SKBR3 or b) MCF7 cells were tranfected with EcadMut-luc and treated HRG. Neither showed a decrease in E-cadherin expression in response to HRG. Error bars indicate standard error of the mean.

To assess the specificity and efficacy of Co(III)-Ebox, its effects were compared to treatments with the untargeted Co(III) Schiff base (Co(III)-sb), Ebox double-stranded oligonucleotide (ds Ebox) and a mutated Co(III)-DNA conjugate (Co(III)-EboxMut) (Figure 6.2). The Ebox sequence in Co(III)-EboxMut has a 2-base pair substitution to diminish Snail protein binding. These three control derivatives were used to evaluate the specificity and efficacy of the binding interaction between Snail family TFs and Co(III)-Ebox (148, 155). In all cases, the HRG-induced decrease in E-cadherin expression was not inhibited compared to Co(III)-Ebox (Figure 6.2).

These results show that it is the cooperative effect between the sequence-specificity of the targeting Ebox oligonucleotide and the inhibitory efficacy of the Co(III)-sb that allows the potent inhibition of Snail family TFs by Co(III)-Ebox, corroborating previously observed results (148, 155). Specific inhibition of the Snail transcription factor is particularly desirable because reducing Snail activity has the potential to simultaneously prevent several aspects of HRG-induced invasiveness. This prediction stems from the centrality of Snail in the induction of EMT (138).

The extent of inhibition of E-cadherin repression by Co(III)-Ebox is not complete, as a decrease in E-cadherin expression is observed over time. However, the alleviation of E-cadherin repression is specific and significant. This is particularly important since Snail has a high turnover with a $t_{1/2}$ of less than 1 h (166, 167). Despite this high protein turnover, Co(III)-Ebox is capable of inhibiting the Snail family TF-mediated repression of E-cadherin expression over 48 h, emphasizing the potency of this conjugate.

To correlate the results observed in the luciferase assay experiments, expression of cytokeratin-18 (a Snail target gene) (158) was monitored in the presence and absence of Co(III)-Ebox using Western blot analysis. Similar to E-cadherin, the cytokeratin-18 promoter includes Ebox sequences and its expression is repressed by Snail (168). GAPDH was used as a loading control and for normalizing the cytokeratin-18 band intensities. 20 ng mL^{-1} HRG causes a time-dependent decrease of cytokeratin-18 expression in both SKBR3 and MCF7 cells (Figure 6.4). When the same cells were treated with Co(III)-Ebox, the HRG-induced decrease in cytokeratin-18 was not observed. The graphs showing the relative expression levels of cytokeratin-18 demonstrate that Co(III)-Ebox effectively inhibits the Snail-induced decrease in this epithelial marker (Figure 6.4).

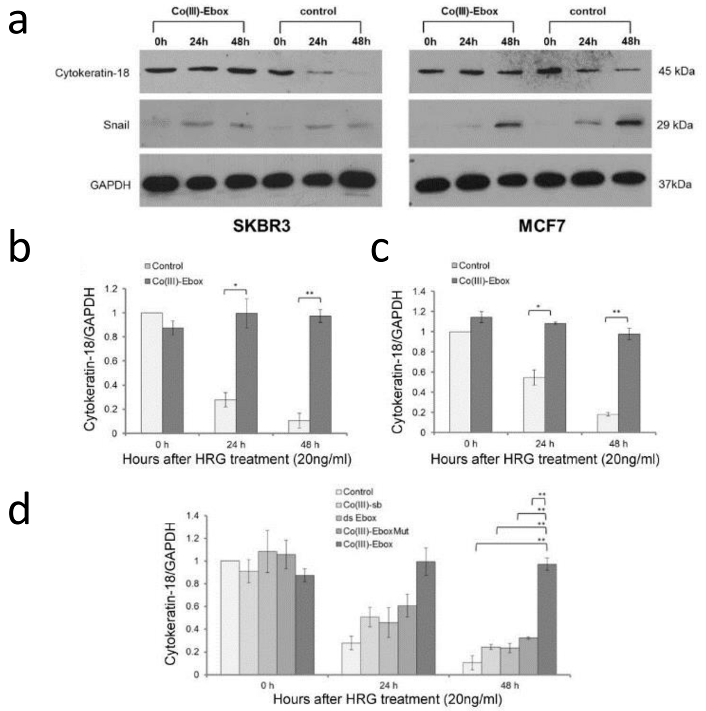

Figure 6.4 Co(III)-Ebox treatment alleviates the HRG-induced decrease in cytokeratin-18 expression in breast cancer cells.

a) Western blot films showing a time-dependent decrease in cytokeratin-18 in response to HRG in SKBR3 and MCF7 cells. This effect of HRG is alleviated when co-treated with Co(III)-Ebox. For both cell lines, the time-dependent increase in Snail in response to HRG is not affected by Co(III)-Ebox treatment. GAPDH was used as a loading control. Relative quantification of cytokeratin-18 expression in b) SKBR3 and c) MCF7 cells. Error bars indicate standard error of the mean. n = 3. Student's t-tests determined statistical significance from control treatment groups where *P<0.05 and **P<0.005. d) The effect of Co(III)-Ebox at inhibiting cytokeratin-18 expression is not observed when SKBR3 cells are treated with Co(III)-sb, ds Ebox or Co(III)-EboxMut. Error bars indicate standard error of the mean. n = 3. Student's t-tests determined statistical significance from control treatment groups where *P<0.05 and **P<0.005.

The expression levels of Snail were also probed using Western blot analysis. Since the target of Co(III)-Ebox is the Snail proteins themselves and not any of the upstream transducers, its expression is not expected to change in the presence or absence of Co(III)-Ebox. Snail expression increased in cells treated with HRG (Figure 6.4). However, the increase in Snail expression was unaltered by Co(III)-Ebox treatment. This shows that Co(III)-Ebox prevents the repression of E-cadherin and cytokeratin-18 through Snail inhibition and not through a reduction of Snail expression.

In a similar manner to the Ecad-luc experiment, the specificity and efficacy of Co(III)-Ebox was tested by comparing its effects to the control treatment with Co(III)-sb, ds Ebox oligonucleotide and Co(III)-EboxMut (Figure 6.4). In all cases HRG-induced decrease in cytokeratin-18 expression was found not to be alleviated which is in accordance with the Ecad-luc experiment. The requirement of having an Ebox sequence conjugated to the Co(III) complex in order to prevent cytokeratin-18 repression further emphasizes the highly specific and effective nature Snail inhibition by Co(III)-Ebox.

The Snail-induced decrease in expression of epithelial markers allows for HRG signaling to cause a corresponding increase in mesenchymal markers, several of which are associated with metastasis. The expression of fibronectin is an indicator of the invasive phenotype associated with Snail (169). For this reason, the ability of Co(III)-Ebox to inhibit the HRG-induced increase in expression of fibronectin was investigated. This was accomplished by immunofluorescence staining of SKBR3 and MCF7 cells. Cells that were treated with HRG showed red fluorescence corresponding to the Cy5-conjugated secondary antibody, indicative of the expression of fibronectin. In contrast, the cells that were treated with Co(III)-Ebox or those that were not treated with HRG did not display red fluorescence. This observation shows that Co(III)-Ebox is capable of inhibiting the downstream increase in fibronectin (Figure 6.5).

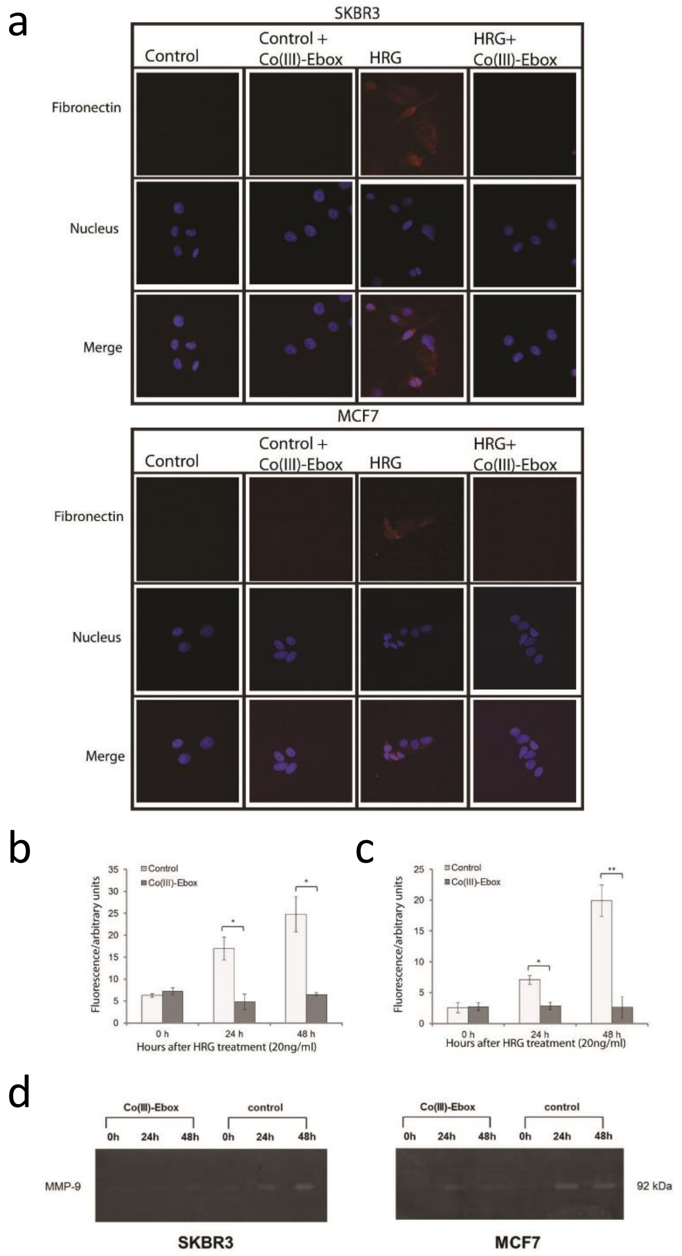

Figure 6.5 Co(III)-Ebox treatment alleviates the HRG-induced increase in mesenchymal marker expression in breast cancer cells.

a) Fluorescence microscope images of immunostained SKBR3 and MCF7 cells showing red (Cy5) fluorescence indicating fibronectin expression in response to HRG. No fibronectin-associated fluorescence is observed following co-treatment with Co(III)-Ebox. The Cy5 fluorescence is shown in grey scale for clarity. Scale bar represents 200 µm. Relative quantification of b) SKBR3 cells and c) MCF7 cells showing a time-dependent increase in fibronectin in response to HRG. This effect is alleviated when co-treated with Co(III)-Ebox. Error bars indicate standard error of the mean. n = 3. Student's t-tests determined statistical significance from control treatment groups where *P<0.05 and **P<0.005. d) Gel zymograms of SKBR3 and MCF7 cells showing a time-dependent increase in MMP-9 activity in response to HRG. The effects of HRG are alleviated by co-treatment with Co(III)-Ebox.

The level of fibronectin expression over time was compared by assessing the amount of red fluorescence corresponding to the Cy5-conjugated secondary antibody in a representative area of the image (Figure 6.5). 20 ng mL^{-1} HRG was shown to cause a time-dependent increase in fibronectin expression, but when the same cells were treated with Co(III)-Ebox, the HRG-induced increase in fibronectin was not observed. This result validates that Co(III)-Ebox effectively inhibits the HRG-induced increase in fibronectin, potentially preventing the capacity to invade surrounding tissue.

MMP-9 has been associated with increased metastatic potential due to its ability to degrade the extracellular matrix and promote angiogenesis (129). It has been shown that HRG increases MMP-9 protein, mRNA and activity levels in MCF7 and SKBR3 cells.(170) Furthermore in MDCK cells, Snail expression has been shown to directly increase expression of MMP-9 (171). Therefore the capacity of Co(III)-Ebox to inhibit HRG-induced expression of MMP-9 was explored. The activity of the enzyme was detected by gel zymography. Cells were grown in serum-free media and treated with vehicle or Co(III)-Ebox, followed by HRG. Fractions of the media were collected 0, 24 and 48 h after treatment and analyzed for MMP-9 activity. The cells treated with HRG exhibited a time-dependent increase in MMP-9 activity (Figure 6.5). However, this time-dependent increase in MMP-9 activity was inhibited when the same cells were treated with Co(III)-Ebox. This result further confirms that Co(III)-Ebox inhibition of Snail is capable of attenuating the invasiveness caused by HRG exposure.

Snail expression increases the invasive and migratory properties of cells, hence inhibition with Co(III)-Ebox is expected to prevent these processes. To confirm this, a functional scratch-wound assay was performed. Three scenarios were compared: cells grown with 1) no HRG, 2) HRG only and 3) both HRG and Co(III)-Ebox. Cells that were grown with no HRG showed little migration (Figure 6.6). However, cells treated with HRG showed much higher migration and the cells treated with Co(III)-Ebox were shown to migrate slower than HRG-treated cells but faster than cells grown without HRG. Further, the cells treated with HRG were observed to migrate with a mesenchymal phenotype, where the cells have a spindle-like appearance and migrate as individual cells rather than clumps of cells. In contrast, cells treated with both HRG and Co(III)-Ebox were observed to migrate less with a mesenchymal phenotype and more with an epithelial phenotype, further supporting that Co(III)-Ebox is capable of inhibiting the HRG-induced invasiveness. These results show that Co(III)-Ebox is capable of preventing the HRG-induced increase in migration by SKBR3 and MCF7 cells.

To corroborate the results of the scratch wound assay, transwell migration and invasion assays were performed (Figures 6.6). For these experiments, the migration and invasion of the mesenchymal-like MDA-MB-231 cells(72) were compared to that of the more epithelial SKBR3 and MCF7 cells (157). The transwell migration and invasion assays were both carried out using Corning® Transwell® inserts which have 8 μm pores in a polycarbonate membrane.

For the migration assays, the cells were plated in wells and treated with HRG alone or with HRG and Co(III)-Ebox. Serum was used as the chemo-attractant. For the invasion assay, basement membrane extract (BME) was plated into the inserts as an invasion substrate between the cells and chemo-attractant. It was found that MDA-MB-231 cells had the highest migratory/invasive ability followed by the SKBR3 cells and finally the MCF7 cells. For all cell lines (regardless of the availability of chemo-attractant), those treated with Co(III)-Ebox displayed less migration and invasion compared to the untreated cells. In particular, SKBR3 and MCF7 cells treated with Co(III)-Ebox migrated and invaded significantly less than the control in the presence of chemo-attractant. This demonstrates that Co(III)-Ebox is capable of inhibiting the migration and invasion of cells undergoing HRG-induced EMT.

To study the effect of Co(III)-Ebox in a more physiologically relevant environment, spheroids grown on a bed of agarose were used as a model of metastatic tumors (172). Attempts were made at growing spheroids from MDA-MB-231, SKBR3 and MCF7 cells, but only MCF7 cells successfully formed spheroids. Consequently, spheroid outgrowth experiments were carried out using MCF7 cells.

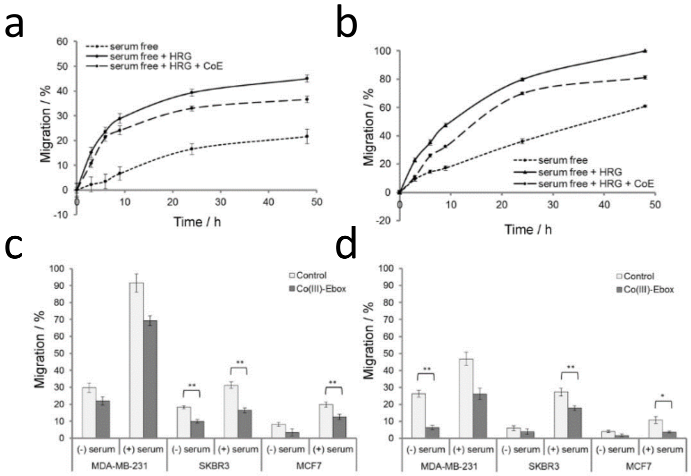

Figure 6.6 Co(III)-Ebox treatment alleviates the HRG-induced increase in breast cancer cell migration and invasion.

Graphs comparing the percent migration of a) SKBR3 and b) MCF7 cells in a scratch wound assay in the presence and absence of HRG, and with or without Co(III)-Ebox co-treatment. Error bars indicate standard error of the mean. n = 9. Comparison of c) the percent migration and d) the percent invasion of HRG-treated MDA-MB-231, SKBR3 and MCF7 cells with or without Co(III)-Ebox co-treatment, and with or without chemo-attractant (serum). Error bars indicate standard error of the mean. n = 3. Student's t-tests determined statistical significance between control and Co(III)-Ebox treatment where $^*P<0.05$ and $^{**}P<0.005$

MCF7 cells were seeded at a density of 2.5×10^4 cells in each well of a 96-well plate in serum-free media, allowed to settle overnight, then transfected with vehicle or 40 nM Co(III)-Ebox. After a 24 h incubation, the spheroids were treated with water or 20 ng mL^{-1} HRG. The cells were then allowed to aggregate for 5 days. Each spheroid was approximately 400 μm in diameter after the 5 day growth period. Figure 6.7 shows the transmittance images of spheroid morphology 8 days after the cells were plated on the bed of agarose. Cells grown without HRG formed clearly defined spheroids. However, cells that were treated with HRG grew misformed spheroids with an ill-defined perimeter. This is likely due to HRG causing the cells to acquire a more migratory and invasive phenotype, which causes the cells to break away from the spheroid. Spheroids that were treated with both HRG and Co(III)-Ebox presented the same morphology as the spheroids untreated with HRG, showing that Co(III)-Ebox is able to inhibit the effects of HRG, even in 3-dimensional culture.

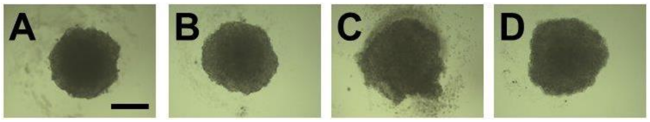

Figure 6.7 Transmittance images of MCF7 spheroids.

A) Treated with vehicle only, B) treated with Co(III)-Ebox only, C) treated with HRG only and D) treated with HRG and Co(III)-Ebox. Scale bar represents 200 μm.

To further assess the migratory and invasive behavior of spheroids, those grown in the same conditions as outlined in Figure 7 were embedded in BME, which mimics the extracellular matrix of cells. The purpose of this experiment was to observe the migration and invasion of cells originating from spheroids in a 3-dimensional setting, as this would be more representative of the actual behavior of cells metastasizing from tumors *in vivo*. To achieve efficient embedding in BME, the spheroids were harvested from the agarose bed and gently washed in PBS to remove any cell debris. They were then mixed with a BME solution in serum-free media supplemented with HRG, and the mixture was placed in a small well lined with pre-gelled BME such that the spheroids were 3-dimensionally suspended in BME upon gelling at 37°C. Images of the spheroids were obtained every 3 days, and the spheroids were fixed and immunostained for fibronectin after a total of 2 weeks.

Spheroids that were treated with vehicle showed migration and invasion of cells disseminating from the spheroids over a 12 day period (Figure 7A). During this time the spheroid was observed to invade the BME and occupy a larger volume. The spheroid became less compact, with clusters of cells migrating away from the main body of the spheroid. In contrast, the spheroid treated with Co(III)-Ebox did not invade the BME to the same extent (Figure 7B). Some alteration in the spheroid morphology was observed as shown by reorganization of its shape over time, but the volume occupied by the spheroids appeared to remain unchanged. The spheroids treated with Co(III)-Ebox remained dense, and no significant outgrowth or invasion into the BME was observed.

The visual observations of spheroid outgrowth were compared by measuring the spheroid density against the background using ImageJ software and determining the average diameter of the spheroids at each time point. The diameter of HRG-treated spheroids increased by approximately 200 μm after the 12 day period, indicating that the invasion of cells into the BME was extensive. In comparison, the diameter of the spheroids co-treated with Co(III)-Ebox remained virtually unchanged. This corroborates the visual observations that Co(III)-Ebox inhibits the invasion and migration of cells from spheroids. The difference in extent of outgrowth between the spheroids treated with HRG only and those that were co-treated with

Co(III)-Ebox highlight the efficacy of Co(III)-Ebox at inhibiting the migratory and invasive propensity of cells in a 3-dimensional setting.

The expression of fibronectin (a mesenchymal marker) was probed in spheroids embedded in BME by immunostaining (Figures 6.8). For the spheroids treated with vehicle only, the red fluorescence indicating fibronectin expression was found to be localized in the perimeter of the spheroids where the cells appear to be disseminating away from the body of the spheroid. This suggests that fibronectin is being expressed by the cells that are located at the outermost part of the spheroid where they are in direct contact with the BME. These cells are expected to be aggressively migrating and invading the matrix in response to HRG, which is in agreement with the high expression levels of fibronectin. In contrast, the spheroids that were treated with Co(III)-Ebox do not show any red fluorescence, indicating that there is no fibronectin expression. This result further supports the observations that the outgrowth of HRG-treated spheroids requires Snail activity and that Co(III)-Ebox is capable of inhibiting this process in 3-dimensions. To our knowledge, this is the first successful example of using spheroids to study inhibition of EMT using a 3-dimensional tumor model *in vitro*.

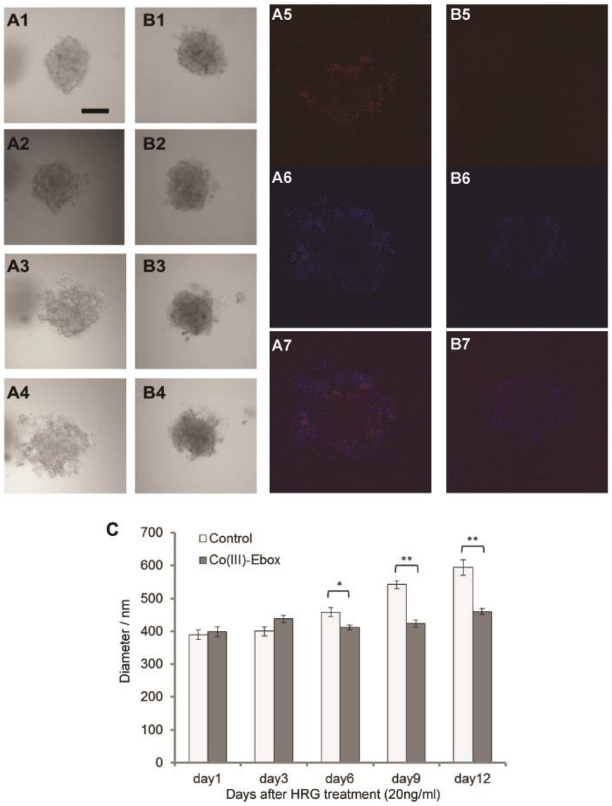

Figure 6.8 Co(III)-Ebox treatment alleviates the HRG-induced increase in breast cancer spheroid invasion.

MCF7 spheroids embedded in BME treated with A) HRG and B) HRG with Co(III)-Ebox were imaged at 1) 1 day, 2) 3 days, 3) 6 days and 4) 9 days. After 12 days, the spheroids were fixed and immunostained for fibronectin. Fluorescence images of 5) fibronectin Cy5), 6) nucleus DAPI) and 7) merge of 5) and 6). Scale bar represents 200 μm. C) Graph comparing the outgrowth of the spheroids as determined by measuring the diameter of the spheroids over time. Error bars indicate standard error of the mean. n = 3. Student's t-tests determined statistical significance between control and Co(III)-Ebox treatment where $*P<0.05$ and $**P<0.005$.

6.3 Conclusions

The results of the experiments described in this report show that Co(III)-Ebox is capable of inhibiting multiple aspects of Snail activity during HRG-induced EMT in SKBR3 and MCF7 breast cancer cells. Specifically, Co(III)-Ebox was observed to inhibit the Snail-induced decrease in epithelial markers such as E-cadherin and cytokeratin-18. Co(III)-Ebox was observed to inhibit the corresponding Snail-induced increase in mesenchymal markers such as fibronectin and MMP-9. Through Snail inhibition, Co(III)-Ebox was capable of delaying the invasive phenotype induced by HRG, both in 2- and 3-dimensional cell culture. In particular, the observed inhibition of spheroid invasion into BME in 3-dimension demonstrates that Co(III)-Ebox has significant promise in preventing tumor metastasis. The success of the agent *in vitro* warrants further experiments *in vivo* and in the clinic as an effective treatment for metastasis with a novel mode of action.

6.4 Materials and Methods

6.4.1 Chemical Synthesis

Co(III)-Ebox conjugate was prepared by methods previously described (148, 156). HRG was purchased from Sigma-Aldrich and used without further purification.

6.4.2 Cell Culture

SKBR3 (ATCC HTB-22), MCF7 (ATCC HTB-30) and MDA-MB-231 (ATCC HTB-26) human breast carcinoma cells were obtained from American Type Culture Collection (ATCC). SKBR3 and MCF7 are epithelial cells well known to be EMT-inducible following treatment with HRG.(157, 158, 173) MDA-MB-231 cells are mesenchymal-like cells used as a positive control.(174) Cells were maintained at 37 °C in a humidified environment with 5% CO_2 in complete media which is McCoy's 5A media supplemented with 10% (v/v) Fetal Bovine Serum (FBS) (Mediatech) for SKBR3, Eagle's Minimum Essential Media (EMEM) (Life Technologies) supplemented with 10% (v/v) FBS (Mediatech), 2 mM glutamine, 1 mM sodium pyruvate and 1 x MEM non-essential amino acids for MCF7 and MEM alpha supplemented with 10% (v/v) FBS, characterized (Mediatech), 2 mM L-glutamine, 1 mM sodium pyruvate, 1 x MEM non-essential amino acids and 1ug mL^{-1} insulin for MDA-MB-231. All experiments were performed in serum-free media to eliminate activation of the pathway by other signal transducers that may be present in serum (175).

Confocal Microscopy of Spheroids

Spheroids were prepared by plating 100 µl of a 2.5x10^{5} cells ml^{-1} single cell suspension of MCF7 cells onto 96 well plates coated in each well with 35 µL agarose (0.75% (w/v) in PBS).(172) Following incubation overnight, the spheroids were treated with 40 nM of Co(III)-Ebox complexed to Turbofect Transfection Reagent (Thermo Scientific). After 24 h, the cells were treated with 20 ng mL^{-1} of HRG and allowed to aggregate for 5 days without motion, resulting in the formation of a single spheroid per well.

On day 5, the spheroids were gently washed with PBS and embedded in 75µL of 0.25 µg µL^{-1} Cultrex® Basement Membrane Extract (BME)(Trevigen) made up in media with and without 20 ng mL^{-1} of HRG. The embedding was performed in a 2-well insert attached to a 35 mm microscopy µ-dish (iBidi) lined with 20 µL of 0.25 µg µL^{-1} Cultrex® BME. The embedded spheroids were imaged on day 1, and subsequently every 3 days over 12 days. At the end of the 12 days, the spheroids were fixed in 3.7% (w/v) formaldehyde solution in PBS for 2 h, then blocked overnight in 6% (w/v) BSA with 0.25% (v/v) TritonX-100 in PBS at room temperature. The wells were washed with 0.25% (v/v) TritonX-100 in PBS (3 x 10 mins) and incubated with anti-fibronectin mouse mAb (1:1000) (Thermo Scientific) in 3% (w/v) BSA with 0.25% (v/v) TritonX-100 in PBS overnight at room temperature. The wells were washed in PBS (3 x 10 mins) and incubated with Cy5-conjugated secondary antibody (1:500) in 3% (w/v) BSA with 0.25% (v/v) TritonX-100 in PBS overnight at room temperature. The wells were washed with 0.25% (v/v) TritonX-100 in PBS (3 x 10 mins) and incubated with DAPI (300 nM) with 0.25% (v/v) TritonX-100 in PBS overnight at room temperature and imaged the following day.

Confocal fluorescence microscopy was performed using a LSM 510 Inverted Confocal Scanning Microscope (Zeiss) and an EC Plan-Neofluar 10x0.30 objective lens. Confocal images were acquired using a 700 nm Mai-Tai Ti-Sapphire crystal laser (Spectra-Physics), a 480 nm LGK7812ML4 Ar laser (Lasos) and a 633 nm LGK7628-1 He/Ne laser. The emission ranges were 390-465 nm, 500-530 nm and 650-710 nm, respectively. A scan rate of 1.6 µs/pixel was used for all images and an average of 4 scans per image were collected. Z-stack images were collected with increments of 15 µm. An incubator chamber (PeCon) was used to maintain the temperature at 37 °C during imaging. At least 3 spheroids were imaged on each occasion and the experiment was repeated on at least 3 separate occasions. Images shown are a representative replicate.

Relative quantification of the spheroid outgrowth was carried out using ImageJ (NIH) by drawing an 800 µm line through the center of the spheroid in the Z-stack transmittance image and measuring the integrated density where the spheroid has the largest diameter. The diameter of the spheroid was determined from the plotted profile of the line. This procedure was repeated 16 times, rotating the line around the spheroid at approximately equal angle intervals and the measured diameters averaged. Measurements were taken from at least six different spheroids in each treatment group. Statistical analysis was performed on the means using the Student's t-test where $^{*}P < 0.05$ and $^{**}P < 0.005$.

Reporter Gene Assays

Luciferase reporter gene constructs containing wild-type E-cadherin promoter sequences were a gift from E. Fearon (164). The E-cadherin promoter region containing 3 Eboxes (from 2108 to +125 of the endogenous E-cadherin gene) were cloned into pGL2-Basic upstream of firefly Luciferase (Ecad-luc). Ebox elements in the E-cadherin promoter in Ecad-luc were mutated from 5'-CAGGTG-3' to 5'-AAGGTA-3' in EcadMut-luc. To examine the repression of the E-cadherin reporter gene construct by endogenous and EMT-induced Snail, 1 x 10^5 cells were plated in each well of a 24-well plate and allowed to adhere overnight. The media was replaced with serum-free media, and 200 ng of the E-cadherin construct (Ecad-luc or EcadMut-luc), 50 ng of the Renilla luciferase construct as a control and 40 nM of the experimental compound were transfected per well. The experimental derivatives included the Co(III) Schiff base complex (Co(III)-sb), the Ebox double-stranded oligonucleotide (ds Ebox), the Co(III)-DNA conjugate with 2-base pair substitution in the Ebox region (Co(III)-EboxMut) and the Co(III)-DNA conjugate targeted to Snail family TFs (Co(III)-Ebox). Cell lines were transfected using Turbofect Transfection Reagent (Thermo Scientific) according to the manufacturer's protocol. In each experiment the total DNA transfected in each well was equalized by the addition of noncoding DNA as pCS2+ empty vector to samples that do not contain experimental compound. Following transfection, the SKBR3 or MCF7 cells were treated with 20 ng mL^{-1} of HRG for 24 or 48 h, then cell extracts were prepared using Passive lysis buffer (Promega).

Firefly luciferase and Renilla luciferase activity were determined using the Dual-Luciferase Reporter assay kit (Promega) on a GloMax 96 Microplate Luminometer (Promega). The results were normalized by dividing firefly luciferase activity by Renilla luciferase activity and reported as fold inductions of the vehicle control. These values were averaged over three replicates and reported with the standard error. Statistical analysis was performed on the means using the Student's t-test where $*P<0.05$ and $**P<0.005$.

Western Blot Analysis

SKBR3 or MCF7 cells were plated at a density of 2.5×10^5 cells in each well of a 6-well plate and allowed to adhere overnight. The media was replaced with serum-free media, and 40 nM of the experimental compound [Co(III)-sb, ds Ebox, Co(III)-EboxMut and Co(III)-Ebox] were transfected per well using Turbofect Transfection Reagent (Thermo Scientific) according to the manufacturer's protocol. Following transfection, the cells were treated with 20 ng mL^{-1} HRG for 24 or 48 h, and cell extracts were prepared using a cell lysis buffer (50 mM Tris-HCl (pH=7.4), 1% (v/v) NP40, 0.25% (w/v) sodium deoxychlorate, 100 mM NaCl, 1 mM EGTA and 1 mM NaF). Samples were denatured in Laemmli buffer and resolved by SDS-PAGE on a 10 % (w/v) acrylamide gel. Each lane of the gel was loaded with 10 µg of total protein. After transferring to a nitrocellulose membrane (Whatman), specific proteins were detected using anti-cytokeratin-18 (Ab-2) mouse mAb (1:200) (Calbiochem), anti-Snai1 rabbit mAb (1:1000) (Cell Signaling Technologies) and anti-GAPDH rabbit mAb (1:500) (Sigma-Aldrich). ECL anti-rabbit IgG HRP-linked antibody (1:3000) (Amersham) and anti-mouse IgG (H+L) HRP conjugate (1:3000) (Promega) were used as secondary antibodies.

The immunoreactive bands were detected using a SuperSignal West Pico Chemiluminescent Substrate (Pierce). Band images were obtained by using ChemiDoc XRS+ (Bio-Rad) and band intensity analyzed by ImageJ software (NIH). Images presented are a representative replicate of triplicate samples. Band intensity values were normalized to the GAPDH signal in each lane. The percentage of protein expressed is the normalized intensity of each treatment divided by the normalized intensity of the untreated lane. These values were averaged over three replicates and reported with the standard error. Statistical analysis was performed on the means using Student's t-test where $*P<0.05$ and $**P<0.005$.

Immunofluorescence

SKBR3 or MCF7 cells were plated at a density of 5×10^5 cells in each well of a 6-well plate onto glass coverslips and allowed to adhere overnight. 40 nM of Co(III)-Ebox was transfected per well using Turbofect Transfection Reagent (Thermo Scientific) according to the manufacturer's protocol. Following transfection, the cells were treated with 20 ng mL^{-1} of HRG for 24 or 48 h, and fixed at 4 °C for 10 mins using 3.7% (w/v) paraformaldehyde in PBS. The cells were then blocked for 1 h in 6% (w/v) BSA with 0.25% (v/v) TritonX-100 in PBS. The coverslips were washed in PBS (3 x 10 mins) and incubated with anti-fibronectin mouse mAb (1:1000) (Thermo Scientific) in 3% (w/v) BSA with 0.25% (v/v) TritonX-100 in PBS for 1 h. The coverslips were washed in PBS (3 x 10 mins) and incubated with Cy5-conjugated anti-mouse secondary antibody (1:500) in 3% (w/v) BSA with 0.25% (v/v) TritonX-100 in PBS for 1 h. The coverslips were washed in PBS (3 x 10 mins) and mounted onto a glass microscopy slide using ProLong Gold antifade agent with DAPI (Invitrogen) and allowed to cure overnight.

Cells were imaged on a DeltaVision Deconvolution Microscope (Applied Precision) equipped with a Coolpix HQ Camera (Nikon) using a PlanApo N *60x/1.45 Oil* objective. The images were deconvoluted and analyzed using the DeltaVisionSoftWoRx™ software. At least 3 images were taken per slide and repeated on at least 3 separate occasions. Images presented are a representative replicate of triplicate samples. Relative quantification of the fluorescence intensity was carried out using ImageJ by drawing a 20 μm diameter circle over a representative portion of the image and measuring the integrated fluorescence intensity. Background fluorescence was measured in areas of the image that did not have cells and subtracted from the measured integrated fluorescence intensity.(176) Measurements were taken from at least five different images in each treatment group. Statistical analysis was performed on the means using the Student's t-test where $*P<0.05$ and $**P<0.005$.

Zymography

SKBR3 and MCF7 cells were plated in complete media at a density of 2 x 10^5 cells in each well of a 6-well plate and allowed to adhere overnight. The media was then replaced with serum free media. 40 nM of Co(III)-Ebox was transfected per well using Turbofect Transfection Reagent (Thermo Scientific) according to the manufacturer's protocol and the cells were subsequently treated with 20 ng mL^{-1} HRG in each well. Aliquots of the new media were taken after 0, 24 and 48 h. Samples were denatured and resolved on a 1% (w/v) gelatin zymography gel cast in acrylamide. Each lane of the gel was loaded with 10 µg of total protein. The SeeBlue® Plus2 Pre-Stained Standard (Invitrogen) was used as a mass marker. The gel was placed in renaturing buffer (50 mM Tris-base, 5 mM $CaCl_2$, 1 µM $ZnCl_2$, 2.5 % (v/v) TritonX-100, pH=7.4) for 1 h at room temperature then placed in developing buffer (50 mM Tris-base, 5 mM $CaCl_2$, 1 µM $ZnCl_2$, 0.01% (w/v) NaN_3, pH = 7.4) at 37 °C for 12h. The gel was stained for 30 mins using a Coumassie Blue stain (0.5 g Coumassie Brilliant Blue R250 dissolved in 45 mL MeOH, 45 mL H_2O and 10 mL glacial acetic acid) then de-stained with 30% (v/v) acetic acid and 10% (v/v) ethanol in water for 1 h.

Scratch wound assay

SKBR3 and MCF7 cells were plated at a density of 2 x 10^5 cells into each well of a 48-well plate and allowed to adhere overnight. The media was replaced with serum free media, serum free media containing 20 ng mL^{-1} of HRG or serum free media containing 20 ng mL^{-1} of HRG and 40 nM of Co(III)-Ebox complexed to Turbofect Transfection Reagent (Thermo Scientific). The cells were allowed to grow to confluency over 2 days, at which point a scratch wound was created in the cell monolayer using a 2 µL pipette tip. A razor was used to mark the underside of the plate perpendicular to the scratch wound as a reference point for imaging. Images of the scratch wound were obtained every 3 h for the first 9 h, then at 24 and 48 h on a Invertoskop 40C microscope (Zeiss) equipped with a ProgRes®C3 camera (Jenoptik) using a CP-ACHROMAT 5x/0.12 objective. The data was processed by measuring the width of the scratch wound at 10 different places and representing as a percentage of the width at t=0. Experiments were conducted in triplicate on at least three separate occasions. These values were averaged and reported with the standard error.

Transwell Migration and Invasion Assays

The transwell migration and invasion assays were performed using the Corning® Transwell® 96 well permeable supports according to the manufacturer's instructions. SKBR3, MCF7 and MDA-MB-231 cells were plated in a T75 flask and allowed to grow to ~50% confluency. The media was changed to serum-free media, and the cells were allowed to grow overnight, then removed from the flask using Accutase®. The cells were counted using a Guava easyCyte® flow cytometer (Millipore) and 5 x 10^4 cells were plated in each well of the Corning® Transwell® 96 well permeable support insert in 50 μL serum-free media with or without 20 ng mL^{-1} HRG and/or 40 nM of Co(III)-Ebox complexed to Turbofect Transfection Reagent (Thermo Scientific). For invasion assays, 35 μL of 0.25 μg $μL^{-1}$ Cultrex® Basement Membrane Extract (Trevigen) diluted 1:4 with appropriate media was plated in each well of the insert and allowed to gel at 37 °C prior to plating cells. 150 μL of complete or serum-free media was placed in each well of the receiver plate. The cells were allowed to incubate for 48 h, after which the inserts and receiver wells were gently washed with PBS. The cells on the underside of the insert were dissociated with 2 mM Calcein-AM (AnaSpec) in Accutase®, and the fluorescence emission at 520 nm in each well was measured using a Synergy 4 microplate reader (BioTek), exciting at 485 nm. These values were averaged over three replicates and reported with the standard error. Statistical analysis was performed on the means using the Student's t-test where $^{*}P<0.05$ and $^{**}P<0.005$.

References Cited

1. Wahl RL, Quint LE, Greenough RL, Meyer CR, White RI, Orringer MB. Staging of mediastinal non-small cell lung cancer with FDG PET, CT, and fusion images: preliminary prospective evaluation. Radiology. 1994;191(2):371-7. doi: doi:10.1148/radiology.191.2.8153308. PubMed PMID: 8153308.

2. Nakamoto Y, Cohade C, Tatsumi M, Hammoud D, Wahl RL. CT Appearance of Bone Metastases Detected with FDG PET as Part of the Same PET/CT Examination. Radiology. 2005;237(2):627-34. doi: doi:10.1148/radiol.2372031994. PubMed PMID: 16244271.

3. Boswell CA, Brechbiel MW. Development of Radioimmunotherapeutic and Diagnostic Antibodies: An Inside-Out View. Nuclear medicine and biology. 2007;34(7):757-78. doi: 10.1016/j.nucmedbio.2007.04.001. PubMed PMID: PMC2212602.

4. Willmann JK, van Bruggen N, Dinkelborg LM, Gambhir SS. Molecular imaging in drug development. Nat Rev Drug Discov. 2008;7(7):591-607. doi: http://www.nature.com/nrd/journal/v7/n7/suppinfo/nrd2290_S1.html.

5. Klunk WE, Engler H, Nordberg A, Wang Y, Blomqvist G, Holt DP, Bergström M, Savitcheva I, Huang G-F, Estrada S, Ausén B, Debnath ML, Barletta J, Price JC, Sandell J, Lopresti BJ, Wall A, Koivisto P, Antoni G, Mathis CA, Långström B. Imaging brain amyloid in Alzheimer's disease with Pittsburgh Compound-B. Annals of Neurology. 2004;55(3):306-19. doi: 10.1002/ana.20009.

6. Caravan P, Ellison JJ, McMurry TJ, Lauffer RB. Gadolinium(III) Chelates as MRI Contrast Agents: Structure, Dynamics, and Applications. Chemical Reviews. 1999;99(9):2293-352. doi: 10.1021/cr980440x.

7. Elliott JT, Dsouza AV, Davis SC, Olson JD, Paulsen KD, Roberts DW, Pogue BW. Review of fluorescence guided surgery visualization and overlay techniques. Biomed Opt Express. 2015;6(10):3765-82. doi: 10.1364/BOE.6.003765.

8. James ML, Gambhir SS. A Molecular Imaging Primer: Modalities, Imaging Agents, and Applications. Physiological Reviews. 2012;92(2):897-965. doi: 10.1152/physrev.00049.2010.

9. Moses WW. Fundamental Limits of Spatial Resolution in PET. Nuclear instruments & methods in physics research Section A, Accelerators, spectrometers, detectors and associated equipment. 2011;648 Supplement 1:S236-S40. doi: 10.1016/j.nima.2010.11.092. PubMed PMID: PMC3144741.

10. Bal H, Guerin L, Casey ME, Conti M, Eriksson L, Michel C, Fanti S, Pettinato C, Adler S, Choyke P. Improving PET spatial resolution and detectability for prostate cancer imaging. Physics in Medicine and Biology. 2014;59(15):4411.

11. Samuel E, Radoslaw M, Vincent K, Stefaan V, Roel Van H. DigiPET: sub-millimeter spatial resolution small-animal PET imaging using thin monolithic scintillators. Physics in Medicine and Biology. 2014;59(13):3405.

12. Jiang L, Tu Y, Shi H, Cheng Z. PET probes beyond (18)F-FDG. Journal of Biomedical Research. 2014;28(6):435-46. doi: 10.7555/JBR.28.20130196. PubMed PMID: PMC4250522.

13. Vander Heiden MG, Cantley LC, Thompson CB. Understanding the Warburg Effect: The Metabolic Requirements of Cell Proliferation. Science (New York, NY). 2009;324(5930):1029-33. doi: 10.1126/science.1160809. PubMed PMID: PMC2849637.

14. Kubota K, Matsuzawa T, Ito M, Ito K, Fujiwara T, Abe Y, Yoshioka S, Fukuda H, Hatazawa J, Iwata R, Watanuki S, Ido T. Lung Tumor Imaging by Positron Emission Tomography Using C-11 L-Methionine. Journal of Nuclear Medicine. 1985;26(1):37-42.

15. Piert M, Machulla H-J, Picchio M, Reischl G, Ziegler S, Kumar P, Wester H-J, Beck R, McEwan AJB, Wiebe LI, Schwaiger M. Hypoxia-Specific Tumor Imaging with 18F-Fluoroazomycin Arabinoside. Journal of Nuclear Medicine. 2005;46(1):106-13.

16. Yagle KJ, Eary JF, Tait JF, Grierson JR, Link JM, Lewellen B, Gibson DF, Krohn KA. Evaluation of 18F-Annexin V as a PET Imaging Agent in an Animal Model of Apoptosis. Journal of Nuclear Medicine. 2005;46(4):658-66.

17. Chin FT, Shen B, Liu S, Berganos RA, Chang E, Mittra E, Chen X, Gambhir SS. First Experience with Clinical-Grade [18F]FPP(RGD)2: An Automated Multi-step Radiosynthesis for Clinical PET Studies.

Molecular imaging and biology : MIB : the official publication of the Academy of Molecular Imaging. 2012;14(1):88-95. doi: 10.1007/s11307-011-0477-3.

18. Wadas TJ, Wong EH, Weisman GR, Anderson CJ. Coordinating Radiometals of Copper, Gallium, Indium, Yttrium and Zirconium for PET and SPECT Imaging of Disease. Chemical reviews. 2010;110(5):2858-902. doi: 10.1021/cr900325h. PubMed PMID: PMC2874951.

19. van der Have F, Vastenhouw B, Ramakers RM, Branderhorst W, Krah JO, Ji C, Staelens SG, Beekman FJ. U-SPECT-II: An Ultra-High-Resolution Device for Molecular Small-Animal Imaging. Journal of Nuclear Medicine. 2009;50(4):599-605. doi: 10.2967/jnumed.108.056606.

20. Jayson GC, Zweit J, Jackson A, Mulatero C, Julyan P, Ranson M, Broughton L, Wagstaff J, Hakannson L, Groenewegen G, Bailey J, Smith N, Hastings D, Lawrance J, Haroon H, Ward T, McGown AT, Tang M, Levitt D, Marreaud S, Lehmann FF, Herold M, Zwierzina H, Research FtEOf, Group ToCBTD. Molecular Imaging and Biological Evaluation of HuMV833 Anti-VEGF Antibody: Implications for Trial Design of Antiangiogenic Antibodies. Journal of the National Cancer Institute. 2002;94(19):1484-93. doi: 10.1093/jnci/94.19.1484.

21. Belhocine T, Steinmetz N, Hustinx R, Bartsch P, Jerusalem G, Seidel L, Rigo P, Green A. <div xmlns="http://www.w3.org/1999/xhtml">Increased Uptake of the Apoptosis-imaging Agent ^{99m}Tc Recombinant Human Annexin V in Human Tumors after One Course of Chemotherapy as a Predictor of Tumor Response and Patient Prognosis</div>. Clinical Cancer Research. 2002;8(9):2766-74.

22. Martins AF, Morfin J-F, Kubíčková A, Kubíček V, Buron F, Suzenet F, Salerno M, Lazar AN, Duyckaerts C, Arlicot N, Guilloteau D, Geraldes CFGC, Tóth É. PiB-Conjugated, Metal-Based Imaging Probes: Multimodal Approaches for the Visualization of β-Amyloid Plaques. ACS Medicinal Chemistry Letters. 2013;4(5):436-40. doi: 10.1021/ml400042w.

23. Liu Z, Ma T, Liu H, Jin Z, Sun X, Zhao H, Shi J, Jia B, Li F, Wang F. 177Lu-Labeled Antibodies for EGFR-Targeted SPECT/CT Imaging and Radioimmunotherapy in a Preclinical Head and Neck Carcinoma Model. Molecular Pharmaceutics. 2014;11(3):800-7. doi: 10.1021/mp4005047.

24. Dzik-Jurasz ASK. Molecular imaging in vivo: an introduction. The British Journal of Radiology. 2003;76(suppl_2):S98-S109. doi: doi:10.1259/bjr/25833499. PubMed PMID: 15572339.

25. Ntziachristos V, Bremer C, Weissleder R. Fluorescence imaging with near-infrared light: new technological advances that enable in vivo molecular imaging. European Radiology. 2003;13(1):195-208. doi: 10.1007/s00330-002-1524-x.

26. Wang LV, Wu H-i. Biomedical optics: principles and imaging: John Wiley & Sons; 2012.

27. Hong G, Lee JC, Robinson JT, Raaz U, Xie L, Huang NF, Cooke JP, Dai H. Multifunctional in vivo vascular imaging using near-infrared II fluorescence. Nat Med. 2012;18(12):1841-6. doi: http://www.nature.com/nm/journal/v18/n12/abs/nm.2995.html#supplementary-information.

28. Wallingford VH. The development of organic iodine compounds as X-ray contrast media. Journal of the American Pharmaceutical Association. 1953;42(12):721-8. doi: 10.1002/jps.3030421206.

29. Hainfeld JF, Slatkin DN, Focella TM, Smilowitz HM. Gold nanoparticles: a new X-ray contrast agent. The British Journal of Radiology. 2006;79(939):248-53. doi: doi:10.1259/bjr/13169882. PubMed PMID: 16498039.

30. Massey LA, Miranda MA, Zrinzo L, Al-Helli O, Parkes HG, Thornton JS, So PW, White MJ, Mancini L, Strand C, Holton JL, Hariz MI, Lees AJ, Revesz T, Yousry TA. High resolution MR anatomy of the subthalamic nucleus: Imaging at 9.4 T with histological validation. NeuroImage. 2012;59(3):2035-44. doi: http://dx.doi.org/10.1016/j.neuroimage.2011.10.016.

31. Rudin M, Weissleder R. Molecular imaging in drug discovery and development. Nature reviews Drug discovery. 2003;2(2):123-31. doi: 10.1038/nrd1007. PubMed PMID: 12563303.

32. Johnson GA, Calabrese E, Badea A, Paxinos G, Watson C. A multidimensional magnetic resonance histology atlas of the Wistar rat brain. NeuroImage. 2012;62(3):1848-56. doi: http://dx.doi.org/10.1016/j.neuroimage.2012.05.041.

33. Pierre VC, Allen MJ, Caravan P. Contrast agents for MRI: 30+ years and where are we going? JBIC Journal of Biological Inorganic Chemistry. 2014;19(2):127-31. doi: 10.1007/s00775-013-1074-5.

34. Kubben PL, ter Meulen KJ, Schijns OEMG, ter Laak-Poort MP, van Overbeeke JJ, Santbrink Hv. Intraoperative MRI-guided resection of glioblastoma multiforme: a systematic review. The Lancet Oncology. 2011;12(11):1062-70. doi: http://dx.doi.org/10.1016/S1470-2045(11)70130-9.

35. Swan JS, Carroll TJ, Kennell TW, Heisey DM, Korosec FR, Frayne R, Mistretta CA, Grist TM. Time-resolved Three-dimensional Contrast-enhanced MR Angiography of the Peripheral Vessels. Radiology. 2002;225(1):43-52. doi: doi:10.1148/radiol.2251011292. PubMed PMID: 12354982.

36. Moats RA, Fraser SE, Meade TJ. A “Smart” Magnetic Resonance Imaging Agent That Reports on Specific Enzymatic Activity. Angewandte Chemie (English Edition). 1997;36(7):726-8. doi: 10.1002/anie.199707261.

37. Giardiello M, Lowe MP, Botta M. An esterase-activated magnetic resonance contrast agent. Chemical Communications. 2007(39):4044-6. doi: 10.1039/B711989E.

38. Tu C, Osborne EA, Louie AY. Synthesis and characterization of a redox- and light-sensitive MRI contrast agent. Tetrahedron. 2009;65(7):1241. doi: 10.1016/j.tet.2008.12.020. PubMed PMID: PMC2678739.

39. Geninatti Crich S, Alberti D, Szabo I, Aime S, Djanashvili K. MRI visualization of melanoma cells by targeting overexpressed sialic acid with a Gd(III)-dota-en-pba imaging reporter. Angewandte Chemie (English Edition). 2013;52(4):1161-4. doi: 10.1002/anie.201207131. PubMed PMID: 23225599.

40. Vymazal J, Spuentrup E, Cardenas-Molina G, Wiethoff AJ, Hartmann MG, Caravan P, Parsons ECJ. Thrombus Imaging With Fibrin-Specific Gadolinium-Based MR Contrast Agent EP-2104R: Results of a Phase II Clinical Study of Feasibility. Investigative Radiology. 2009;44(11):697-704.

41. Li W-h, Parigi G, Fragai M, Luchinat C, Meade TJ. Mechanistic Studies of a Calcium-Dependent MRI Contrast Agent. Inorganic Chemistry. 2002;41(15):4018-24. doi: 10.1021/ic0200390.

42. De León-Rodríguez LM, Lubag A, Udugamasooriya DG, Proneth B, Brekken RA, Sun X, Kodadek T, Dean Sherry A. MRI Detection of VEGFR2 in Vivo Using a Low Molecular Weight Peptoid−(Gd)8-Dendron for Targeting. Journal of the American Chemical Society. 2010;132(37):12829-31. doi: 10.1021/ja105563a.

43. Carney CE, MacRenaris KW, Mastarone DJ, Kasjanski DR, Hung AH, Meade TJ. Cell Labeling via Membrane-Anchored Lipophilic MR Contrast Agents. Bioconjugate Chemistry. 2014;25(5):945-54. doi: 10.1021/bc500083t.

44. Nicholls FJ, Rotz MW, Ghuman H, MacRenaris KW, Meade TJ, Modo M. DNA–gadolinium–gold nanoparticles for in vivo T1 MR imaging of transplanted human neural stem cells. Biomaterials. 2016;77:291-306. doi: http://dx.doi.org/10.1016/j.biomaterials.2015.11.021.

45. Hung AH, Holbrook RJ, Rotz MW, Glasscock CJ, Mansukhani ND, MacRenaris KW, Manus LM, Duch MC, Dam KT, Hersam MC, Meade TJ. Graphene Oxide Enhances Cellular Delivery of Hydrophilic Small Molecules by Co-incubation. ACS Nano. 2014;8(10):10168-77. doi: 10.1021/nn502986e.

46. Preslar AT, Parigi G, McClendon MT, Sefick SS, Moyer TJ, Haney CR, Waters EA, MacRenaris KW, Luchinat C, Stupp SI, Meade TJ. Gd(III)-Labeled Peptide Nanofibers for Reporting on Biomaterial Localization in Vivo. ACS Nano. 2014;8(7):7325-32. doi: 10.1021/nn502393u.

47. Viswanathan S, Kovacs Z, Green KN, Ratnakar SJ, Sherry AD. Alternatives to Gadolinium-based MRI Metal Chelates. Chemical reviews. 2010;110(5):2960-3018. doi: 10.1021/cr900284a. PubMed PMID: PMC2874212.

48. Manus LM, Strauch RC, Hung AH, Eckermann AL, Meade TJ. Analytical Methods for Characterizing Magnetic Resonance Probes. Analytical chemistry. 2012;84(15):6278-87. doi: 10.1021/ac300527z. PubMed PMID: PMC3418482.

49. Lauffer RB, Parmelee DJ, Dunham SU, Ouellet HS, Dolan RP, Witte S, McMurry TJ, Walovitch RC. MS-325: albumin-targeted contrast agent for MR angiography. Radiology. 1998;207(2):529-38. doi: doi:10.1148/radiology.207.2.9577506. PubMed PMID: 9577506.

50. Strauch RC, Mastarone DJ, Sukerkar PA, Song Y, Ipsaro JJ, Meade TJ. Reporter protein-targeted probes for magnetic resonance imaging. Journal of the American Chemical Society. 2011;133(41):16346-9. Epub 2011/09/29. doi: 10.1021/ja206134b. PubMed PMID: 21942425; PubMed Central PMCID: PMCPmc3203639.

51. Moriggi L, Cannizzo C, Dumas E, Mayer CR, Ulianov A, Helm L. Gold Nanoparticles Functionalized with Gadolinium Chelates as High-Relaxivity MRI Contrast Agents. Journal of the American Chemical Society. 2009;131(31):10828-9. doi: 10.1021/ja904094t.

52. Louie AY, Huber MM, Ahrens ET, Rothbacher U, Moats R, Jacobs RE, Fraser SE, Meade TJ. In vivo visualization of gene expression using magnetic resonance imaging. Nature Biotechnology. 2000;18(3):321-5.

53. Siriwardena-Mahanama BN, Allen MJ. Strategies for Optimizing Water-Exchange Rates of Lanthanide-Based Contrast Agents for Magnetic Resonance Imaging. Molecules (Basel, Switzerland). 2013;18(8):9352-81. doi: 10.3390/molecules18089352. PubMed PMID: PMC3775326.

54. Sukerkar PA, MacRenaris KW, Meade TJ, Burdette JE. A Steroid-Conjugated Magnetic Resonance Probe Enhances Contrast in Progesterone Receptor Expressing Organs and Tumors in Vivo. Molecular Pharmaceutics. 2011;8(4):1390-400. doi: 10.1021/mp200219e.

55. Ahrens ET, Rothbächer U, Jacobs RE, Fraser SE. A model for MRI contrast enhancement using T1 agents. Proceedings of the National Academy of Sciences, USA. 1998;95(15):8443-8.

56. Hanaoka K, Lubag AJ, Castillo-Muzquiz A, Kodadek T, Sherry AD. The detection limit of a Gd3+-based T1 agent is substantially reduced when targeted to a protein microdomain. Magnetic resonance imaging. 2008;26(5):608-17. doi: 10.1016/j.mri.2007.11.002. PubMed PMID: 18234462; PubMed Central PMCID: PMC2483407.

57. Schwanhausser B, Busse D, Li N, Dittmar G, Schuchhardt J, Wolf J, Chen W, Selbach M. Global quantification of mammalian gene expression control. Nature. 2011;473(7347):337-42. doi: http://www.nature.com/nature/journal/v473/n7347/abs/10.1038-nature10098-unlocked.html#supplementary-information.

58. Albanese A, Tang PS, Chan WCW. The Effect of Nanoparticle Size, Shape, and Surface Chemistry on Biological Systems. Annual Review of Biomedical Engineering. 2012;14(1):1-16. doi: doi:10.1146/annurev-bioeng-071811-150124. PubMed PMID: 22524388.

59. Harney AS, Meade TJ. Molecular imaging of in vivo gene expression. Future medicinal chemistry. 2010;2(3):503-19. doi: 10.4155/fmc.09.168. PubMed PMID: PMC4507573.

60. Major JL, Meade TJ. Bioresponsive, Cell-Penetrating, and Multimeric MR Contrast Agents. Accounts of Chemical Research. 2009;42(7):893-903. doi: 10.1021/ar800245h.

61. Kalber TL, Kamaly N, So PW, Pugh JA, Bunch J, McLeod CW, Jorgensen MR, Miller AD, Bell JD. A low molecular weight folate receptor targeted contrast agent for magnetic resonance tumor imaging. Molecular imaging and biology : MIB : the official publication of the Academy of Molecular Imaging. 2011;13(4):653-62. doi: 10.1007/s11307-010-0400-3. PubMed PMID: 20809208.

62. Heffern MC, Matosziuk LM, Meade TJ. Lanthanide Probes for Bioresponsive Imaging. Chemical Reviews. 2014;114(8):4496-539. doi: 10.1021/cr400477t.

63. Banerjee SR, Ngen EJ, Rotz MW, Kakkad S, Lisok A, Pracitto R, Pullambhatla M, Chen Z, Shah T, Artemov D, Meade TJ, Bhujwalla ZM, Pomper MG. Synthesis and Evaluation of GdIII-Based Magnetic Resonance Contrast Agents for Molecular Imaging of Prostate-Specific Membrane Antigen. Angewandte Chemie International Edition. 2015;54(37):10778-82. doi: 10.1002/anie.201503417.

64. Cohen B, Dafni H, Meir G, Harmelin A, Neeman M. Ferritin as an endogenous MRI reporter for noninvasive imaging of gene expression in C6 glioma tumors. Neoplasia. 2005;7(2):109-17. doi: 10.1593/neo.04436. PubMed PMID: 15802016; PubMed Central PMCID: PMC1501126.

65. Zurkiya O, Chan AW, Hu X. MagA is sufficient for producing magnetic nanoparticles in mammalian cells, making it an MRI reporter. Magnetic Resonance in Medicine. 2008;59(6):1225-31. doi: 10.1002/mrm.21606. PubMed PMID: 18506784.

66. Bartelle BB, Szulc KU, Suero-Abreu GA, Rodriguez JJ, Turnbull DH. Divalent metal transporter, DMT1: A novel MRI reporter protein. Magnetic Resonance in Medicine. 2013;70(3):842-50. doi: 10.1002/mrm.24509.

67. Patrick PS, Hammersley J, Loizou L, Kettunen MI, Rodrigues TB, Hu D-E, Tee S-S, Hesketh R, Lyons SK, Soloviev D, Lewis DY, Aime S, Fulton SM, Brindle KM. Dual-modality gene reporter for in vivo imaging. Proceedings of the National Academy of Sciences, USA. 2014;111(1):415-20. doi: 10.1073/pnas.1319000111.

68. Los GV, Encell LP, McDougall MG, Hartzell DD, Karassina N, Zimprich C, Wood MG, Learish R, Ohana RF, Urh M, Simpson D, Mendez J, Zimmerman K, Otto P, Vidugiris G, Zhu J, Darzins A, Klaubert

DH, Bulleit RF, Wood KV. HaloTag: A Novel Protein Labeling Technology for Cell Imaging and Protein Analysis. ACS Chemical Biology. 2008;3(6):373-82. doi: 10.1021/cb800025k.

69. Kosaka N, Ogawa M, Choyke PL, Karassina N, Corona C, McDougall M, Lynch DT, Hoyt CC, Levenson RM, Los GV, Kobayashi H. In Vivo Stable Tumor-Specific Painting in Various Colors Using Dehalogenase-Based Protein-Tag Fluorescent Ligands. Bioconjugate Chemistry. 2009;20(7):1367-74. doi: 10.1021/bc9001344.

70. Ohana RF, Hurst R, Vidugiriene J, Slater MR, Wood KV, Urh M. HaloTag-based purification of functional human kinases from mammalian cells. Protein Expression and Purification. 2011;76(2):154-64. doi: http://dx.doi.org/10.1016/j.pep.2010.11.014.

71. Zhang Y, So MK, Loening AM, Yao H, Gambhir SS, Rao J. HaloTag protein-mediated site-specific conjugation of bioluminescent proteins to quantum dots. Angewandte Chemie (English Edition). 2006;45(30):4936-40. Epub 2006/06/30. doi: 10.1002/anie.200601197. PubMed PMID: 16807952.

72. Hong H, Benink HA, Zhang Y, Yang Y, Uyeda HT, Engle JW, Severin GW, McDougall MG, Barnhart TE, Klaubert DH, Nickles RJ, Fan F, Cai W. HaloTag: a novel reporter gene for positron emission tomography. American journal of translational research. 2011;3(4):392-403. Epub 2011/09/10. PubMed PMID: 21904659; PubMed Central PMCID: PMCPmc3158741.

73. Cutler JI, Auyeung E, Mirkin CA. Spherical Nucleic Acids. Journal of the American Chemical Society. 2012;134(3):1376-91. doi: 10.1021/ja209351u.

74. Giljohann DA, Seferos DS, Daniel WL, Massich MD, Patel PC, Mirkin CA. Gold nanoparticles for biology and medicine. Angewandte Chemie (English Edition). 2010;49(19):3280-94. doi: 10.1002/anie.200904359. PubMed PMID: 20401880; PubMed Central PMCID: PMC3930332.

75. Jensen SA, Day ES, Ko CH, Hurley LA, Luciano JP, Kouri FM, Merkel TJ, Luthi AJ, Patel PC, Cutler JI, Daniel WL, Scott AW, Rotz MW, Meade TJ, Giljohann DA, Mirkin CA, Stegh AH. Spherical nucleic acid nanoparticle conjugates as an RNAi-based therapy for glioblastoma. Science translational medicine. 2013;5(209):209ra152. doi: 10.1126/scitranslmed.3006839. PubMed PMID: 24174328; PubMed Central PMCID: PMC4017940.

76. Song Y, Xu X, MacRenaris KW, Zhang XQ, Mirkin CA, Meade TJ. Multimodal gadolinium-enriched DNA-gold nanoparticle conjugates for cellular imaging. Angewandte Chemie (English Edition). 2009;48(48):9143-7. doi: 10.1002/anie.200904666. PubMed PMID: 19882611; PubMed Central PMCID: PMC2917899.

77. Choi CHJ, Hao L, Narayan SP, Auyeung E, Mirkin CA. Mechanism for the endocytosis of spherical nucleic acid nanoparticle conjugates. Proceedings of the National Academy of Sciences, USA. 2013;110(19):7625-30. doi: 10.1073/pnas.1305804110.

78. Zhang K, Hao L, Hurst SJ, Mirkin CA. Antibody-Linked Spherical Nucleic Acids for Cellular Targeting. Journal of the American Chemical Society. 2012;134(40):16488-91. doi: 10.1021/ja306854d.

79. Zheng D, Seferos DS, Giljohann DA, Patel PC, Mirkin CA. Aptamer Nano-flares for Molecular Detection in Living Cells. Nano Letters. 2009;9(9):3258-61. doi: 10.1021/nl901517b.

80. Hurst SJ, Lytton-Jean AKR, Mirkin CA. Maximizing DNA Loading on a Range of Gold Nanoparticle Sizes. Analytical Chemistry. 2006;78(24):8313-8. doi: 10.1021/ac0613582.

81. Neklesa TK, Tae HS, Schneekloth AR, Stulberg MJ, Corson TW, Sundberg TB, Raina K, Holley SA, Crews CM. Small-molecule hydrophobic tagging–induced degradation of HaloTag fusion proteins. Nat Chem Biol. 2011;7(8):538-43. doi: http://www.nature.com/nchembio/journal/v7/n8/abs/nchembio.597.html#supplementary-information.

82. Mastarone DJ, Harrison VSR, Eckermann AL, Parigi G, Luchinat C, Meade TJ. A Modular System for the Synthesis of Multiplexed Magnetic Resonance Probes. Journal of the American Chemical Society. 2011;133(14):5329-37. doi: 10.1021/ja1099616.

83. Padovan-Merhar O, Nair Gautham P, Biaesch Andrew G, Mayer A, Scarfone S, Foley Shawn W, Wu Angela R, Churchman LS, Singh A, Raj A. Single Mammalian Cells Compensate for Differences in Cellular Volume and DNA Copy Number through Independent Global Transcriptional Mechanisms. Molecular Cell. 2015;58(2):339-52. doi: 10.1016/j.molcel.2015.03.005.

84. Dai Q, Walkey C, Chan WCW. Polyethylene Glycol Backfilling Mitigates the Negative Impact of the Protein Corona on Nanoparticle Cell Targeting. Angewandte Chemie International Edition. 2014;53(20):5093-6. doi: 10.1002/anie.201309464.

85. Lundqvist M, Stigler J, Elia G, Lynch I, Cedervall T, Dawson KA. Nanoparticle size and surface properties determine the protein corona with possible implications for biological impacts. Proceedings of the National Academy of Sciences. 2008;105(38):14265-70. doi: 10.1073/pnas.0805135105.

86. Hong V, Presolski SI, Ma C, Finn MG. Analysis and Optimization of Copper-Catalyzed Azide–Alkyne Cycloaddition for Bioconjugation. Angewandte Chemie International Edition. 2009;48(52):9879-83. doi: 10.1002/anie.200905087.

87. Brookmeyer R, Johnson E, Ziegler-Graham K, Arrighi HM. Forecasting the global burden of Alzheimer's disease. Alzheimer's & Dementia. 2007;3(3):186-91. doi: http://dx.doi.org/10.1016/j.jalz.2007.04.381.

88. Wimo A, Jönsson L, Bond J, Prince M, Winblad B. The worldwide economic impact of dementia 2010. Alzheimer's & Dementia. 2013;9(1):1-11.e3. doi: http://dx.doi.org/10.1016/j.jalz.2012.11.006.

89. Mollee P, Renaut P, Gottlieb D, Goodman H. How to diagnose amyloidosis. Internal Medicine Journal. 2014;44(1):7-17. doi: 10.1111/imj.12288.

90. Nagarajan R. Molecular Packing Parameter and Surfactant Self-Assembly: The Neglected Role of the Surfactant Tail. Langmuir. 2002;18(1):31-8. doi: 10.1021/la010831y.

91. Manus LM, Mastarone DJ, Waters EA, Zhang X-Q, Schultz-Sikma EA, MacRenaris KW, Ho D, Meade TJ. Gd(III)-nanodiamond conjugates for MRI contrast enhancement. Nano letters. 2010;10(2):484-9. doi: 10.1021/nl903264h. PubMed PMID: PMC2829273.

92. Chinisaz M, Ebrahim-Habibi A, Yaghmaei P, Parivar K, Dehpour A-R. Generating local amyloidosis in mice by the subcutaneous injection of human insulin amyloid fibrils. Experimental and Therapeutic Medicine. 2014;8(2):405-8. doi: 10.3892/etm.2014.1772. PubMed PMID: PMC4079414.

93. Lockhart A, Ye L, Judd DB, Merritt AT, Lowe PN, Morgenstern JL, Hong G, Gee AD, Brown J. Evidence for the Presence of Three Distinct Binding Sites for the Thioflavin T Class of Alzheimer's Disease PET Imaging Agents on β-Amyloid Peptide Fibrils. Journal of Biological Chemistry. 2005;280(9):7677-84. doi: 10.1074/jbc.M412056200.

94. Hong MC, Kim YK, Choi JY, Yang SQ, Rhee H, Ryu YH, Choi TH, Cheon GJ, An GI, Kim HY, Kim Y, Kim DJ, Lee J-S, Chang Y-T, Lee KC. Synthesis and evaluation of stilbene derivatives as a potential

imaging agent of amyloid plaques. Bioorganic & Medicinal Chemistry. 2010;18(22):7724-30. doi: http://dx.doi.org/10.1016/j.bmc.2010.06.044.

95. Shen CL, Murphy RM. Solvent effects on self-assembly of beta-amyloid peptide. Biophysical Journal. 1995;69(2):640-51. PubMed PMID: PMC1236289.

96. Bissig C, Rochin L, van Niel G. PMEL Amyloid Fibril Formation: The Bright Steps of Pigmentation. International Journal of Molecular Sciences. 2016;17(9):1438. doi: 10.3390/ijms17091438. PubMed PMID: PMC5037717.

97. Ono M, Saji H. SPECT Imaging Agents for Detecting Cerebral β-Amyloid Plaques. International Journal of Molecular Imaging. 2011;2011. doi: 10.1155/2011/543267.

98. Harrison VSR, Carney CE, MacRenaris KW, Waters EA, Meade TJ. Multimeric Near IR–MR Contrast Agent for Multimodal In Vivo Imaging. Journal of the American Chemical Society. 2015;137(28):9108-16. doi: 10.1021/jacs.5b04509.

99. Barnholtz-Sloan JS, Sloan AE, Davis FG, Vigneau FD, Lai P, Sawaya RE. Incidence proportions of brain metastases in patients diagnosed (1973 to 2001) in the Metropolitan Detroit Cancer Surveillance System. Journal of clinical oncology : official journal of the American Society of Clinical Oncology. 2004;22(14):2865-72. Epub 2004/07/16. doi: 10.1200/jco.2004.12.149. PubMed PMID: 15254054.

100. Tsukada Y, Fouad A, Pickren JW, Lane WW. Central nervous system metastasis from breast carcinoma. Autopsy study. Cancer. 1983;52(12):2349-54. Epub 1983/12/15. PubMed PMID: 6640506.

101. Weil RJ, Palmieri DC, Bronder JL, Stark AM, Steeg PS. Breast cancer metastasis to the central nervous system. The American journal of pathology. 2005;167(4):913-20. Epub 2005/09/30. doi: 10.1016/s0002-9440(10)61180-7. PubMed PMID: 16192626; PubMed Central PMCID: PMCPmc1603675.

102. Khanna C, Hunter K. Modeling metastasis in vivo. Carcinogenesis. 2005;26(3):513-23. Epub 2004/09/11. doi: 10.1093/carcin/bgh261. PubMed PMID: 15358632.

103. Carney CE, MacRenaris KW, Meade TJ. Water-soluble lipophilic MR contrast agents for cell membrane labeling. JBIC Journal of Biological Inorganic Chemistry. 2015;20(6):971-7. doi: 10.1007/s00775-015-1280-4.

104. Nandwana V, De M, Chu S, Jaiswal M, Rotz M, Meade TJ, Dravid VP. Theranostic Magnetic Nanostructures (MNS) for Cancer. In: Mirkin CA, Meade TJ, Petrosko SH, Stegh AH, editors. Nanotechnology-Based Precision Tools for the Detection and Treatment of Cancer. Cham: Springer International Publishing; 2015. p. 51-83.

105. Lin W, Hyeon T, Lanza GM, Zhang M, Meade TJ. Magnetic Nanoparticles for Early Detection of Cancer by Magnetic Resonance Imaging. MRS Bulletin. 2009;34(06):441-8. doi: doi:10.1557/mrs2009.120.

106. Bulte JWM. In Vivo MRI Cell Tracking: Clinical Studies. American Journal of Roentgenology. 2009;193(2):314-25. doi: 10.2214/AJR.09.3107.

107. Bulte JWM, Kraitchman DL. Iron oxide MR contrast agents for molecular and cellular imaging. NMR in Biomedicine. 2004;17(7):484-99. doi: 10.1002/nbm.924.

108. Liu W, Dahnke H, Jordan EK, Schaeffter T, Frank JA. In vivo MRI using positive-contrast techniques in detection of cells labeled with superparamagnetic iron oxide nanoparticles. NMR in Biomedicine. 2008;21(3):242-50. doi: 10.1002/nbm.1187.

109. Heyn C, Ronald JA, Mackenzie LT, MacDonald IC, Chambers AF, Rutt BK, Foster PJ. In vivo magnetic resonance imaging of single cells in mouse brain with optical validation. Magnetic Resonance in Medicine. 2006;55(1):23-9. doi: 10.1002/mrm.20747.

110. Shapiro EM, Sharer K, Skrtic S, Koretsky AP. In vivo detection of single cells by MRI. Magnetic Resonance in Medicine. 2006;55(2):242-9. doi: 10.1002/mrm.20718.

111. Farrell E, Wielopolski P, Pavljasevic P, van Tiel S, Jahr H, Verhaar J, Weinans H, Krestin G, O'Brien FJ, van Osch G, Bernsen M. Effects of iron oxide incorporation for long term cell tracking on MSC differentiation in vitro and in vivo. Biochemical and Biophysical Research Communications. 2008;369(4):1076-81. doi: http://dx.doi.org/10.1016/j.bbrc.2008.02.159.

112. Schäfer R, Kehlbach R, Müller M, Bantleon R, Kluba T, Ayturan M, Siegel G, Wolburg H, Northoff H, Dietz K, Claussen CD, Wiskirchen J. Labeling of human mesenchymal stromal cells with superparamagnetic iron oxide leads to a decrease in migration capacity and colony formation ability. Cytotherapy. 2009;11(1):68-78. doi: doi:10.1080/14653240802666043.

113. Hu F, MacRenaris KW, A. Waters E, Schultz-Sikma EA, Eckermann AL, Meade TJ. Highly dispersible, superparamagnetic magnetite nanoflowers for magnetic resonance imaging. Chemical Communications. 2010;46(1):73-5. doi: 10.1039/B916562B.

114. Cheon J, Lee J-H. Synergistically Integrated Nanoparticles as Multimodal Probes for Nanobiotechnology. Accounts of Chemical Research. 2008;41(12):1630-40. doi: 10.1021/ar800045c.

115. Lorger M, Felding-Habermann B. Capturing changes in the brain microenvironment during initial steps of breast cancer brain metastasis. The American journal of pathology. 2010;176(6):2958-71. Epub 2010/04/13. doi: 10.2353/ajpath.2010.090838. PubMed PMID: 20382702; PubMed Central PMCID: PMCPmc2877856.

116. Hamilton AM, Aidoudi-Ahmed S, Sharma S, Kotamraju VR, Foster PJ, Sugahara KN, Ruoslahti E, Rutt BK. Nanoparticles coated with the tumor-penetrating peptide iRGD reduce experimental breast cancer metastasis in the brain. Journal of molecular medicine (Berlin, Germany). 2015;93(9):991-1001. Epub 2015/04/15. doi: 10.1007/s00109-015-1279-x. PubMed PMID: 25869026.

117. Wang Q, West M. Model-controlled flooding with applications to image reconstruction and segmentation. Journal of electronic imaging. 2012;21(2). Epub 2012/10/11. doi: 10.1117/1.jei.21.2.023020. PubMed PMID: 23049229; PubMed Central PMCID: PMCPmc3462023.

118. Wileman T, Harding C, Stahl P. Receptor-mediated endocytosis. Biochemical Journal. 1985;232(1):1-14. PubMed PMID: PMC1152830.

119. Vistain LF, Rotz MW, Rathore R, Preslar AT, Meade TJ. Targeted delivery of gold nanoparticle contrast agents for reporting gene detection by magnetic resonance imaging. Chemical Communications. 2016;52(1):160-3. doi: 10.1039/C5CC06565H.

120. Holbrook RJ, Rammohan N, Rotz MW, MacRenaris KW, Preslar AT, Meade TJ. Gd(III)-Dithiolane Gold Nanoparticles for T1-Weighted Magnetic Resonance Imaging of the Pancreas. Nano Letters. 2016;16(5):3202-9. doi: 10.1021/acs.nanolett.6b00599.

121. Hinterwirth H, Kappel S, Waitz T, Prohaska T, Lindner W, Lämmerhofer M. Quantifying Thiol Ligand Density of Self-Assembled Monolayers on Gold Nanoparticles by Inductively Coupled Plasma–Mass Spectrometry. ACS Nano. 2013;7(2):1129-36. doi: 10.1021/nn306024a.

122. Forster MD, Ormerod MG, Agarwal R, Kaye SB, Jackman AL. Flow cytometric method for determining folate receptor expression on ovarian carcinoma cells. Cytometry Part A. 2007;71A(11):945-50. doi: 10.1002/cyto.a.20456.

123. Sabharanjak S, Mayor S. Folate receptor endocytosis and trafficking. Advanced Drug Delivery Reviews. 2004;56(8):1099-109. doi: http://dx.doi.org/10.1016/j.addr.2004.01.010.

124. Chang SS. Overview of Prostate-Specific Membrane Antigen. Reviews in Urology. 2004;6(Suppl 10):S13-S8. PubMed PMID: PMC1472940.

125. Chen Y, Dhara S, Banerjee SR, Byun Y, Pullambhatla M, Mease RC, Pomper MG. A Low Molecular Weight PSMA-Based Fluorescent Imaging Agent for Cancer. Biochemical and biophysical research communications. 2009;390(3):624-9. doi: 10.1016/j.bbrc.2009.10.017. PubMed PMID: PMC2787846.

126. Kamen BA, Capdevila A. Receptor-mediated folate accumulation is regulated by the cellular folate content. Proceedings of the National Academy of Sciences of the United States of America. 1986;83(16):5983-7. PubMed PMID: PMC386421.

127. Maraveyas A, Johnson Miriam J, Xiao Yu P, Noble S. Malignant melanoma as a target malignancy for the study of the anti-metastatic properties of the heparins. Cancer metastasis reviews. 2010;29(4):777-84. PubMed PMID: 2010915816.

128. Coleman Robert E, Lipton A, Roodman GD, Guise Theresa A, Boyce Brendon F, Brufsky Adam M, Clezardin P, Croucher Peter I, Gralow Julie R, Hadji P, Holen I, Mundy Gregory R, Smith Matthew R, Suva Larry J. Metastasis and bone loss: advancing treatment and prevention. Cancer treatment reviews. 2010;36(8):615-20. PubMed PMID: 2010966418.

129. Deryugina E, Quigley J. Matrix metalloproteinases and tumor metastasis. Cancer Metastasis Rev. 2006;25(1):9-34. doi: 10.1007/s10555-006-7886-9.

130. Robichaud N, del Rincon SV, Huor B, Alain T, Petruccelli LA, Hearnden J, Goncalves C, Grotegut S, Spruck CH, Furic L, Larsson O, Muller WJ, Miller WH, Sonenberg N. Phosphorylation of eIF4E promotes EMT and metastasis via translational control of SNAIL and MMP-3. Oncogene. 2015;34(16):2032-42. doi: 10.1038/onc.2014.146.

131. Kudo-Saito C, Shirako H, Takeuchi T, Kawakami Y. Cancer Metastasis Is Accelerated through Immunosuppression during Snail-Induced EMT of Cancer Cells. Cancer Cell. 2009;15(3):195-206. doi: http://dx.doi.org/10.1016/j.ccr.2009.01.023.

132. Yang MH, Chang SY, Chiou SH, Liu CJ, Chi CW, Chen PM, Teng SC, Wu KJ. Overexpression of NBS1 induces epithelial-mesenchymal transition and co-expression of NBS1 and Snail predicts metastasis of head and neck cancer. Oncogene. 2006;26(10):1459-67. doi: http://www.nature.com/onc/journal/v26/n10/suppinfo/1209929s1.html.

133. Barrallo-Gimeno A, Nieto MA. The snail genes as inducers of cell movement and survival: Implications in development and cancer. Development (Cambridge, United Kingdom). 2005;132(14):3151-61. doi: 10.1242/dev.01907. PubMed PMID: 2005:843590.

134. Baum B, Settleman J, Quinlan MP. Transitions between epithelial and mesenchymal states in development and disease. Seminars in Cell & Developmental Biology. 2008;19(3):294-308. doi: 10.1016/j.semcdb.2008.02.001. PubMed PMID: 2008:442956.

135. Voulgari A, Pintzas A. Epithelial-mesenchymal transition in cancer metastasis: Mechanisms, markers and strategies to overcome drug resistance in the clinic. Biochimica et Biophysica Acta, Reviews on Cancer. 2009;1796(2):75-90. doi: 10.1016/j.bbcan.2009.03.002. PubMed PMID: 2009:1189285.

136. Mego M, Mani SA, Cristofanilli M. Molecular mechanisms of metastasis in breast cancer-clinical applications. Nature Reviews Clinical Oncology. 2010;7(12):693-701. doi: 10.1038/nrclinonc.2010.171. PubMed PMID: 2010:1483437.

137. Brabletz T. To differentiate or not - routes towards metastasis. Nature Reviews Cancer. 2012;12(6):425-36. doi: 10.1038/nrc3265. PubMed PMID: 2012:683997.

138. Nieto MA. The Snail superfamily of zinc-finger transcription factors. Nature Reviews Molecular Cell Biology. 2002;3(3):155-66. doi: 10.1038/nrm757. PubMed PMID: 2002:210220.

139. Cano A, Perez-Moreno MA, Rodrigo I, Locascio A, Blanco MJ, Del Barrio MG, Portillo F, Nieto MA. The transcription factor Snail controls epithelial-mesenchymal transitions by repressing E-cadherin expression. Nature Cell Biology. 2000;2(2):76-83. doi: 10.1038/35000025. PubMed PMID: 2000:108662.

140. Roy F, Berx G. The cell-cell adhesion molecule E-cadherin. Cellular and Molecular Life Sciences. 2008;65(23):3756-88. doi: 10.1007/s00018-008-8281-1. PubMed PMID: 2008:1453162.

141. Perl A-K, Wilgenbus P, Dahl U, Semb H, Christofori G. A causal role for E-cadherin in the transition from adenoma to carcinoma. Nature (London). 1998;392(6672):190-3. PubMed PMID: 1998:193620.

142. Vleminckx K, Vakaet L, Jr., Mareel M, Fiers W, Van Roy F. Genetic manipulation of E-cadherin expression by epithelial tumor cells reveals an invasion suppressor role. Cell (Cambridge, MA, United States). 1991;66(1):107-19. doi: 10.1016/0092-8674(91)90143-m. PubMed PMID: 1991:556123.

143. Frixen UH, Behrens J, Sachs M, Eberle G, Voss B, Warda A, Loechner D, Birchmeier W. E-cadherin-mediated cell-cell adhesion prevents invasiveness of human carcinoma cells. Journal of Cell Biology. 1991;113(1):173-85. doi: 10.1083/jcb.113.1.173. PubMed PMID: 1991:183081.

144. Konstantinopoulos PA, Papavassiliou AG. Seeing the future of cancer-associated transcription factor drug targets. JAMA, the Journal of the American Medical Association. 2011;305(22):2349-50. PubMed PMID: 2011:737437.

145. Rodriguez-Martinez JA, Peterson-Kaufman KJ, Ansari AZ. Small-molecule regulators that mimic transcription factors. Biochimica et Biophysica Acta, Gene Regulatory Mechanisms. 2010;1799(10-12):768-74. doi: 10.1016/j.bbagrm.2010.08.010. PubMed PMID: 2010:1522681.

146. Pazos E, Portela C, Penas C, Vazquez ME, Mascarenas JL. Peptide-DNA conjugates as tailored bivalent binders of the oncoprotein c-Jun. Organic & Biomolecular Chemistry. 2015;13(19):5385-90. doi: 10.1039/C5OB00318K.

147. Portela C, Albericio F, Eritja R, Castedo L, Mascareñas JL. ds-Oligonucleotide–Peptide Conjugates Featuring Peptides from the Leucine-Zipper Region of Fos as Switchable Receptors for the Oncoprotein Jun. ChemBioChem. 2007;8(10):1110-4. doi: 10.1002/cbic.200700115.

148. Harney AS, Lee J, Manus LM, Wang P, Ballweg DM, La Bonne C, Meade TJ. Targeted inhibition of Snail family zinc finger transcription factors by oligonucleotide-Co(III) Schiff base conjugate. Proceedings of the National Academy of Sciences of the United States of America. 2009;106(33):13667-72, S/1-S/3. doi: 10.1073/pnas.0906423106. PubMed PMID: 2009:1117207; PubMed Central PMCID: PMCPMC2728951.

149. Takeuchi T, Bottcher A, Quezada CM, Meade TJ, Gray HB. Inhibition of thermolysin and human α-thrombin by cobalt(III) Schiff base complexes. Bioorganic & Medicinal Chemistry. 1999;7(5):815-9. doi: 10.1016/s0968-0896(98)00272-7. PubMed PMID: 1999:383505.

150. Takeuchi T, Boettcher A, Quezada CM, Simon MI, Meade TJ, Gray HB. Selective Inhibition of Human α-Thrombin by Cobalt(III) Schiff Base Complexes. J Am Chem Soc. 1998;120(33):8555-6. doi: 10.1021/ja981191x. PubMed PMID: 1998:499468.

151. Louie AY, Meade TJ. A cobalt complex that selectively disrupts the structure and function of zinc fingers. Proceedings of the National Academy of Sciences of the United States of America. 1998;95(12):6663-8. doi: 10.1073/pnas.95.12.6663. PubMed PMID: 1998:378459; PubMed Central PMCID: PMCPMC22591.

152. Manus LM, Holbrook RJ, Atesin TA, Heffern MC, Harney AS, Eckermann AL, Meade TJ. Axial Ligand Exchange of N-heterocyclic Cobalt(III) Schiff Base Complexes: Molecular Structure and NMR Solution Dynamics. Inorg Chem. 2013;52(2):1069-76. doi: 10.1021/ic302379j. PubMed PMID: 2013:20389.

153. Heffern MC, Kurutz JW, Meade TJ. Spectroscopic Elucidation of the Inhibitory Mechanism of Cys2His2 Zinc Finger Transcription Factors by Cobalt(III) Schiff Base Complexes. Chemistry – A European Journal. 2013;19(50):17043-53. doi: 10.1002/chem.201301659.

154. Heffern MC, Yamamoto N, Holbrook RJ, Eckermann AL, Meade TJ. Cobalt derivatives as promising therapeutic agents. Current Opinion in Chemical Biology. 2013;17(2):189-96. doi: http://dx.doi.org/10.1016/j.cbpa.2012.11.019.

155. Harney AS, Meade TJ, Labonne C. Targeted Inactivation of Snail Family EMT Regulatory Factors by a Co(III)-Ebox Conjugate. PLoS One. 2012;7(2):e32318. PubMed PMID: 2012288446; PubMed Central PMCID: PMCPMC3290632.

156. Hurtado RR, Harney AS, Heffern MC, Holbrook RJ, Holmgren RA, Meade TJ. Specific inhibition of the transcription factor Ci by a cobalt(III) schiff base-DNA conjugate. Molecular Pharmaceutics. 2012;9(2):325-33. doi: 10.1021/mp2005577. PubMed PMID: 2012:12388; PubMed Central PMCID: PMCPMC3313626.

157. Kim J, Jeong H, Lee Y, Kim C, Kim H, Kim A. HRG-β1-driven ErbB3 signaling induces epithelial-mesenchymal transition in breast cancer cells. BMC cancer. 2013;13:383. PubMed PMID: 2013889765.

158. Cheng LS, Zha Z, Lang B, Liu J, Yao XB. Heregulin-β1 promotes metastasis of breast cancer cell line SKBR3 through upregulation of Snail and induction of epithelial-mesenchymal transition. Cancer Letters (Shannon, Ireland). 2009;280(1):50-60. doi: 10.1016/j.canlet.2009.02.007. PubMed PMID: 2009:599764.

159. Breuleux M. Role of heregulin in human cancer. Cellular and Molecular Life Sciences. 2007;64(18):2358-77. doi: 10.1007/s00018-007-7120-0. PubMed PMID: 2007:1199671.

160. Slamon DJ, Godolphin W, Jones LA, Holt JA, Wong SG, Keith DE, Levin WJ, Stuart SG, Udove J, Ullrich A, et al. Studies of the HER-2/neu proto-oncogene in human breast and ovarian cancer. Science. 1989;244(4905):707-12. PubMed PMID: 1989242144.

161. Slamon DJ, Clark GM, Wong SG, Levin WJ, Ullrich A, McGuire WL. Human breast cancer: correlation of relapse and survival with amplification of the HER-2/neu oncogene. Science (Washington, DC, United States). 1987;235(4785):177-82. doi: 10.1126/science.3798106. PubMed PMID: 1987:100255.

162. Ross JS, Fletcher JA. The HER-2/neu oncogene in breast cancer: prognostic factor, predictive factor, and target for therapy. Stem cells (Dayton, Ohio). 1998;16(6):413-28. PubMed PMID: 1999048707.

163. Adam L, Vadlamudi R, Kondapaka SB, Chernoff J, Mendelsohn J, Kumar R. Heregulin regulates cytoskeletal reorganization and cell migration through the p21-activated kinase-1 via phosphatidylinositol-3 kinase. Journal of Biological Chemistry. 1998;273(43):28238-46. doi: 10.1074/jbc.273.43.28238. PubMed PMID: 1998:704605.

164. Hajra KM, Chen DYS, Fearon ER. The SLUG zinc-finger protein represses E-cadherin in breast cancer. Cancer Research. 2002;62(6):1613-8. PubMed PMID: 2002:240121.

165. Domínguez D, Montserrat-Sentís B, Virgós-Soler A, Guaita S, Grueso J, Porta M, Puig I, Baulida J, Francí C, García de Herreros A. Phosphorylation Regulates the Subcellular Location and Activity of the Snail Transcriptional Repressor. Molecular and Cellular Biology. 2003;23(14):5078-89. doi: 10.1128/mcb.23.14.5078-5089.2003.

166. de Herreros Antonio G, Peiro S, Nassour M, Savagner P. Snail family regulation and epithelial mesenchymal transitions in breast cancer progression. Journal of mammary gland biology and neoplasia. 2010;15(2):135-47. PubMed PMID: 2010505880.

167. Franci C, Takkunen M, Dave N, Alameda F, Gomez S, Rodriguez R, Escriva M, Montserrat-Sentis B, Baro T, Garrido M, Bonilla F, Virtanen I, Garcia de Herreros A. Expression of Snail protein in tumor-stroma interface. Oncogene. 2006;25(37):5134-44. doi: 10.1038/sj.onc.1209519. PubMed PMID: 2006:847565.

168. De Craene B, Gilbert B, Stove C, Bruyneel E, van Roy F, Berx G. The Transcription Factor Snail Induces Tumor Cell Invasion through Modulation of the Epithelial Cell Differentiation Program. Cancer Research. 2005;65(14):6237-44. doi: 10.1158/0008-5472.can-04-3545.

169. Moody SE, Perez D, Pan T-c, Sarkisian CJ, Portocarrero CP, Sterner CJ, Notorfrancesco KL, Cardiff RD, Chodosh LA. The transcriptional repressor Snail promotes mammary tumor recurrence. Cancer Cell. 2005;8(3):197-209. doi: http://dx.doi.org/10.1016/j.ccr.2005.07.009.

170. Yao J, Xiong S, Klos K, Nguyen N, Grijalva R, Li P, Yu D. Multiple signaling pathways involved in activation of matrix metalloproteinase-9 (MMP-9) by heregulin-β1 in human breast cancer cells. Oncogene. 2001;20(56):8066-74. doi: 10.1038/sj.onc.1204944. PubMed PMID: 2001:936769.

171. Jordà M, Olmeda D, Vinyals A, Valero E, Cubillo E, Llorens A, Cano A, Fabra À. Upregulation of MMP-9 in MDCK epithelial cell line in response to expression of the Snail transcription factor. Journal of Cell Science. 2005;118(15):3371-85. doi: 10.1242/jcs.02465.

172. Kim BJ, Hambley TW, Bryce NS. Visualising the hypoxia selectivity of cobalt(iii) prodrugs. Chemical Science. 2011;2(11):2135-42. doi: 10.1039/c1sc00337b. PubMed PMID: 2011:1291054.

173. Kushima Y, Iida K, Nagaoka Y, Kawaratani Y, Shirahama T, Sakaguchi M, Baba K, Hara Y, Uesato S. Inhibitory effect of (-)-epigallocatechin and (-)-epigallocatechin gallate against heregulin β1-induced migration/invasion of the MCF-7 breast carcinoma cell line. Biological & Pharmaceutical Bulletin. 2009;32(5):899-904. doi: 10.1248/bpb.32.899. PubMed PMID: 2009:645631.

174. Yin KB. The Mesenchymal-Like Phenotype of MDA-MB-231 Cell Line. In: Gunduz MaG, Esra, editor. Breast Cancer - Focusing Tumor Microenvironment, Stem cells and Metastasis: InTech Open Access Publisher Book Project; 2011. p. 385-403.

175. Oft M, Peli J, Rudaz C, Schwarz H, Beug H, Reichmann E. TGF-β1 and Ha-Ras collaborate in modulating the phenotypic plasticity and invasiveness of epithelial tumor cells. Genes & Development. 1996;10(19):2462-77. doi: 10.1101/gad.10.19.2462. PubMed PMID: 1996:626488.

176. Waters JC. Accuracy and precision in quantitative fluorescence microscopy. Journal of Cell Biology. 2009;185(7):1135-48. doi: 10.1083/jcb.200903097. PubMed PMID: 2009:822951.

Resume

Luke F. Vistain

1106 Davis St. Apt 3, Evanston, IL 60201 | Phone: (224)436-4764 | Email:lvistain@gmail.com

---

EDUCATION

Northwestern University, Evanston IL Anticipated graduation date: Winter 2017

Ph.D. in Biological Sciences (Overall GPA: 3.9)

Advisor: Thomas J. Meade, Ph.D.

New York University, New York, New York Graduated May 2007

B.A. in Biochemistry (Overall GPA: 3.5)

SCHOLARSHIP

NIH Ruth L. Kirschstein National Research Service Award (total award: $170,000) 2012-2016

WORK EXPERIENCE

Graduate Research Assistant Northwestern University, Evanston, 2010-present

Interdisciplinary Biological Sciences, PI: Thomas J. Meade, Ph.D.

Thesis title: A HaloTag-targeted AuDNA-Gd(III)-HT Nanoparticle for Molecular Imaging and Detection of Gene Expression

Objective: To develop a platform for the detection of cell surface receptors via MRI

Key accomplishments and responsibilities:

- Created a library of MRI contrast agents targeted to the HaloTag protein
- Synthesized novel nanoparticle probes to enhance the MR signal generated by HaloTag binding
- Developed assays to quantitatively measure expression levels of cell surface receptors
- Created techniques to measure nanoparticle binding in several cell lines
- Collaborated with chemists, imaging specialists, and engineers to develop appropriate model systems to measure reporter gene signal
- Supervised and trained undergraduate and graduate students through multi year-long projects

Research Technician II Rosalind Franklin University, North Chicago, Illinois 2008-2010

Biochemistry and Molecular Biology, PI: David Mueller, Ph.D.
Study of the structure of yeast F1Fo ATP Synthase

Key responsibilities:

- Design and execution of protein crystallization screens
- Protein purification (water-soluble and transmembrane)
- Operated a large scale (80 liter) yeast fermenter

Hospira North Chicago, Illinois 2007-2008

Sterility Technician

Key accomplishments and responsibilities:

- Pharmaceutical sterility testing
- Good manufacturing practice (GMP) documentation

PUBLICATIONS

Vistain, L. F., Rotz, M. W., Rathore, R., Preslar A.T., Meade, T.J., Targeted Delivery of Gold Nanoparticle Contrast Agents for Reporting Gene Detection by Magnetic Resonance Imaging. *Chemical Communications,* 2016, 52:160-163, DOI: 10.1039/c5cc06565h

PUBLICATIONS

Vistain, L. F.*, Yamamoto N.*, Rathore R., Cha, P., Meade, T.J., Targeted Inhibition of Snail Activity in Breast Cancer Cells Using a Co(III)-Ebox Conjugate. *ChemBioChem*, Sep 25 2015, 16(14):2065-72

Pagadala, V., **Vistain, L**., Symersky, J., and Mueller, D.M., Characterization of the mitochondrial ATP synthase from yeast *Saccharomyces cerevisae*. *Journal of Bioenergetics and Biomembranes*, 2011, 43:333-347

PATENTS

Meade, T.J., Strauch, R.C., **Vistain, L.F.**, MRI Contrast Agents, Patent pending 13/853324, Apr 27 2012.

SKILLS

Molecular Biology: PCR, real-time PCR, staggered extension PCR, cloning, SDS-PAGE, and western blotting

Cell Biology: cell culture, multi-color flow cytometry, cell transfection, 2nd generation lentiviral packaging and transduction

Chemistry: Basic synthetic chemistry, thin layer chromatography, nuclear magnetic resonance, mass spectrometry (ESI, MALDI, and ICP)

Imaging: Phase contrast microscopy, fluorescence microscopy, confocal microscopy, and magnetic resonance imaging
Purification: High-pressure liquid chromatography, silica chromatography, size-exclusion chromatography, affinity chromatography (nickel column), centrifugation, ultracentrifugation, and detergent extraction
Other: GMP, Grant writing, Microsoft Office, Flowjo, and MATLAB

TEACHING EXPERIENCE

Teaching Assistant
Winter 2011 and winter 2012

Biochemistry Lab, Northwestern University, Evanston, IL

- Lectured for two lab sections to prepare students for experiments
- Lectured for three review sections prior to tests
- Produced and graded weekly quizzes

Undergraduate Mentorship
2012-2015

Meade lab, Northwestern University, Evanston, IL

- Provided hands-on training for three undergraduates in synthetic chemistry, cell culture, biochemistry, and cell biology

CONFERENCES

Vistain, L., Rotz, M., Meade, T.J., A Nanoparticle Platform for Protein-Targeted Delivery of High Gd(III) Concentrations. Imaging in 2020, September 21-25, 2014.

Pagadala, V., **Vistain, L.**, Asernieva, D., Symersky, J., and Mueller, D.M., Locking the Yeast ATP Synthase into a Single Rotomer Confromation to Aid in Crystallization. Gordon Research Conference on Molecular and Cellular Bioenergetics, June 7-12, 2009.

Arsenieva, D., Wang, Y., Symersky, J., **Vistain, L.**, and Mueller, D.M., Crystal Structures of Yeast Mitochondrial ATPase with Uncoupling Mutations. Biophysical Society, Fe. 20-24, 2010, San Francisco, CA.